ABSTRACT

Title of Dissertation:	High Temperature Radiation Absorption of Fuel Molecules And An Evaluation of Its Influence on Pool Fire Modeling

Kaoru Wakatsuki
Doctor of Philosophy, 2005

Dissertation Directed By:	Associate Professor, Jungho Kim
	Associate Professor, Greg Jackson
	Department of Mechanical Engineering

Infrared absorption coefficients of various gas and liquid fuels (propane, n-heptane, methanol, toluene, propylene and methyl methacrylate) were measured using high temperature Fourier transform infrared spectroscopy (FTIR) for a range of temperatures up to 1000 K in order to facilitate calculation of radiative absorption of fuel molecules in large-scale, non-premixed flames. Spectrally resolved fits as a function of temperature (up to 600 K) were calculated using a semi-empirical expression derived from quantum theory. These fits provided a basis for calculating infrared spectra for the fuels from 300 K to 1400 K. Extrapolating the fit to high temperature gave integrated total absorption coefficients with errors ≤ 20 % temperature up to 1000 K for measured hydrocarbon fuel specie. Highly resolved infrared absorption coefficient database of fuels and combustion products (H_2O, CO_2, and CO from HITEMP database, and soot from modeling) were created. Comparison of Planck mean absorption coefficients as a function of temperature indicated unique behavior with respect to molecular structure of

fuels. Directional radiation intensity at the fuel surface of 0.3 m methanol, heptane and toluene pool fires were solved using a one dimensional radiative transport equation for line of sight at flame centerline using the new radiation absorption coefficient database. The solution of transport equation predicted radiation intensity at fuel surface within 2 % for non-sooty methanol pool, but under predicted < -100% for sooty pool fires of heptane and toluene. Flame structure impacted importance of absorption and emission. Soot within the flame, which has continuous band absorption at entire infrared region, absorbed much more radiation than other species, which has particular discrete band absorption, and resulted in low radiation intensity at the fuel surface.

HIGH TEMPERATURE RADIATION ABSORPTION OF FUEL MOLECULES AND AN ENVALUATIOIN OF ITS INFLUENECE ON POOL FIRE MODELING

By

Kaoru Wakatsuki

Dissertation submitted to the Faculty of the Graduate School of the
University of Maryland, College Park, in partial fulfillment
of the requirements for the degree of
Doctor of Philosophy
2005

Advisory Committee:
Professor Jungho Kim, Chair
Professor Greg Jackson, Co-Chair
Professor Kenneth Yu, The Dean's representative
Professor James G. Quintiere
Professor Anthony Hamins
Professor Marc R. Nyden

Acknowledgements

I would like to express my deepest gratitude to my advisors, Drs. Jungho Kim and Greg Jackson, who gave me to the opportunity to work for their project from the Building and Fire research laboratory (BFRL) in National Institute of Standards and Technology (NIST) and led me to complete my PhD program. I greatly appreciate Drs. Anthony Hamins and Marc Nyden of BFRL in NIST, who gave me the interest of thermal energy feedback in a fire and supported me technically and financially. To Dr. James Quintiere, who first taught me how to play with fire and the fear of fire, and always cheered my wife and me to accomplish our goal in the U.S., I deeply appreciate his advice. I thank to Dr. Kenneth Yu for serving my dissertation as the Dean's representative, and to Dr. S. Paul Fuss of Alcohol, Tobacco, Firearms and Explosives (ATF) who gave me the opportunity to continue his project, and advised me to run and fix the high temperature FTIR in NIST.

To my friends of Department of Fire Protection Engineering (ENFP), Nathasak Boonmee, Yunyong Utiskul (Pock), Tingguang Ma, and Yi Wang, I thank to them all their help for my study and grateful discussion. To Drs. Francine Amon and Takashi Kashiwagi of BFRL at NIST, who supported me personally, and worked together for their projects, I greatly appreciate them. To Dr. Tomohiro Naruse of Building Research Insitute (BRI) in Japan, who worked with me during his two years stay in ENFP and gave me many advice for my study and a job search, I am so thankful to him, too.

To my wife, Kayo, I would like to give her my deepest appreciation. With her support and understanding for my dream, I have completed the academic program in the U.S. This degree is the achievement between Kayo and me. Finally, my special thanks go to Mr. and Mrs. William and Toshiko Lofquist, my relatives in law, for their support of our life in the U.S.

Table of Contents

List of Tables

List of Figures

CHAPTER 1   INTRODUCTION

1.1   Radiation feedback study in fire

1.1.1   Background

Energy to volatilize solid and liquid fuels in fires is transported by conduction, convection and radiation. With small fires less than 0.1 m in base diameter, conduction dominates the heat transfer to the fuel source, whereas convection tends to dominate for fires with diameters between 0.1 and 0.3 m. Above about 0.3 m, radiation heat transfer is typically the largest source of heat feedback to the fuel source [1]. Because of the dominance of radiation for large fires, an accurate assessment of radiation absorption within the fuel rich core of the fire becomes imperative for assessing heat feedback to the fuel source.

For large fires, radiation dominates external heat transfer to the surroundings as well as internal heat transfer to the fuel source. Hamins et al. [2] reported that radiation heat transfer provides 96%, 80% and 55% of total heat feedback to the fuel source for 0.3 m diameter (D) pool fires of toluene, n-heptane and methanol respectively. Because external heat transfer from these and large fires are typically dominated by radiation, assessment of fire damage depends on accurate models of radiative heat transfer emitted from fires, which in turn depends on the flame temperature. Flame temperature may be impacted by the absorption of radiation by both soot and the fuel rich core just above the fuel surface in a fire. Since the incident radiative heat flux controls fuel volatilization in

fires, accurate assessment of the effects of gaseous fuel molecules on radiative exchange is needed.

In most previous studies, combustion products such as carbon dioxide (CO_2), water vapor (H_2O), carbon monoxide (CO) and soot have been the focus of radiative transport [3-5]. Studies on the radiative absorption of these molecules have provided absorption coefficients over a broad range of temperatures, and one can obtain this data through HITEMP [6]. To include contributions of fuels and other decomposition products to radiative transport in fires, absorption coefficients for these molecules must be known over a broad range of temperatures characteristic of the fuel rich core, from 300 K to 1000 K [7, 8].

Many studies incorporating radiative transport in fires or combustion utilize a gray gas assumption to calculate radiation attenuation. The gray gas emissivity approximation is often based on empirical fits to external radiation intensity measurements, e.g., in fires of volatilized plastics [9]. The effective emissivity and corresponding absorptivity will vary significantly with flame temperature particularly for sooty flames depending on how close the peak of the broadband flame emissions falls relative to the strong absorption bands of the vaporized fuel molecules [10]. To date, only a few studies have attempted to provide data for assessing the temperature dependent absorption coefficients of fuel molecules to temperatures as high as 1000 K. Notable studies in this area include the work of Tien and coworkers on hydrocarbon fuels and methyl-methacrylate (MMA) [11-14], and Fuss et al. on paraffin hydrocarbons and acid gases [15-17]. Difficulties in measuring high-resolution infrared absorption coefficients at high temperature arise because of the temperature limitations of most

infrared window materials and issues associated with high temperature vacuum seals. This study has been undertaken to build a database for absorption coefficients for several hydrocarbon molecules for temperatures up to 1000 K. Infrared absorption coefficients of the hydrocarbons propane (C_3H_8), n-heptane (C_7H_{16}), and propylene (C_3H_6) were measured by Fourier transform infrared spectrometer (FTIR) in a unique experimental facility that facilitates measurements to 1000 K. These measurements are analyzed and compared to existing data for methane (CH_4) in the HITRAN [18] database.

1.1.2 Previous work

1.1.2.1 Radiation feedback in fires

A pool fire is a basic experiment to study characteristics of a fire. Application of the pool fires experiments includes fire growth in enclosures, such as compartment fires [19], tunnel fires [20], smoke management [20-23], fire suppression [20, 24-33], and oil tank fires [34-36]. Laboratory scale pool fire experiments are generally up to 1 m [2, 7, 10, 37, 38]. Several pool fire experiments in outdoors [35, 39] have been conducted so far, but the fires were affected by wind and weather, and cannot be correlated with predictions of a large pool fire extrapolated from small fire experiment. Although large pool fire experiments are necessary to determine the separation distance of oil tanks and tactics to extinguish oil tank fire practically, there is unfortunately little information on large pool fires. Computer modeling such as NIST's fire dynamics simulator (FDS) [40] is being developed to study large fires. Several fire modelers have tried to mimic small and large pool fires [41-43]. One of the current problems is that the computer model does not predict mass (fuel) evaporation rate well since radiation feedback from flame to fuel

surface is not calculated correctly. Radiation absorption by fuel molecules in the relatively cool fuel rich core above the fuel surface plays a significant role in controlling the amount of the energy reaching the fuel surface. For example, De Ris [44], Brosmer et al. [7], and Novozhilov et al [42]. used a gray gas absorption coefficient to calculate energy feedback on pool fire. Hostikka et al. [41] modeled methanol pool fires using NIST Fire Dynamics Simulator (FDS) [45] with RADCAL database [46]. Therefore, it is very important to resolve the role of fuel absorption on determining thermal energy feedback to fuel surface and mass burning rate for fire modeling. A summary of previous studies on energy feedback study on pool fires follows.

Buckius and Tien [3] first studied the radiation contribution of combustion products on monomer-polystyrene (PS, C_8H_8), monomer-poly-methylmethacrylate (PMMA, $C_5H_8O_2$), and monomer-polyacetal (PA, CH_2O) fires. They discovered soot is dominant in sooty fires such as PS , soot and product species are important in moderate sooty fires such as PMMA, and product species such as carbon dioxide, water, and carbon monoxide are dominant in non-sooty fires such as PA. They also found non-homogeneous and non-gray models predict the relationship between radiance and pathlength accurately.

De Ris [44] investigated energy feedback to a polymer (PMMA, PE, and PS) pool surface. He evaluated the validity of three radiation models, such as Hottel's emissivity charts, narrow-band statistical models and wide-band models [47], to predict emissivity of non-homogeneous and non-gray path within a fire. He stated that the narrow band approach is accurate, but needs expensive computation. The wide band model is moderately accurate significantly less computational demand for combustion simulations.

He assumed sooty and moderately sooty fires can use the gray gas radiation absorption. However, he first proposed that radiation absorption of vaporized fuel gas on condensed surface controls burning rate. He further concluded that it is necessary to develop fuel absorption coefficient database to handle the fuel rich core since radiation attenuates within the fuel core.

Modak [48] analyzed absorption coefficient and temperature distribution within the fuel rich core of a 0.73 m PMMA pool fire. Cross sectional temperature profiles showed a cool fuel rich core near the PMMA surface (from 0.02 m to 0.03 m thick). Absorption coefficient near the pool surface significantly increased at the center of the pool fire. As the fire size increases, absorption coefficient and species concentration within the fire became distributed non-homogeneously. Especially for large fires, non-isothermal and non-homogeneous conditions should be included to determine the incident heat flux to the fuel surface, which is proportional to fuel burning rate, when pool heating is ignored or very small.

Brosmer and Tien [49] assumed two separate zones exist in a fire; a relatively cool fuel rich core and a high temperature zone. They used 900 K and a gray absorption coefficient for fuel calculated from soot absorption in their fuel core, and 1350 K and the gray absorption coefficient of combustion products (CO_2, H_2O and soot) as their combustion region. Their prediction based on this two region model for mass evaporation rate of PMMA had good agreement up to 0.73 m pool diameter. Although their two region model predicted the fuel burning rate well, they stated non-isothermal and non-homogeneous assumptions should be incorporated as the fire size becomes larger.

Hamins et al. [2, 38] measured radial variation of mass burning rate, and radiative and net heat flux in pool fires of heptane (C_7H_{16}), toluene (C_7H_8), methanol (CH_3OH), and methylmethacrylate (MMA, $C_5H_8O_2$) with pools up to 0.38 m in diameter. Radiation heat transfer was measured to provide 96%, 80% and 55% of total heat feedback to the fuel source for 0.3 m diameter pool fires of toluene, n-heptane and methanol respectively. The intensity was distributed uniformly on the pool for toluene, was slightly decreased toward to pool edge (approximately 25 % less than at the center) for heptane, and reduced gradually quarters of the pool diameter (approximately 25 % less than at the center) and significantly dropped toward to the pool edge (approximately 85 % less than at the center) for methanol. The highest radiation intensity for all fuels was observed at the center of the pool. The paper also concluded that all pool fires with 0.3 m < D < 1 m have a small convection effect on energy feedback (< 20 %), and the radiation dominates completely the energy feedback to the fuel surface of larger pool fires.

Gritzo et al. [50] investigated energy feedback of a large JP-8 pool fire (20 m diameter) under several wind conditions both experimentally and numerically. Their radiation heat flux distribution and fuel burning rate were affected by wind speed and wind induced vortices. They observed the lowest heat flux region was at the center of fuel surface. This is opposite to the result of small-scale fires by Hamins. As the fire size increases, the fuel rich core with soot increased the relatively cold temperature region and resulted in the lowest heat flux at the center of the pool. The lowest heat flux region was also shifted by the wind speed from the center toward to the pool edge. The magnitude of lowest and highest heat flux increased with wind speed. The existence of a fuel rich core

region was confirmed by their low wind velocity test, and fuel and soot radiation absorption reduced the radiation heat flux on the fuel surface.

Klassen et al. [37] measured local radiation intensity and transmissivity of small toluene pool fire (D = 7.1 cm) as a function of radial and height position using a He-Ne laser and two band pass filters. Based on the intensity and transmissivity measurements, they estimated local temperature and soot volume fraction. Results showed little emission near the pool surface at height 1.4 cm and radial distance 40% from the center at 2.8 cm from the pool surface. As the height from the surface increased, the highest radiation intensity position shifted closer to the pool center. They also observed visually that soot particles near the pool surface moved up and down with a low frequency motion. Soot volume fraction estimated by transmission measurement showed that almost the same amount of soot at the flame tip was above the pool surface. Low emissivity at the pool surface suggested that relatively cold soot and toluene fuel vapor absorption were blocking the radiation feedback from flame toward fuel surface.

Hostikka et al. [41, 51] used NIST's fire dynamics simulator (FDS) to model methanol and heptane pool fires. Since FDS did not at the time include methanol and heptane absorption information, methane absorption data was used instead absorption data for the two fuels. Six and nine separated band models were used to calculate Planck mean absorption coefficient, and incorporated into FDS to conduct radiation transport calculation. Fuel burning rate, radiative and convective heat fluxes as a function of pool diameter, and temperature distribution within the fire were reported. The fuel burning rate as a function of D showed qualitative agreement, but quantitavely overpredicted it. They commented that more absorption information and band models should be

investigated, and more than 20 grid cells should be set within the pool diameter to obtain good results.

Novozhilov and Koseki [42] developed a CFD model including both gas and liquid phase interface to calculate fuel burning rates of methanol, heptane, and toluene. Their model used a dense mesh at the gas and liquid interface and along the flame centerline. Their modeled data was compared to previous experimental data done by Hamins [38], Klassen [8], Janssen [52], and Koseki [53]. The prediction agreed qualitatively for mean flame temperature, fuel burning rate of different pool size, radiation heat flux on fuel surface, and radiation contribution to total energy feedback toward the fuel. The absorption coefficient calculation was done using a simple gray gas simple formula including all gases absorption according to Fletcher et al. [20]. Average error of a fuel burning rate was about 17%, and toluene fire had the worst discrepancy due to strong dependency on soot absorption.

1.1.2.2 Absorption coefficient measurements

Many researchers have conducted temperature dependent absorption coefficient measurements since the 1960's. Most of the studies in the 1960's and 1970's were combustion product measurements such as carbon dioxide, carbon monoxide, water and methane. Ludwig's NASA report summarizes results for the 1970's [4]. Tien and his coworkers made great contributions in the 1980's on the absorption coefficient measurement on fuels such as methane, propylene, acetylene, and methyl-methacrylate [11-14]. Their spectral resolution permitted the use of wide band and narrow band models

to optimize line broadening and temperature dependency of infrared spectrum. Their data is still used to calculate radiation transport equation in combustion and fire simulations.

Grosshandler and his coworkers constructed the narrow band radiation absorption coefficient database "RADCAL" [46] in 1993 based on Ludwig's report and the date of Tien et al. Current fire modeling programs such as FDS use this program to tabulate radiation absorption coefficient as a function of temperature and species concentration. HITRAN and HITEMP database [6, 18] edited by Rothman is also currently used to calculate absorption coefficients. HITRAN has line-by-line spectral information for 37 species and its accuracy has been verified with experiments up to 600 K. HITEMP has three combustion product species (H_2O, CO_2 and CO), with spectral information experimentally verified up to 1000 K. The HITEMP database will be used to make a new radiation absorption coefficient database for H_2O, CO_2 and CO as a part of this thesis

Tien and his coworkers measured temperature dependent infrared spectra of acetylene (C_2H_2), methane (CH_4), propylene (C_3H_6), and methyl methacrylate (MMA, $C_5H_8O_2$) [11-14]. They constructed a simple infrared spectrometer with a globar source, a chopper, a monochromometer, a gas cell with a temperature controlling furnace, and infrared windows. Two combinations of infrared windows were used; Barium Fluoride (BaF_2) and Sodium Chloride (NaCl) windows for short wavelengths, and Potassium Bromide (KBr) for long wavelengths. Low-resolution infrared spectra were analyzed by both wide and narrow band models to correlate low-resolution data to high resolution ones. Their work includes temperature dependent infrared spectra, wide band and narrow band fitting parameters, and Planck mean absorption coefficients. They found that a statistical narrow band model with equal spacing (Elasser model) gave good agreement

with high-resolution data for methane. The data are still used to calculated radiative transport of fuels 30 years later.

Fuss et al. measured the infrared spectra of methane (CH_4) with 4 cm^{-1} resolution from 296 K to 900 K [15]. They used an FTIR and a temperature controlled gas cell like Tien. Infrared spectra were obtained by the instrument with BaF_2 windows and 4 cm^{-1} and 32 cm^{-1} resolution. They investigated the effect of resolution on Elasser's narrow band parameters. They found that band resolution impacts individual narrow band parameters, but the results showed that total (integrated) absorptivity did not have a strong dependency on spectral resolution. They concluded that resolution dependency impacts the modeling the absorptivity of multi component gas mixtures. Fuss et al. also reported temperature dependent ethane (C_2H_6), propane (C_3H_8) and butane (C_4H_{10}) spectra [16], in addition to methane, with the same temperature condition. Universal functions on total absorptivity for four fuels as a function of temperature were established and correlated with their experiment results. Two formulas for each species were distinguished due to optically thin and thick condition. The results showed that total absorptivity per unit C-H bond of ethane, propane, and butane were similar, but that of methane was about 40% and 60% lower than the other three species at 296 K and 900 K, respectively.

1.2   Vibration and rotation infrared spectroscopy principle

Radiation absorption coefficients for any gas species can be related to molecular structure and modes of energy storage in the individual molecules. A molecule has four modes of energy states such as translational, electronic, rotational and vibrational. All

energy modes are quantized, which means that transitions between two discrete energy levels shown in Figure 1-1 are associated with absorption or emission of photons at particular energy levels of frequency. When the ground energy level of a molecule, say E_1, jumps up to one energy level higher, say E_2, the molecule absorbs photons with certain energy ΔE (= E_2 - E_1). The same amount of energy ΔE is emitted in a photon when the higher energy level returns to the original level. These two processes are called "absorption" and "emission", respectively. Absorption and emission from translational energy transitions occur at such low energy due to the closely packed nature of the energy levels, translational energies do not impact absorption or emission relevant for radiative heat transfer.
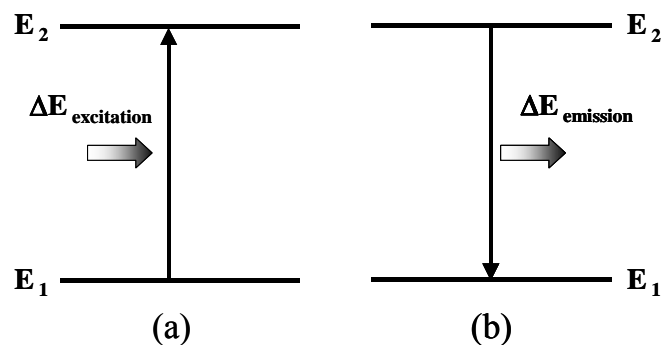
Figure 1-1: Energy transition due to absorption and emission: (a) Absorption and (b) Emission.

Induced emission shown in Figure 1-2 is different from the previous emission process. This emission is caused as follows: when the photons from a certain direction with the same frequency as quantized energy transition strike (encounter) a molecule with an excited energy state, and the molecule emits a photon in the same direction and frequency as the stimulating photon.
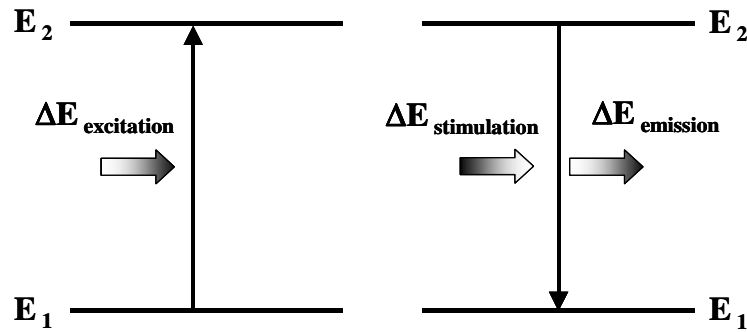
Figure 1-2: Energy transition due to induced emission.

The theory of vibration and rotational spectroscopy is summarized in Banwell and McCash [54], and Modest [47], respectively. Max Planck introduced Planck constant h to relate the energy transition ΔE to photon frequency v (s^{-1}).

$$\Delta E = hv \qquad (1.1)$$

Since the amount of energy due to state transition is different for each electric, rotational, and vibrational modes ($\Delta E_{rot} < \Delta E_{vib} < \Delta E_{elec}$), a frequency for each mode can be easily calculated by eqn. 1.1. In spectroscopy, wavenumber $\bar{v}$ (cm^{-1}) and wavelength λ (μm) are commonly used to describe an electromagnetic wave. The definition of wavenumber and wavelength are:

$$\bar{v} = \frac{v}{c} \times 100 = \frac{E}{hc} \times 100 \qquad (1.2)$$

$$\lambda = \frac{10000}{\bar{v}} = \frac{hc}{E} \times 100 \qquad (1.3)$$

12

1.2.1   Vibration with harmonic oscillator model

A chemical bond between two atoms can be represented to a first approximation by a mass-spring system, which gives a harmonic oscillator. The harmonic oscillator potential energy well is parabolic, which only works as a good approximation for relatively low energy levels near the ground state shown in Figure 1-3. Since the harmonic oscillator assumes that vibration between two atoms in a molecule has displacement, for instance a diatomic molecule, the Schrödinger wave equation is applied to calculate vibrational energy between two atoms. Also, a vibrating spring obeys Hooke's law. Combination of the Schrödinger and Hooke's equations gives the quantized vibrational energy equation.

One-dimensional Schrödinger wave equation for the potential well $V(x)=1/2*k(x-x_0)^2$ gives

$$\frac{d^2\psi}{dx^2} + \frac{2\mu}{\hbar}\left[E - \frac{1}{2}kx^2\right]\psi(x) = 0 \qquad (1.4)$$

where E(x): Total energy for a harmonic oscillator.

$\hbar$: Modified planck constant (=h/2π).

μ: Reduced mass.

ψ(x): Spatial amplitude of the wave.

The energy level in equation 1.4 serves as an eigenvalue for the differential equation and solutions for ψ(x) only exist at discrete value of E given by equation 1.5.

$$E_{\upsilon} = \hbar\left(\upsilon + \frac{1}{2}\right)\sqrt{\frac{k}{\mu}} = h\left(\upsilon + \frac{1}{2}\right)\left(\frac{1}{2\pi}\sqrt{\frac{k}{\mu}}\right) = \left(\upsilon + \frac{1}{2}\right)h\nu \qquad (1.5)$$

where υ: Quantum number (υ= 0, 1, 2, 3….)

Since the Schrödinger equation only permits energy transition between two adjacent energy levels, so called "specific selection rule ($\Delta\upsilon = \pm 1$)", the vibrational energy transition due to absorption and emission is given as:

$$\Delta E_{absorption,\upsilon \to \upsilon+1} = E_{\upsilon+1} - E_{\upsilon} = h\nu \qquad (1.6)$$

$$\Delta E_{emission,\upsilon+1 \to \upsilon} = E_{\upsilon} - E_{\upsilon+1} = -h\nu \qquad (1.7)$$
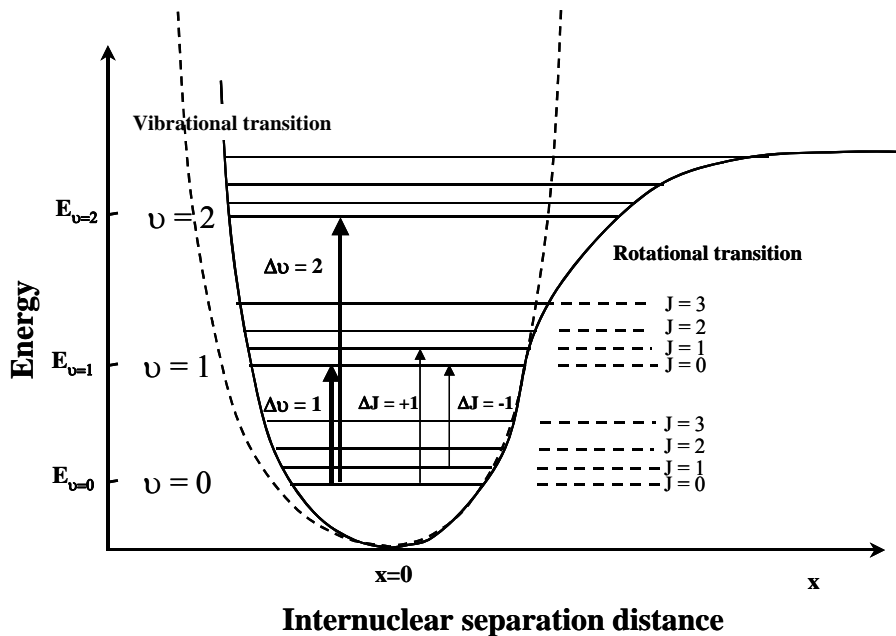
Figure 1-3: Potential energy curve for anharmonic oscillator; anharmonic oscillator (—), harmonic oscillator (----).

1.2.2 Rotation

The energy levels of a rigid rotator are assumed to explain rotational motion of a diatomic molecule. Two atoms have their own mass m_1 and m_2, and fixed separation distance from the center of two masses, respectively. When the diatomic molecule rotates about the center of the two masses at a frequency ν_r, kinetic energy K of the rotator is expressed as:

$$K = \left(\frac{1}{2}m_1 r_1^2 + m_2 r_2^2\right)\omega^2 = \frac{1}{2}I\omega^2 = \frac{1}{2}\mu r^2 \varpi \qquad (1.8)$$

where I is the moment of inertia and μ is the effective reduced mass.

The Schrödinger equation for a rigid rotator with polar coordinates θ and ϕ is

$$-\frac{\hbar^2}{2I}\left[\frac{1}{\sin\theta}\frac{\partial}{\partial\theta}\left(\sin\theta\frac{\partial}{\partial\theta}\right) + \frac{1}{\sin^2\theta}\left(\frac{\partial^2}{\partial\phi^2}\right)\right]Y(\theta,\phi) = EY(\theta,\phi) \qquad (1.9)$$

Solving this partial differential equation gives eigenvalues for E as follows:

$$E_{rot} = \frac{\hbar}{2I}J(J+1) \qquad (1.10)$$

where, J is Rotational quantum number (J=0, 1, 2, 3...).

The energy due to absorption and emission between two adjacent rotational energy levels (J and J+1) by the selection rule are written as

$$\Delta E_{absorption, J \to J+1} = \frac{\hbar^2}{I}(J+1) = \frac{h^2}{4\pi^2 I}(J+1) = 2Bh(J+1) \qquad (1.11)$$

$$\Delta E_{emission, J+1 \to J} = -\frac{\hbar^2}{I}(J+1) = -\frac{h^2}{4\pi^2 I}(J+1) = -2Bh(J+1) \qquad (1.12)$$

where B is rotational constant ($B = \frac{h}{8\pi^2 I}$).

1.2.3 Vibration-Rotation with harmonic oscillator

Simple rotational transitions for most low-lying states occur at frequencies in the microwave region, and they are not as important in radiative heat transfer as vibrational transition. However, when a molecule absorbs photons at vibrational transition, rotational transition may also be simultaneously induced. This so-called "Vibration-Rotation" transition plays a significant role for spectral broadening of a vibrational absorption band, and impacts the radiation transport calculation. Total energy by vibration and rotation is

$$E_{vib} + E_{rot} = \left(\upsilon + \frac{1}{2}\right)h\nu + 2BhJ(J+1) \qquad (1.13)$$

where, $\upsilon = 0, 1, 2, 3\ldots$ and $J = 0, 1, 2, 3\ldots$

When a molecule absorbs radiation, two combinations of selection rule for vibration-rotation are considered; (1) $(\upsilon, J) \to (\upsilon+1, J+1)$ and (2) $(\upsilon, J) \to (\upsilon+1, J-1)$.

Transition energy of selection rules (1) and (2) is expressed in terms of frequency and wavenumber as

For rule (1),

$$\Delta(E_{vib} + E_{rot}) = hv + 2Bh(J+1) \qquad (1.14)$$

$$\frac{\Delta(E_{vib} + E_{rot})}{hC_0} = \bar{v} + 2\bar{B}(J+1) \qquad (1.15)$$

For rule (2),

$$\Delta(E_{vib} + E_{rot}) = hv - 2BhJ \qquad (1.16)$$

$$\frac{\Delta(E_{vib} + E_{rot})}{hC_0} = \bar{v} - 2\bar{B}J \qquad (1.17)$$

Since typical values of $\bar{v}$ and $\bar{B}$ are about the order of 10^3 cm^{-1} and 1 cm^{-1}, energy level spacing associate with rotational levels is 1/1000 of the vibrational levels shown in Figure 1-3.

1.2.4 Vibration with anharmonic oscillator model

In previous sections, the harmonic oscillator model was introduced to simply understand the relationship between molecule motion and energy transition. However, in reality the molecule has anharmonicities because of the non-parabolic nature of the true energy well as indicated in Figure 1.3. One potential energy curve for approximations anharmonic oscillator transitions is the Morse function as:

$$E = D_{eq}[1 - \exp(ax)]^2 \qquad (1.18)$$

where a is a constant for a particular molecule and D_{eq} is the dissociation energy between two atoms. Substituting the potential energy on anharmonic oscillator into Schrödinger equation in eqn. 1.4, vibrational energy on anharmonic oscillator at different energy levels is found to be as polynomial form:

$$\overline{E}_{vib} = \left(\upsilon + \frac{1}{2}\right) - \left(\upsilon + \frac{1}{2}\right)^2 x_e + \left(\upsilon + \frac{1}{2}\right)^3 x_e - \cdots \qquad (1.19)$$

where x_e is anharmonic constant (approx. = 0.01)

This expression gives unequally spaced vibrational energy levels, and the selection rule on anharmonic oscillator can expand to $\Delta\upsilon = \pm1, \pm2, \pm3\ldots$. Each transition $\upsilon = 0 \rightarrow 1$, $\upsilon = 0 \rightarrow 2$, and $\upsilon = 0 \rightarrow 3$ is named fundamental, first overtone, and second overtone, respectively. However, the overtones progressively becomes less intense with higher Δv.

1.2.5   Vibration-Rotation with anharmonic oscillator

As for the harmonic oscillator model, the total energy by vibrational and rotational mode is expressed as:

$$\overline{E}_{tot} = \overline{E}_{vib} + \overline{E}_{rot} \qquad (1.20)$$

Rotational energy for the anharmonic oscillator is

$$\overline{E}_{rot} = \overline{B}J(J+1) - \overline{D}J^2(J+1)^2 + \overline{H}J^3(J+1)^3 - \cdots \qquad (1.21)$$

and the selection rule for this rotational transition is $\Delta J = \pm 1$. Substituting $\overline{E}_{rot}$ and $\overline{E}_{vib}$ into total energy equation, equation 1.20 becomes:

$$\overline{E}_{tot} = \left(\upsilon + \frac{1}{2}\right) - \left(\upsilon + \frac{1}{2}\right)^2 x_e + \left(\upsilon + \frac{1}{2}\right)^3 x_e - \cdots \overline{B}J(J+1) - \overline{D}J^2(J+1)^2 + \overline{H}J^3(J+1)^3 - \cdots$$

(1.22)

Rotational spectrum induced by vibration comes out on both the left from the band center (P branch, $\Delta J = -1$) and the right from the band center (R branch $\Delta J = +1$). Rotational-vibrational spectrum ($\upsilon=0\rightarrow1$) of HCl is shown in Figure 1-4 as an example, which presents the P and the Q branches.
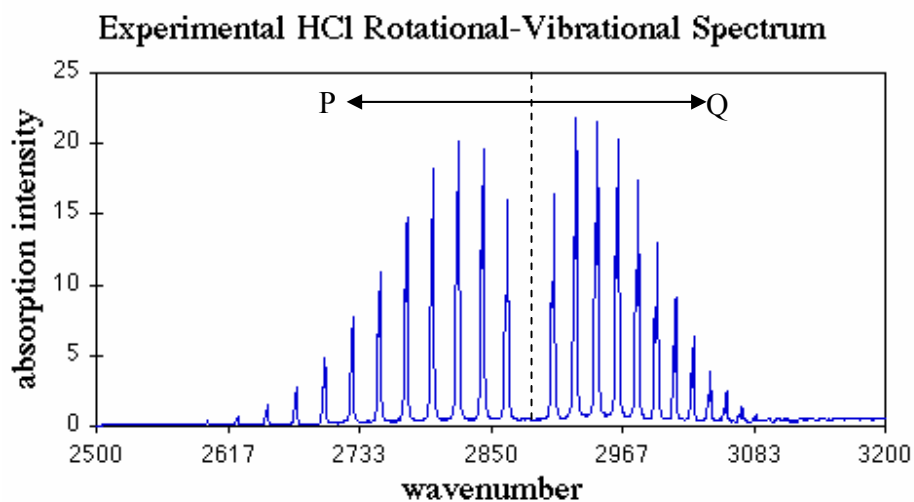
Figure 1-4: Rotational-vibrational spectrum ($\upsilon=0\rightarrow1$) of the P and the Q branches of HCl.

1.2.6   Vibration and rotation of a polyatomic molecule

When two atoms in a molecule bond have different electronegativity, a dipole moment between the two atoms forms due to a charge distribution imbalance. Infrared absorption happens if the dipole moment is non-zero, but not if the dipole moment is zero. For example, in C-Cl bonds, chlorine has more electronegativity than carbon so chlorine plays negative and carbon is positive within a dipole moment. In C-H bonds, carbon plays negative and hydrogen is positive. However, homonuclear diatomic molecules like H_2, N_2, and O_2 do not have dipoles because nuclei equally attract. One of vibration motions of a diatomic molecule CO_2, also doesn't have infrared absorption since the net dipole vector is zero.

A polyatomic molecule has 3 (non-linear molecule) and 2 (linear molecule) degrees of freedom for rotational, and 3N-6 (non-linear molecule) and 3N-5 (linear molecule) degrees of freedom for vibrational modes (where, N is the number of atoms). Within the vibrational mode, N-1 is for vibrational stretching and 2N-5 or 2N-4 are for vibrational bending. For example, methane (CH_4, N=5) has 6 degrees of freedom for vibration: three for stretching and also three for bending. Since the frequency of each different bond is unique, the characteristic band group of stretching and bending motion of bonds are tabulated and applied to identify the chemical bond and motion within a molecule.

1.3   Line broadening

Theoretical emission or absorption takes place monochromatically at a frequency v_0 obtained by energy transition. Line distributions cause peaks to occur over a range of

frequencies. Line broadening and overlap, can arise from collision, Doppler and natural broadenings. The width of the distribution is dependent on temperature, pressure (population of molecules), and pathlength, and impacts the total amount of energy absorbed by a molecule.

1.3.1 Collision broadening

For fire temperatures up to 2000 K, collision broadening is the most important broadening of the three broadenings. Since the molecule is releasing electro magnetic waves continuously, molecular collisions disrupt the wave and changes the phase. Although the collision doesn't change the frequency of transition, it changes the phase of the electromagnetic wave at a transition frequency.

An absorption coefficient κ_v including collision broadening gives a Lorentzian profile with respect to v, which is expressed by

$$\kappa_v = \frac{S}{\pi} \frac{b_c}{(v - v_0)^2 + b_c^2} \qquad (1.23)$$

where S is line intensity, b_c is line half width with a collision broadening, v_0 is the center of the line spectrum, and v is an arbitrary wavenumber within the Lorentzian profile. The line half width b_c is calculated from kinetic theory as

$$b_c = b_{c0} \left(\frac{p}{p_0} \right) \left(\frac{T_0}{T} \right)^{1/2} \qquad (1.24)$$

where subscript 0 is standard condition. The line half width of collision broadening increases with pressure P, but decreases with temperature.

1.3.2 Doppler and Natural broadening

Doppler broadening happens at high temperatures (high velocity), and low pressures (low probability of collision). Comparing the frequency of the transition and the one due to molecular velocity, a slight shift of frequency happens while the molecule is moving in the line of sight, and the Doppler effect results in the broadening of the line width spectrum. Doppler broadening has a Gaussian profile due to the molecule velocity. Since the lifetime of excitation (10^{-4} to 10^{-5} second) results in a line width on the order of 10^{-7} cm^{-1}, and thus natural broadening is not relevant for radiation absorption calculations.

1.4 Absorption coefficient

1.4.1 Absorption coefficient theory

According to the Beer Lambert law, the absorption coefficient, κ_ν, at any wavenumber, ν, can be expressed in terms of measurable quantities as

$$\kappa_\nu = \frac{-\ln(\tau_\nu)}{pL} \qquad (1.25)$$

where τ_ν is the spectral transmittance, p is the partial pressure of the absorbing specie (Pa), and L is the measurement path length (m). From a fundamental perspective [55],

the absorption coefficient is the product of line intensity (S), line shape ($g(\nu-\nu_0)$) and the number of absorbing molecules per unit volume and pressure:

$$\kappa_\nu = S \cdot g(\nu - \nu_0) \cdot N_L \cdot \left(\frac{296}{T}\right) \qquad (1.26)$$

where ν_o is the center of an absorbing line in wavenumber and N_L is Loschmidts' number ($N_L = 2.447 \cdot 10^{19}$ molecules/cm^3/kPa at 296 K). For applications at atmospheric pressure and moderate temperatures, the Lorentzian line shape is generally applied assuming broadening is dominated by collisions;

$$g(\nu - \nu_0) = \frac{\left(\gamma_p/\pi\right)}{\left(\nu - \nu_0\right)^2 + \gamma_p^2} \qquad (1.27)$$

where γ_p is the pressure (collision)-broadened line half width:

$$\gamma_p = g \cdot \left(\frac{296}{T}\right)^n P_t \cdot \qquad (1.28)$$

where P_t is the total pressure, g is a broadening parameter (cm^{-1}/kPa), and n is the air-broadened linewidth parameter. The line intensity (S) corresponds to the product of the quantum mechanical probability for the transition and the population difference between the initial (absorption) and final (emission) states [10]:

$$S = \frac{\left\{\dfrac{8 \cdot \pi^3}{3hc}\right\} \cdot \upsilon \cdot \left\{\dfrac{\left|\vec{R}\right|^2}{g_l}\right\} \cdot g_i \cdot I_a \cdot \left[1 - \exp\left(-\dfrac{hc\nu}{kT}\right)\right] \cdot g_l \cdot \exp\left(-\dfrac{E'}{kT}\right)}{Q \cdot 10^{36}} \qquad (1.29)$$

Here, h and k are the Planck and Boltzmann constants, respectively, c is the speed of light, E' is the energy of the lower state, $\vec{R}$ is the transition moment, and hcv is the difference in energy between the upper and lower states. The second bracketed term is the quantum mechanical transition probability, where g_l is the degeneracy of the lower state. Finally, I_a is the isotope fraction, g_i is the nuclear spin degeneracy, and Q is the rotational partition sum. Combining eqns. (1.26) to (1.29) yields:

$$k_\nu = \frac{\left\{\dfrac{8 \cdot \pi^3}{3hc}\right\} \cdot v \cdot \left\{\dfrac{|R|^2}{g_l}\right\} \cdot g_i \cdot I_a \cdot \left[1 - \exp\left(-\dfrac{hc\nu}{kT}\right)\right] \cdot g_l \cdot \exp\left(-\dfrac{E'}{kT}\right) \cdot \dfrac{g}{\pi} \cdot \left(\dfrac{296}{T}\right)^n \cdot P_t \cdot N_L \cdot \left(\dfrac{296}{T}\right)}{Q \cdot 10^{36} \cdot \left[(\nu - \nu_0)^2 + \left(g \cdot \left(\dfrac{296}{T}\right)^n \cdot P_t\right)^2\right]}$$

$$(1.30)$$

where P_t is the total pressure and g is a broadening parameter (cm^{-1}/kPa).

1.4.2   Temperature dependence on absorption coefficient

As temperature increases, absorption coefficients decrease around the band peaks but increased broadening due to rotational transitions can cause a rise in the band wings. The band peak decreases because the higher vibrational states become more probable with higher temperatures.

Spectral absorption coefficient in equation 1.30 at band center has contribution of rotational partition function Q, quantum mechanical probability of energy transition, probability of lower energy state to higher energy state, collision broadening band width, and the number of absorbing molecule decrease absorption band peaks at high temperature. Rotational partition function Q on denominator is proportional to T (m = 2 rotational degrees of freedom) in a linear molecule and $T^{3/2}$ (m = 3) in a nonlinear molecule [18]. For the first exponential term, energy absorption due to the quantum mechanical energy transition exponentially decreases, since induced emission exponentially increases with temperature. Induced emission happens when the photons from a certain direction with the same frequency as quantized energy transition strike (encounter) a molecule with an excited energy state. For the second exponential term, the probability of energy absorption from lower energy state to higher energy state also decreases exponentially. Since a molecule with highly excited energy state increases with temperature. Broadening parameter term and the number of absorbing molecule decreases as a function of 1/T. All contributions described above decrease the absorption coefficient with temperature. In contrast, absorption coefficient at band wings increases with temperature. This is because the largest population of rotational energy states shifts higher as temperature increases, and vibrational energy transition at higher energy states "hot bands" happens at high temperature.

1.5   Problem description

Figure 1-5 shows the temperature and fuel contour plots of a heptane 1m pool fire calculated by FDS. The line represents temperature, and the filled plot represents fuel

volume fraction. There is a cool fuel rich core above the fuel surface temperature ranging from 400 K to 800 K, which is consistent with Brosmer [7] and Klassen's [8] condition. Radiation is most likely attenuated within this fuel core, and transmitted radiation reaches the liquid or solid fuel bed. Since fuel radiation absorption is not well studied, radiation properties of fuel species from low temperature to high temperature are needed to calculate radiation attenuation within the fuel core.
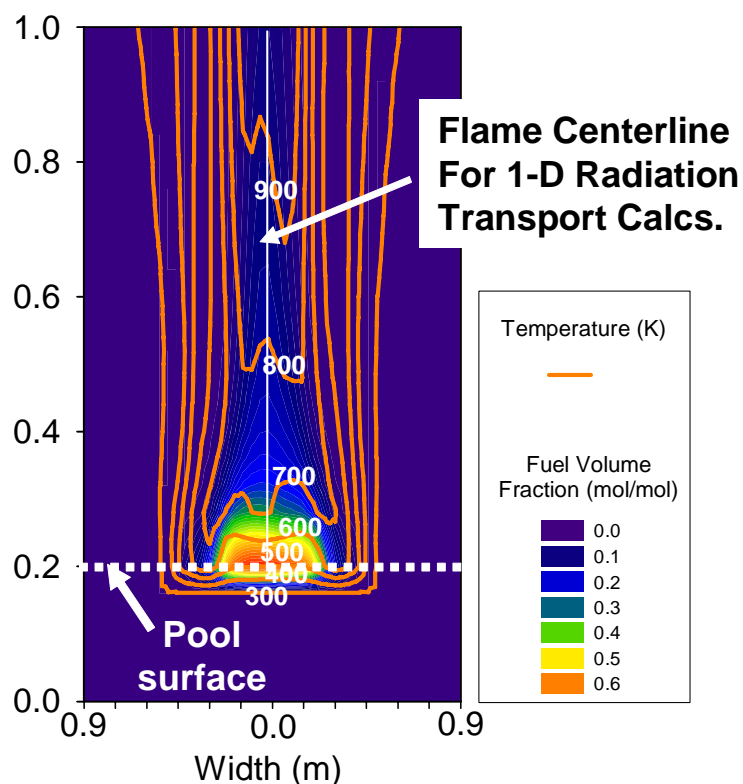
Figure 1-5: Temperature/Fuel contour plot of 1m Heptane pool fire using NIST Fire Dynamics Simulator

Table 1-1 is an example of an absorption coefficient database currently used in combustion calculations. Previous databases contain combustion product information for carbon dioxide, water, and carbon monoxide. However, methane is the only fuel gas in the databases. This small gas molecule information is not adequate to calculate radiation

absorption of more complex fuel molecules such as heptane, methanol and toluene. Different chemical structure will give differences in radiation absorption characteristics compared to methane and ethane. Additional fuel absorption data is necessary for accurate calculations of energy feedback study in fire.

Table 1-1: An example of an absorption coefficient database currently used in combustion calculation

Database	HITEMP	RADCAL
Author	Rothman et al. (2003)	Grosshandler (1993)
Temperature	Up to 2000K	Up to 2000K
Species	3	5
Combustion products	CO_2, H_2O, CO	CO_2, H_2O, CO, Soot
Fuel	N/A	CH_4
Key point	Accurate, but needs many parameters	Moderate accuracy, low resolution

1.6   Objective and brief summary of the thesis

The objective of this thesis is to 1) measure infrared spectra of fuel species, namely propane (C_3H_8), n-heptane (C_7H_{16}), propylene (C_3H_6), methanol (CH_3OH), toluene (C_7H_8), and methyl methacrylate (MMA, $C_5H_8O_2$), using a high temperature FTIR test rig in a unique experimental facility that enables measurements to 1000 K, 2) develop a simple extrapolation technique for absorption coefficient to high temperature, and verify the extrapolated results with HITEMP [6] and experimental data using the high temperature FTIR test rig, 3) build an absorption coefficient database RADCAL2 with the updated data of combustion products from HITEMP and fuels from experiment and existing data for methane (CH_4) obtained from the HITRAN [18] database, and 4)

investigate the contribution of fuel radiation absorption on radiation feedback to the fuel surface using line of sight one dimensional radiative transport equation and FDS.

A brief summary of this dissertation is given below. In chapter 2, the experimental apparatus used to obtain high temperature FTIR is described. Thermal properties and spectral characteristics of infrared windows are evaluated. A window cooling unit designed and installed in a gas cell is described. Cooling effect on the infrared window evaluated by temperature measurement on the windows.

In chapter 3, infrared spectra of gas and liquid fuel species measured by high temperature FTIR apparatus are presented. Propane, heptane, methanol, toluene, propylene and methyl methacrylate (MMA) infrared absorption coefficients are presented as a function of temperature up to 1000 K. A simplified extrapolation technique for absorption coefficient proposed by Fuss is evaluated by HITEMP database and propane spectrum. Fuel pyrolysis at high temperature is calculated by CHEMKIN AURORA using detailed kinetic mechanisms to determine fuel pyrolysis during high temperature infrared measurement and thereby influences results.

In chapter 4, new absorption coefficient database is created. Combustion products absorption coefficient calculated by E-trans with HITEMP, modeling of soot absorption, and fuel absorption coefficients as a function of temperature calculated by extrapolation and interpolation using simplified extrapolation equation described in chapter 3 are shown. Planck mean absorption coefficient of measured fuels and methane from the HITRAN database are calculated and fit to fourth order polynomial of Planck mean absorption coefficient as a function of temperature are given.

In chapter 5, contribution of combustion products and fuel for radiation feedback to fuel surface are investigated by solving the one dimensional radiative transport equation with new absorption coefficient database. Mole fraction of gas species and soot volume fraction are calculated from FDS with old absorption coefficient data, and the concentration data are input to solve radiation intensity on fuel surface. The result of radiation intensity by new database and RADCAL are compared for methanol, heptane, and toluene 0.3 m pool fires. Also, radiation transport at gas and condensed phase interface are discussed by comparing infrared spectra of both phases.

Finally, a summary of this dissertation and future work are presented.

CHAPTER 2   EXPERIMENTAL APPARATUS

2.1   Introduction

For radiation feedback study in a fire, radiation absorption coefficients of fuels from low temperature to high temperature in addition to combustion products are very important to understand how radiation attenuates within the fire. Although absorption coefficient of combustion products such as H_2O, CO_2, CO and soot have been studied for a long time over wide temperature ranges, absorption coefficient for fuels are not well known. Tien and his coworkers [11-14] and Fuss et al. [15, 16] studied hydrocarbons and methyl methacrylate. However, Tien's data, which has been used for more than 20 years, are not highly resolved. Updated absorption coefficients of Tien's fuels and other new fuels over a wide temperature range are necessary to model accurate radiation feedback within a fire. High-resolution infrared spectrum measurements at high temperature is challenging because the infrared windows must keep its transparency to obtain a high resolution infrared spectrum over many scans. In this study, a Fourier transform infrared spectrometer with unique window cooling system is developed, in order to accomplish high temperature infrared measurement for various fuels. In this chapter, the unique FTIR system and gas and liquid fuel absorption coefficient measurement technique is described here.

2.2   Challenges of high temperature absorption measurement

Transmissivity of infrared window materials along the infrared beam path need to be carefully considered in order to take measurements of infrared spectroscopy at high

temperature. Table 2-1 shows thermal properties of window materials, which are commonly used, in infrared spectroscopy. Many infrared materials lose their optical properties from 600 K to 700 K due to oxidation, attack by steam, or thermal degradation. Even if the infrared material maintains its transmissivity at high temperature, the material cuts off spectral transmissivity at several important band groups. For instance sapphire [Figure 2-1 (a)], which is typically used for space engineering, sustains its optical transmissivity up to 2000 K, which is applicable for our temperature range of interest. However, sapphire cuts off the spectrum below 1700 cm^{-1} (5.6 μm), which contains characteristics band groups of carbon double bonding, aromatic group, bending motion of C-H bending motion, etc. Similarly, quartz is not suitable to be used along our infrared beam path, but its high temperature stability makes it suitable for walls and tubes not in the optical path.

Zinc Selenide (ZnSe), chosen as the window in this thesis, has uniform transparency at mid- infrared range shown in Figure 2-1 (b) and has low thermal expansion. Low thermal expansion can prevent an infrared window from thermal shock during furnace cooling. However, ZnSe can only be used up to 600 K without thermal degradation and oxidation, and window-cooling line with inert gas is necessary for higher temperatures. Figure 2-2 shows a comparison between non-oxidized (clean) and oxidized ZnSe windows. The oxidized window changes its color from dark yellow (clean condition) to white. As the result of oxidation at high temperature, the window loses its optical transparency.

Table 2-1: Thermal properties of typical optical materials adopted from Ref. [56]

Material	Symbol	Thermal Conductivity	Thermal Expansion	Maximum Use Temp.	Comments
		mW/cm·K	·10^{-6}/K	°C	
Sodium chloride	NaCl	65	44	400	slightly sensitive to thermal shock
Potassium chloride	KCl	65	36	400	
Potassium bromide	KBr	48	43	300	sensitive to thermal shock
Calcium fluoride	CaF$_2$	97	19	600	
Strontium fluoride	SrF$_2$	83	18	~600	
Barium fluoride	BaF$_2$	117	18	500	sensitive to thermal shock
Sapphire	a Al$_2$O$_3$	240	8.4	1700	
Crystal quartz	a SiO$_2$	12	11	>1200	
Zirconia	ZrO$_2$	~19	~9	>1000	
Zinc sulfide	ZnS	272	6.4	300	
Zinc selenide	ZnSe	180	7.3	300	
Cadmium sulfide	CdS	159	4.6	~200	
Cadmium selenide	CdSe	?	4.9	>200	
Cadmium telluride	CdTe	63	4.5	300	opaque at high temperatures
Diamond	C	23200	0.8	>700	
Silicon	Si	1490	4.2	300	opaque at high temperatures
Silica glasses	vSiO$_2$	14	0.6	1070	immune to thermal shock

(a)

(b)
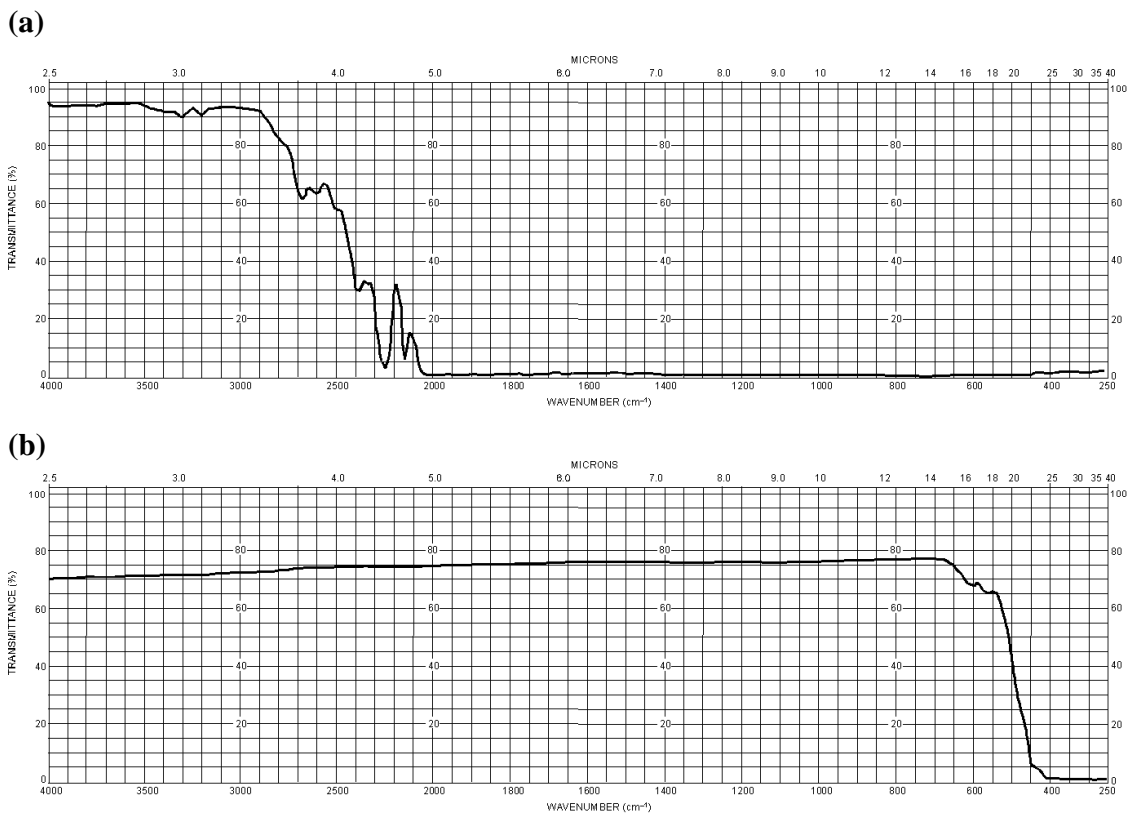
Figure 2-1: Spectral transmissivity of infrared materials: (a) sapphire and (b) zinc selenide.

(a)   **(b)**
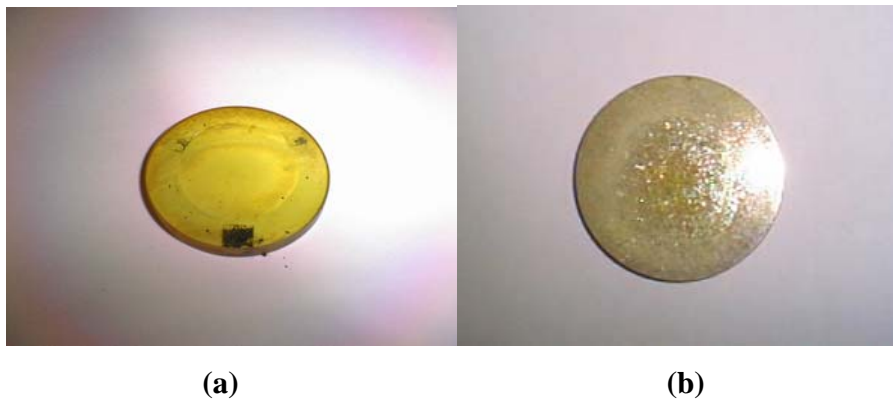
Figure 2-2: Picture of a zinc selenide window (a) clean and (b) oxidized at high temperature

2.3   Experimental setup

A Mattson Galaxy 7020 FTIR spectrometer was modified such that the IR beam from a globar source passed through the interferometer and was diverted from the internal sample compartment and along the axis of an external quartz flow cell. The flow cell was located inside a tube furnace, and the IR beam passed through the cell and into an external Mercury Cadmium Telluride (MCT) detector (MI0465, Graseby Infrared). The detected signal fed back to the FTIR, and a Fourier transform was used to generate the spectrum. Winfirst FTIR software by Mattson was used to operate the FTIR and analyze the infrared spectrum. Absorption spectra were measured at 1 cm^{-1} resolution with the signal averaged over 128 scans. A diagram and a picture of the experimental setup are shown in Figure 2-3 and Figure 2-4.

The entire optical path, including the spectrometer and external detector chamber was purged with N_2 (99.995 % min. purity) from a liquid nitrogen tank (200 liter) to eliminate absorption from ambient water vapor and CO_2. The interferometer was equipped with corner-cube optics which minimized the effect of sample emission on the transmission measurements [57]. This was confirmed by measuring the emission with the source blocked from the heated (1000 K) cell containing propane gas, which was found to be negligible.   The furnace (Lindberg/Blue M HTF53347C) had three heating zones designed to maintain a uniform temperature over the full length (31.75 ± 0.01 cm) of the cell (inner diameter = 2.54 cm).   Gas temperatures were measured with K-type thermocouples (probe diameter = 0.05 cm o.d.) at the inlet and outlet of the cell. The set point was adjusted to keep the inlet and outlet of gas line temperature within 5 K, which was considered acceptable for the purposes of this investigation. Temperature difference

34

at inlet and outlet was observed when the furnace temperature was low (400 K, 450 K, 500 K, and 600 K), and the set point was adjusted by monitoring the temperature on the data acquisition system. Before the infrared measurement at a given temperature, the furnace and cell condition were stabilized for 30 minutes. This lead time helped to yield a stable background spectrum, although the spectrum changed slightly during the measurement.

The ends of the quartz cell were sealed with zinc selenide (ZnSe) laser grade windows (0.3 cm thickness, ISP optics). Sealing between the ZnSe window and the quartz cell was performed using graphite gasket and high tension springs to absorb thermal expansion of the materials at high temperature. Although maximum temperature for ZnSe is reported to be 600 K [56], the ZnSe window (CVD grade, ISP optics) kept its transparency up to 700 K. To prevent oxidation of the ZnSe, the temperature of the windows was kept below about 700 K by directing a jet of N_2 on the outside of the windows as indicated in Figure 2-3. This cooling permitted high-resolution infrared measurement at high temperature with many scans. The pressure inside the cell was monitored by an absolute pressure transducer (Omega engineering, PX303-050) and regulated to maintain 101 kPa $\pm$ 1 kPa during the measurements.

Convection cooling with nitrogen jet gas from a liquid nitrogen tank (200 liter) on the window center was incorporated into the FTIR test rig. Figure 2-5 shows a picture of the cooling line. Stainless tube (O.D. 1/4") was welded at on angle of 30 degree to the center of a ZnSe window from outside of the gas cell. After cooling the window, the nitrogen pushed out air within beam path of a stainless tube and prevented carbon dioxide and water vapor from affecting the infrared spectrum.
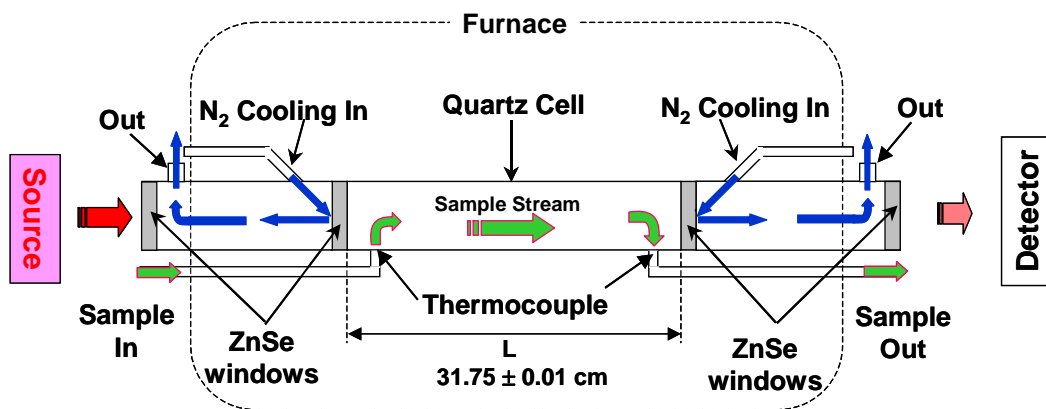
Figure 2-3: Diagram of the high temperature test rig.

Figure 2-4: Picture of high temperature FTIR test rig.
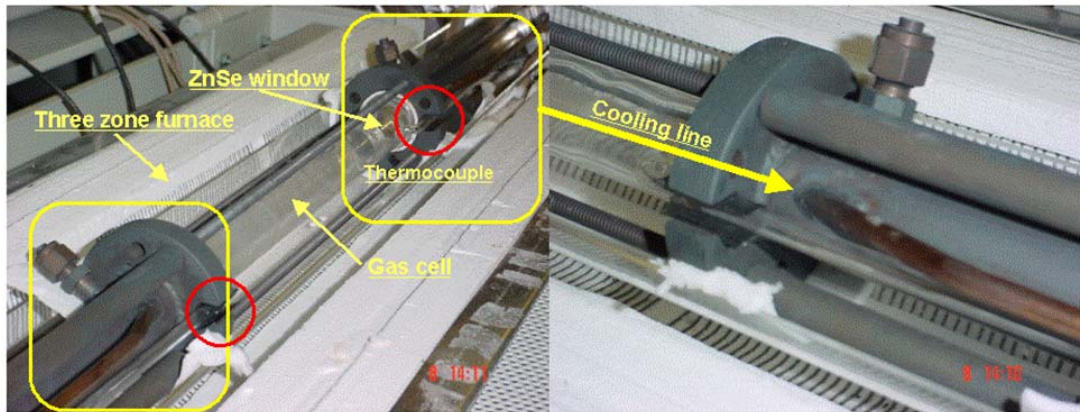
Figure 2-5: Picture of experiment setup, Left: Entire setup, Right: Cooling line.

To find the proper cooling gas volume flow rate (velocity), K-type thermocouples were temporarily installed on the ZnSe window with zirconia's based adhesive (Cotronics Co. Ltd., type: RESBOND 940). Figure 2-6 shows the picture of temperature measurement on the ZnSe window. In order to verify that this did not affect the gas temperature within the gas cell, gas temperature measurement was conducted by traversing a K-type thermocouple wire from the inlet to outlet of the gas cell. Figure 2-7 shows the gas temperature within the cell and Figure 2-8 shows the inside and outside of ZnSe window temperature. These figures indicate that the cooling system did not affect the gas temperature on the streamline within the cell, while keeping the window temperature below the temperature limit. However, the temperature on the inside surface was lower than gas temperature on the streamline. There was a small temperature gradient. Temperature gradient effect on absorption coefficient will be discussed in the next chapter.

Figure 2-6: Temperature measurement of a ZnSe window with a K-Type thermocouple.
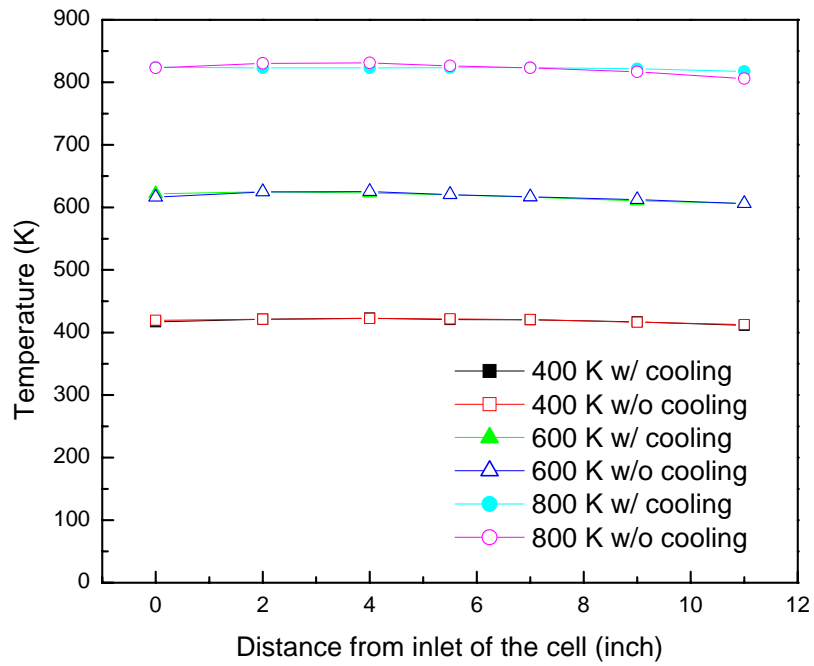
Figure 2-7: Temperature distribution within a gas cell.
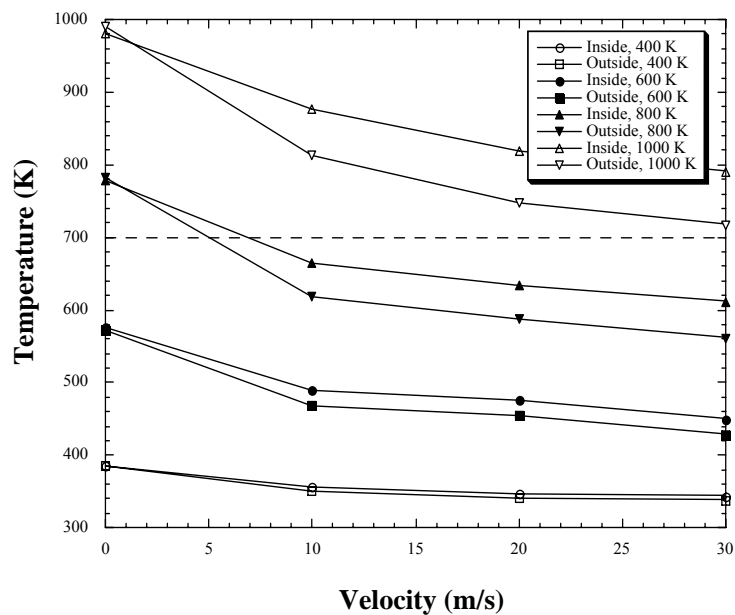
Figure 2-8: Window temperature as a function of cooling velocity.

2.4   Window cooling effect on the absorption coefficient

To estimate the uncertainty of variations in absorption coefficient due to temperature variation near the cooled windows, effective absorption coefficients were calculated based on the measured axial temperature profile with window cooling and compared to the absorption coefficients found assuming a uniform temperature in the gas cell.   The analysis was performed using Beer's law for the uniform temperature, which can be expressed as Beer's law of uniform temperature for entire beam path is expressed as:

$$I(L) = I(0)\exp(-\kappa P L) \qquad (3.1)$$

Figure 2-9 shows the elements based on temperature measurement, and Table 2-2 shows the temperature used for this uncertainty analysis. Uniform medium pressure P for each element was assumed. Based on this assumption, equation 3.1 can be modified as:

$$I(L) = I(0)\exp\left[-\left(2\kappa_1 PL_1 + \kappa_2 PL_2\right)\right] \qquad (3.2)$$

where, coefficient 2 on absorption coefficient κ_1 represents that the same temperature gradient near the window for both side is assumed as a result of temperature measurement. Using equation 3.2, HITEMP carbon dioxide data was used to estimate the uncertainty of absorption coefficient due to window cooling for 600 K, 800 K and 1000 K.
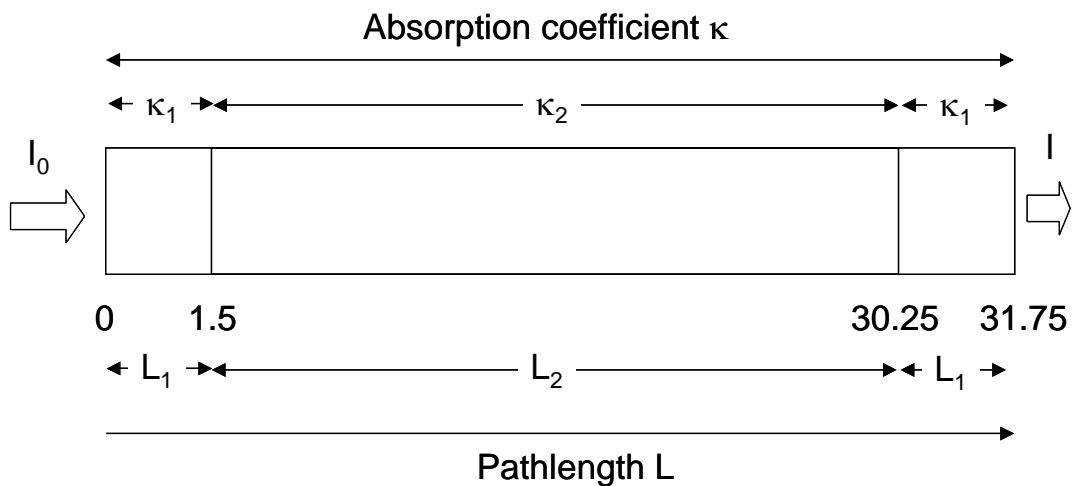
Figure 2-9: Absorption coefficient and pathlength used for uncertainty analysis of absorption coefficient due to window cooling.

Table 2-2: Temperature used for uncertainty analysis of absorption coefficient due to window cooling.

	Element 1	Element 2	Element 1
600 K		600 K	
	543 K	600 K	543 K
800 K		800 K	
	706 K	800 K	706 K
1000 K		1000 K	
	871 K	1000 K	871 K

Figure 2-10 shows the error between absorption coefficients for uniform temperature and for a temperature gradient due to window cooling. Carbon dioxide has a characteristic peak at about 2350 cm^{-1}. The error shows about + 2 % error is at the band center for all temperature, and − 3.5 % to − 6 % error at the band wings for 600 K and 1000 K, respectively. Therefore, the uncertainty of absorption coefficient due to the window cooling can be expected within ± 4 %, ± 5 %, and ± 6 % for 600 K, 800 K, and 1000 K, respectively. As the pathlength of uniform temperature increases, the error of absorption coefficient decreases. In other word, a short pathlength results in a huge uncertainty on absorption coefficient.
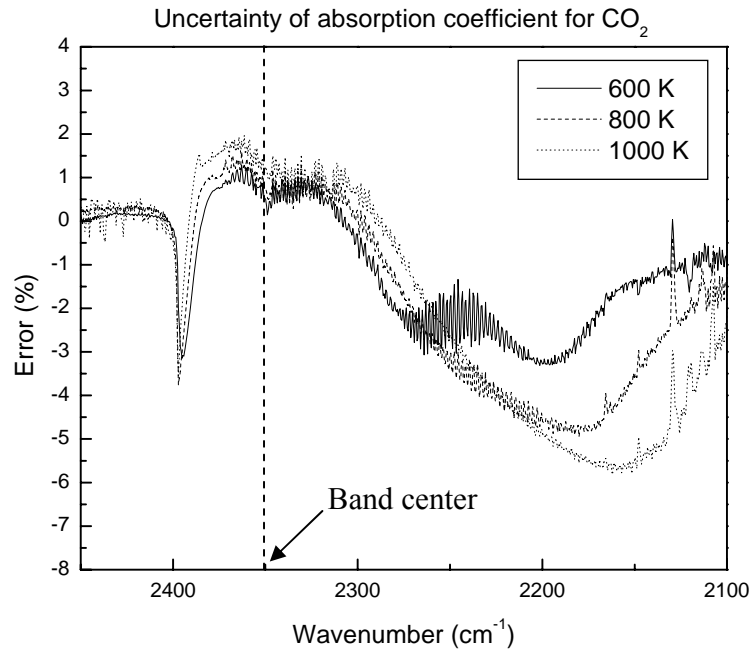
Figure 2-10: Uncertainty of absorption coefficient for CO_2 due to window cooling at 600 K, 800 K, and 1000 K.

2.5   Sample preparation

2.5.1   Gas fuels

CP grade (99.0 %) propane (Matheson gas), CP grade (99.0 %) propylene (Matheson gas), and acetylene infrared spectra at temperature ranging from 300 K to 1000 K were taken (300 K, 400 K, 450 K, 500 K, 600 K, 800 K and 1000 K). Mixtures containing 1000 ± 20 ppm, 2500 ± 50 ppm, and 4000 ± 80 ppm of propane in N_2 (99.999% Super Dry), and 15000 ± 300 ppm, 10000 ± 200 ppm, and 5000 ± 100 ppm of propylene in N_2 (99.999% Super Dry) were made by regulating the flow of these gases into the cell using mass flow controllers (MKS 1479A, 20 sccm for propane, 200 sccm for propylene and 1000 sccm for N_2). In order to calibrate the volume flow rate for each fuel, a NIST certified volume flow calibrator (Dry Cal DC-Lite, BIOS international Co.)

was used. The mass flow controllers were operated by a data acquisition system (Strawberry Tree Inc., currently supported by IO Tech Inc.), which continuously monitored the concentration, temperature within a gas cell, and pressure of gas line. The diluted gas was introduced into the gas cell, and then out to the exhaust.

2.5.2   Liquid fuels

Vaporized heptane (99.0 % Mallinckrodt), methanol (99.98 % J.T. Baker), toluene (99.999 % J.T. Baker), and methyl methacrylate (MMA, 99.9 %, Aldrich) infrared spectra were taken over temperatures ranging from 300 K to 1000 K as well as the gas fuel measurement. Since vaporized liquid fuels have to be supplied continuously, a fuel bubbling unit was set up within a lab hood. Figure 2-11 shows a picture and diagram of the fuel bubbler. Two K-type thermocouples (one for water bath, and the other for the fuel bubbler) were installed. Temperature data measured by a thermocouple in the fuel bubbler was used to calculate vapor pressure of fuel. The vapor pressure of each fuel was calculated using the Antoine equation with three parameters obtained by NIST web book (http://webbook.nist.gov). Fuel vapor pressure is expressed by Antoine equation as:

$$P_{fuel}(Bar) = 1.0E\left(A - \frac{B}{T_{fuel} + C} \right) \qquad (2.1)$$

where, T_{fuel}, A, B, and C are liquid fuel temperature (K), and Antoine parameters for each fuels shown in Table 2-3, respectively.

Nitrogen was introduced into the bubbler and mixed with additional nitrogen at the mixing point for dilution, then delivered to the gas cell. Three concentrations shown in Table 2-4 were adjusted not to exceed the saturation of transmittance (0% transmittance) infrared spectrum. Therefore, the first attempt for each fuel infrared measurement was to set the concentration of each fuel at ambient temperature. The gas phase infrared spectrum data on NIST webbook [58] was used to estimate the maximum concentration not to saturate the spectral transmissivity 0, and minor adjustment was made with the smaller fuel flow mass flow controller. At least three samples and maximum 5 samples were taken for each concentration of fuel and nitrogen mixture to verify that the spectrum was stable at each temperature. Infrared measurements were conducted from highest concentration to lowest one. The repeatability of the spectrum using low to high concentration and also high to low concentration was checked and both orders gave the same result.
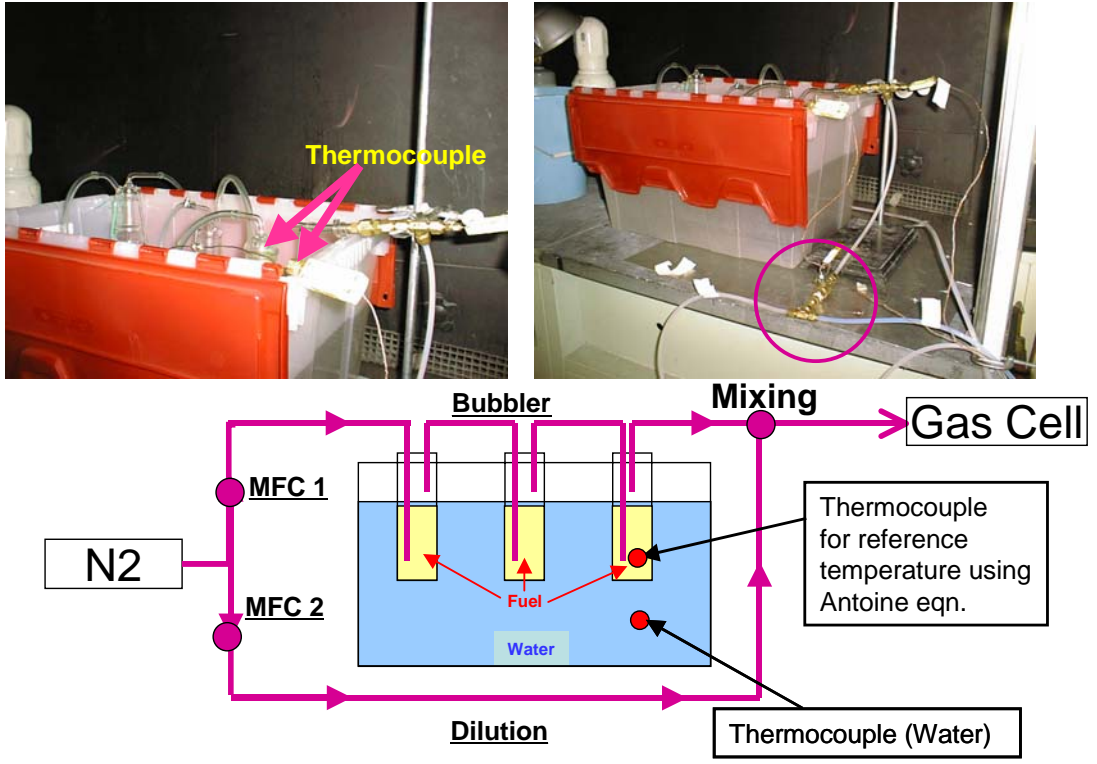
Figure 2-11: Picture and diagram of a fuel bubbling device.

Table 2-3: Antoine equation parameters for heptane, methanol, toluene, and methyl methacrylate.

Fuel	Temperature (K)	A	B	C
Heptane (C_7H_{16})	299.1-372.43	4.02832	1268.636	-56.20
Methanol (CH_3OH)	288.0-256.83	5.20409	1581.341	-33.50
Toluene (C_7H_8)	273.13-297.89	4.23679	1426.448	-45.957
Methyl methacrylate ($C_5H_8O_2$)	312.3-362.3	5.37785	1945.560	-7.569

Table 2-4: List of experimental condition for gas and liquid fuels.

Gas fuels

Propane

Temperature (K)	Volume Fraction (x 10^{-6})		
295	1000	2500	4000
396	1000	2500	4000
435	1000	2500	4000
513	1000	2500	4000
578	1000	2500	4000
790	1000	2500	4000
1009	1000	2500	4000

Propylene

Temperature (K)	Volume Fraction (x 10^{-6})		
296	5000	10000	15000
390	5000	10000	15000
444	5000	10000	15000
491	5000	10000	15000
594	5000	10000	15000
793	5000	10000	15000
1003	5000	10000	15000

Liquid fuels

Heptane

Temperature (K)	Volume Fraction (x 10^{-6})		
293	474	985	1554
400	458	951	1500
450	480	982	1564
490	474	964	1561
593	479	992	1588
794	468	952	1389
1000	548	971	1149

Methanol

Temperature (K)	Volume Fraction (x 10^{-6})		
293	1570	2256	2912
396	1590	2323	2935
443	1445	2235	2960
483	1540	2213	2857
570	1574	2286	2904
804	1692	2472	3193
1000	1543	2302	3055

Toluene

Temperature (K)	Volume Fraction (x 10^{-6})		
300	4278	3183	2548
396	3929	3021	2552
440	3446	2666	2340
477	3964	3032	2617
587	3729	3026	2557
795	4021	3043	2627
999	4345	3260	2821

MMA

Temperature (K)	Volume Fraction (x 10^{-6})		
297	3162	2474	1716
396	3217	2413	1670
441	2978	2330	1600
483	3011	2337	1613
597	3044	2350	1626
803	3324	2551	1746
1014	3596	2767	1883

2.6   Conclusion

An experimental apparatus for high temperature FTIR measurement was developed. Thermal properties and spectral characteristics of infrared windows were evaluated and ZnSe were chosen as the infrared window. A window cooling unit was designed and installed in a gas cell to protect the ZnSe windows from oxidation and thermal degradation and keep its spectral transmissivity at high temperature. Cooling effect on the infrared window was evaluated by temperature measurement inside and outside of the windows by thermocouples, and the necessary cooling velocity on the window was determined. Two mass flow controllers, one for fuel delivery and the other for fuel dilution, were installed to supply gas fuels and nitrogen mixture continuously to optical cell. In order to investigate an infrared spectrum at gas phase of liquid fuels, a water bath was used to vaporize liquid fuels by nitrogen bubbling. A thermocouple in the liquid fuel determined the vapor pressure of liquid fuel using the Antoine equation. All concentrations of fuel and nitrogen mixture were determined by the ratio of fuel volume flow rate to total volume flow rate.

CHAPTER 3   ABSORPTION DATA ANALYSIS

3.1   Introduction

In the previous chapter, the unique high temperature infrared spectrometer and measurement technique for gas and liquid fuels were introduced. In this chapter, infrared spectrum of various fuels is first presented for characteristic band groups for each fuel. Next, a simplified extrapolation technique of infrared absorption coefficient at high temperature from several lower temperatures is introduced. This technique is very useful to take an infrared measurement at high temperature (> 700 K), which cannot usually be measured by infrared spectrometers, and also for fuels, that are thermally unstable at high temperature. Last, verification of the extrapolation technique using HITEMP database and infrared spectra of propane and fuel pyrolysis problem at high temperature are presented.

3.2   Gas fuels

3.2.1   Propane (C_3H_8)

Figure 3-1 shows the absorption coefficient of propane at 296 K, which illustrates a typical absorption spectrum for a paraffin hydrocarbon.   The temperature dependent normalized blackbody spectral emissive power is also plotted as a function of wavenumber to show how characteristic bands of such fuels impacts absorption of blackbody radiation for a range of temperatures. Propane contains a CH_3- stretching peak

centered at 2960 cm^{-1} and bending peaks at 1460 and 1380 cm^{-1} as well as $-CH_2-$ stretching peaks at 2930 and 2850 cm^{-1}, and a bending peak at 1470 cm^{-1}. Figure 3-2 (a) and (b) show the spectral absorption coefficient of the propane stretching and bending band regions as a function of T. The plots show the characteristic decline with increasing T in absorption coefficients near the band centers and the broadening causing a rise in spectral absorption with increasing T near the edges of the band.

The location of the peak blackbody emission shifts to larger wavenumber (shorter wavelength) as T increases as indicated in Figure 3-1. The low wave number absorption bending bands thus have a larger impact on emission and absorption of blackbody radiation at low $T \leq 400$ K. On the other hand for high temperature ($T \geq 800$ K), the higher frequency C-H stretching peaks fall nearer to the peaks of blackbody emission and thus play the dominant role in fuel-based radiative absorption. In addition to a decrease of absorption coefficient and an increase the height of band wing, the spectrum at high temperature looks noisy. Taine and Soufiani [59] provide a good explanation of infrared spectrum at high temperature. As temperature increases, the probability of energy transition between higher energy levels of both vibration and rotation increase. Finally, a spectrum at the higher energy level tends to appear clearly. Since a spectrum shows the sum of all possible energy transition in a molecule, a spectrum at high temperature presents many noisy tiny waves.

Figure 3-1: The measured spectral absorption coefficient of propane (C_3H_8) at 296 K and the temperature dependent normalized blackbody spectral emissive power as a function of wavenumber.

(a)
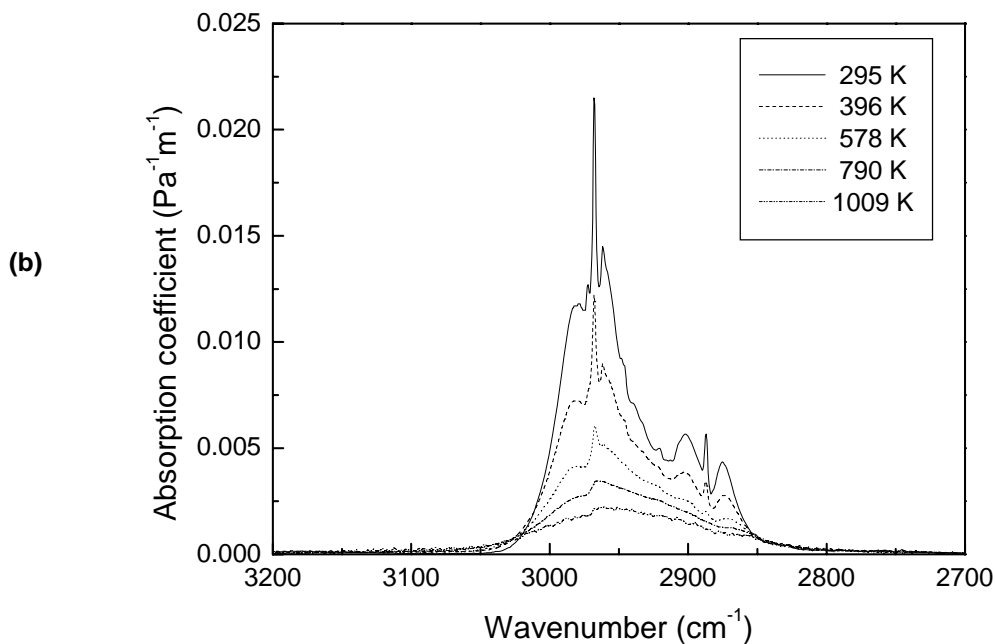
Figure 3-2: Measured temperature-dependent spectral absorption coefficient of C_3H_8; (a) C-H bending and (b) C-H stretching region.

3.2.2   Propylene (C_3H_6)

Figure 3-3 shows the absorption coefficient of propylene at 296 K and the temperature dependent normalized blackbody spectral emissive power as a function of wavenumber. Propylene has a large set of characteristic band groups such as a bending group (1420 cm^{-1}), stretching of =CH_2 (3080 cm^{-1}), C-H out of plane bending (1860 cm^{-1}), C=C stretching (1645 cm^{-1}), and =CH_2 out of plane bending (990 cm^{-1} and 910 cm^{-1}), in addition to a C-H stretching group (2960 cm^{-1} for CH_3-). Propylene's =CH_2 out of plane bending enhances radiation absorption and emission at lower temperatures. Figure 3-4 (a), (b), and (c) show the spectral absorption coefficient of propylene =CH_2 and C-H out of plane bending peaks, and C=C stretching, and C-H in and out of plane bending and =CH_2 stretching peaks as a function of temperature.

Figure 3-3: The measured spectral absorption coefficient of C_3H_6 at 296 K and the temperature-dependent normalized blackbody spectral emissive power as a function of wavenumber.

Figure 3-4: The measured temperature dependent spectral absorption coefficient of Propylene (C_3H_6); (a) =CH_2 out of plane bending (b) C-H in plane and out of plane bending, and C=C stretching and (c) CH_3- and =CH_2 stretching.

3.3 Liquid Fuels

3.3.1 Heptane (C_7H_{16})

Figure 3-5 shows the absorption coefficient of n-heptane at 296 K and the temperature dependent normalized blackbody spectral emissive power as a function of wavenumber. Since both propane and heptane are alkanes and have the same characteristic band groups (CH_3- and -CH_2-), heptane qualitatively has the same absorption characteristic as propane. Figure 3-6 (a) and (b) show the spectral absorption coefficient of the C-H bending and stretching peaks for heptane as a function of temperature. As expected, comparison of Figures 3-3 and 3-5 shows that heptane absorbs more radiant energy per unit mole than propane due to the increased number of C-H bonds. Furthermore, heptane, with its increased chain length, has a reduced sharpness in the peaks in comparison to propane.

Figure 3-5: Measured spectral absorption coefficient of n-C_7H_{16} at 293 K and the temperature dependent normalized blackbody spectral emissive power as a function of wavenumber.

Figure 3-6: The measured spectral absorption coefficient of n-heptane; (a) C-H bending and (b) C-H stretching.

3.3.2   Toluene (C_7H_8)

Figure 3-7 shows the absorption coefficient of toluene at 296 K and the temperature dependent normalized blackbody spectral emissive power as a function of wavenumber. This figure shows how characteristic bands of toluene impact absorption of blackbody emission. Toluene contains CH_3- stretching peaks centered at 2940 and 2889 cm^{-1}, bending peaks at 1473 and 1392 cm^{-1}, =CH stretching peaks at 3073 and 3046 cm^{-1}, in-plane bending peaks at 1090 and 1030 cm^{-1}, and a strong out of plane bending peak at 728 cm^{-1}, phenyl C=C stretching peaks at 1609 and 1500 cm^{-1}, respectively. Figure 3-8 (a)-(e) show the spectral absorption coefficient of the toluene =CH out of plane bending, in plane bending, CH_3 bending and phenyl C=C stretching, and CH_3 and =CH stretching band region as a function of temperature, respectively. A phenyl =CH bending motion and C=C stretching have the most significant impact on emission and absorption for blackbody radiation from low to high temperature. Stretching motion of CH_3- for toluene at low temperature does not contribute blackbody radiation so much compared to other peaks, but the motion becomes important at temperature higher than 800 K. Since the fuel rich core temperature generally ranges from the boiling temperature to 900 K, out of plane and in plane =CH bending and C=C stretching peaks of toluene molecule causes blackbody emission and absorption mainly within the fuel rich core and C-H stretching motion does near the flame.
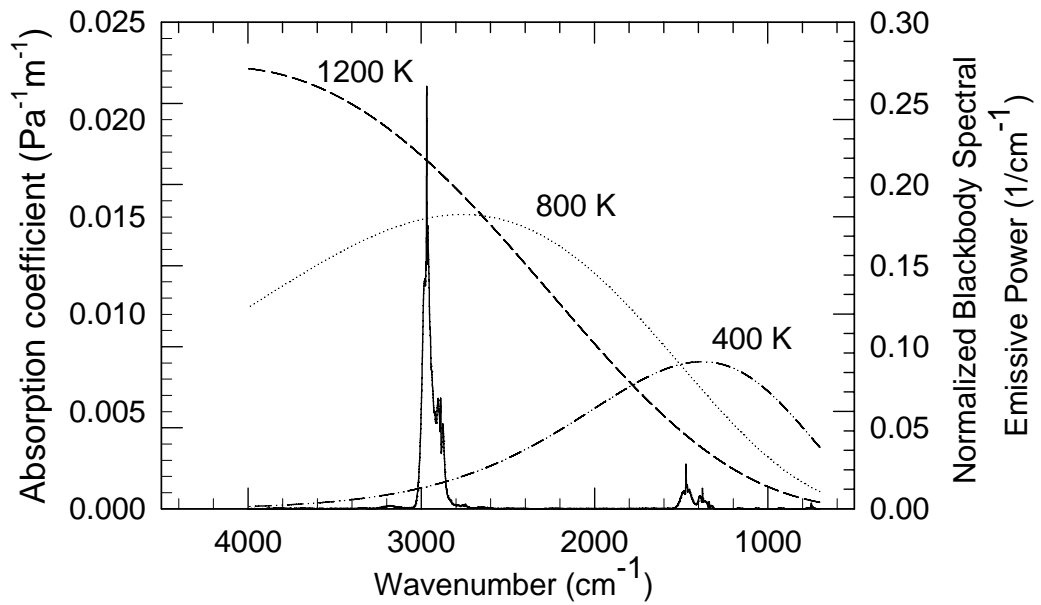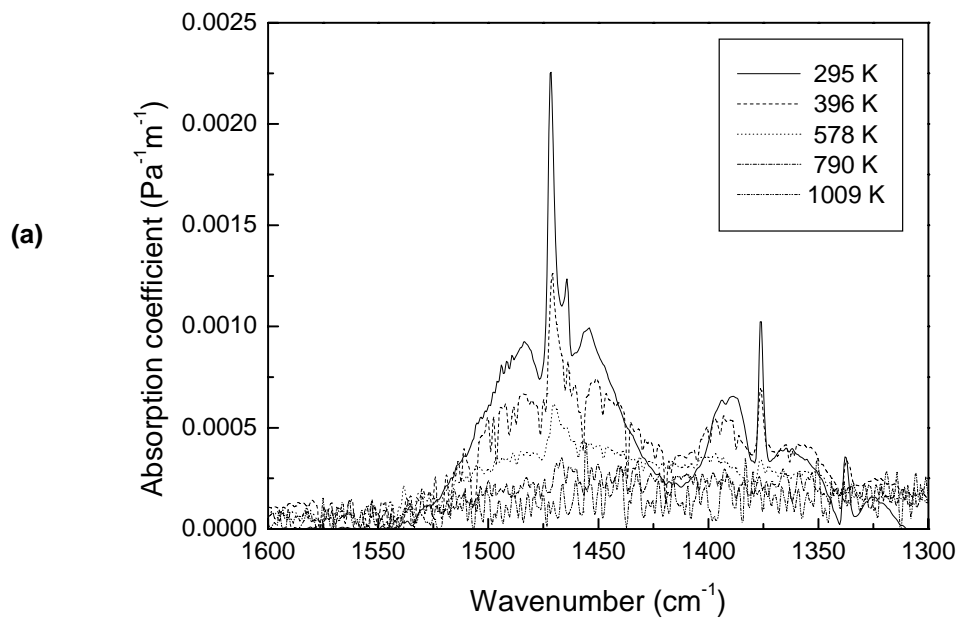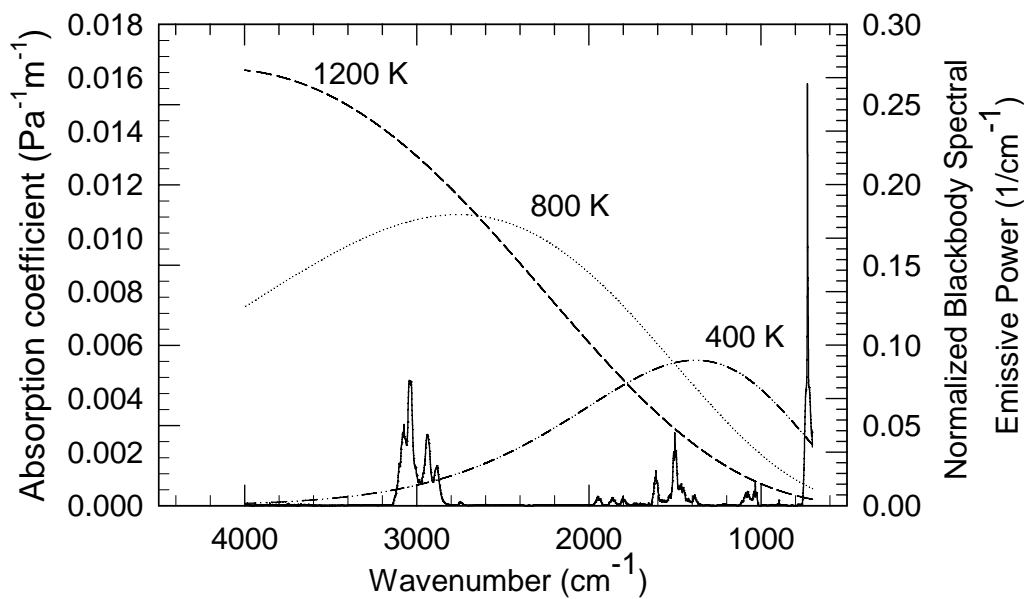
Figure 3-7: Measured spectral absorption coefficient of toluene (C_7H_8) at 300 K and the temperature dependent normalized blackbody spectral emissive power as a function of wavenumber.

(a)

(b)

(c)

59
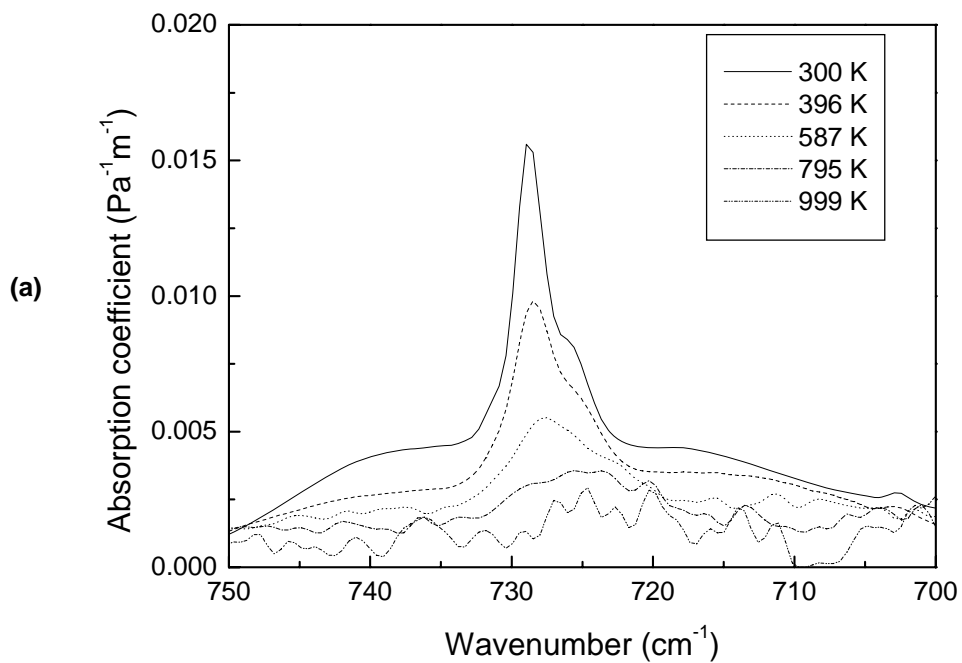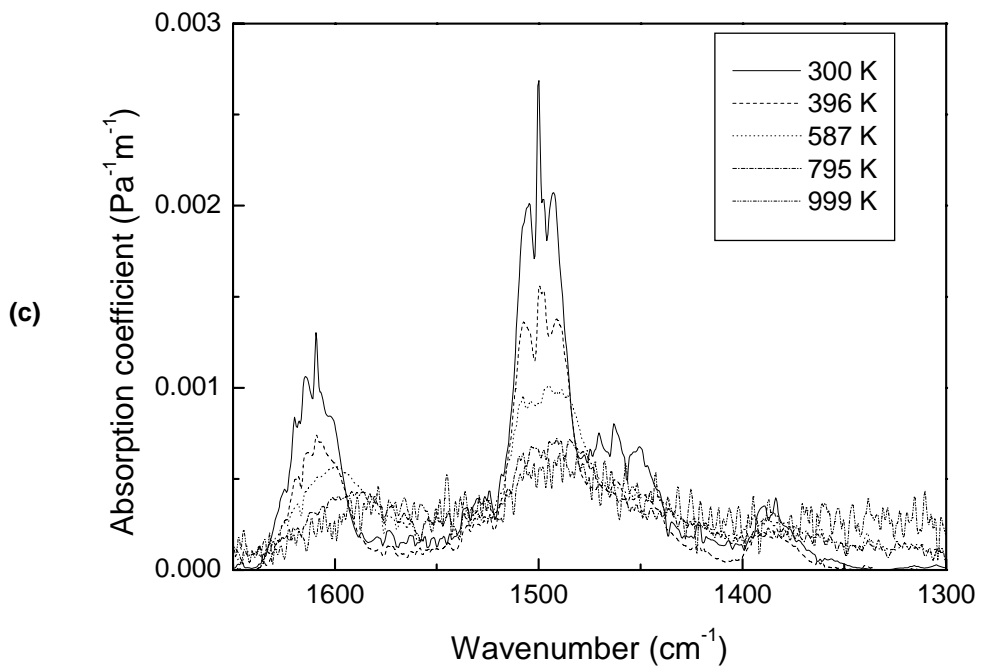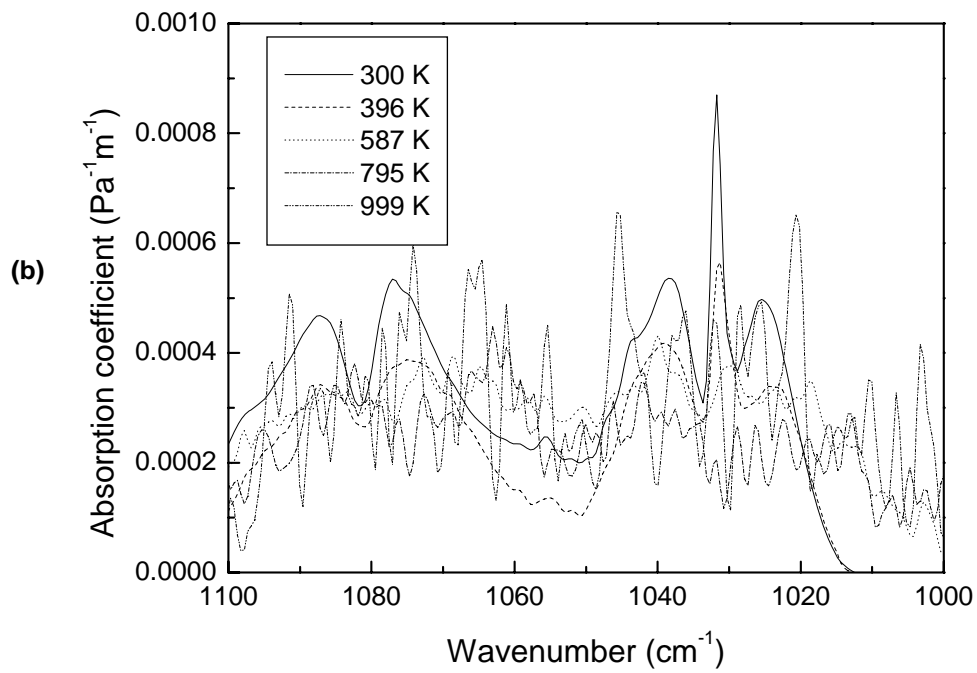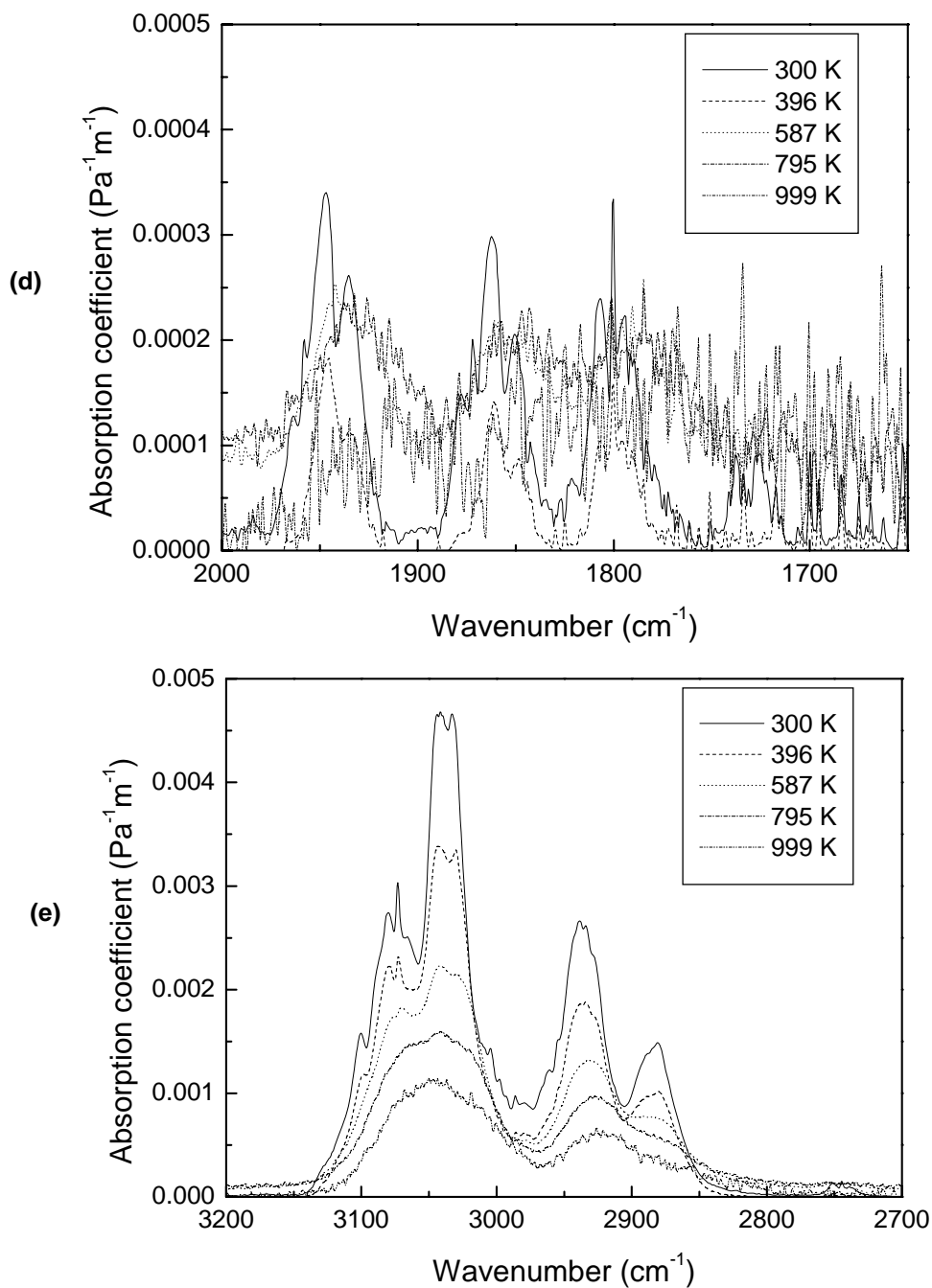
Figure 3-8: The temperature dependent spectral Planck mean absorption coefficient of toluene (C_7H_8); (a) phenyl =CH out of plane bending (b) phenyl =CH in plane bending, (c) phenyl C=C stretching, (d) overtones of (b) and (e) CH_3- and =CH stretching.

3.3.3   Methanol (CH$_3$OH)

Figure 3-9 shows the absorption coefficient of methanol at 296 K and the temperature dependent normalized blackbody spectral emissive power as a function of wavenumber. This figure represents how characteristic bands of methanol impact absorption of blackbody emission. Methanol contains CH$_3$- stretching peaks centered at 2981 and 2844 cm^{-1}, bending peaks at 1455 and 1345 cm^{-1}, an -OH stretching peak at 3680 cm^{-1}, a strong C-O stretching peak at 1033 cm^{-1}, and a bending peak at 1470 cm^{-1}. Figure 3-10 (a)-(d) show the spectral absorption coefficient of the methanol C-O stretching, CH$_3$- bending, CH$_3$- stretching, and –OH stretching band region as a function of temperature, respectively. A C-O stretching motion has the most significant impact on emission and absorption for blackbody radiation from low to high temperature. Other motions such as CH$_3$- bending and –OH stretching are very small compared to C-O stretching, but CH$_3$- stretching motion becomes more important higher than 800 K. Although the fuel rich core region of a methanol fire is much thinner than heptane and toluene fire, the C-O stretching motion of methanol molecule for blackbody emission and absorption occurs near the fuel surface while the CH$_3$- stretching motion occurs near the flame.
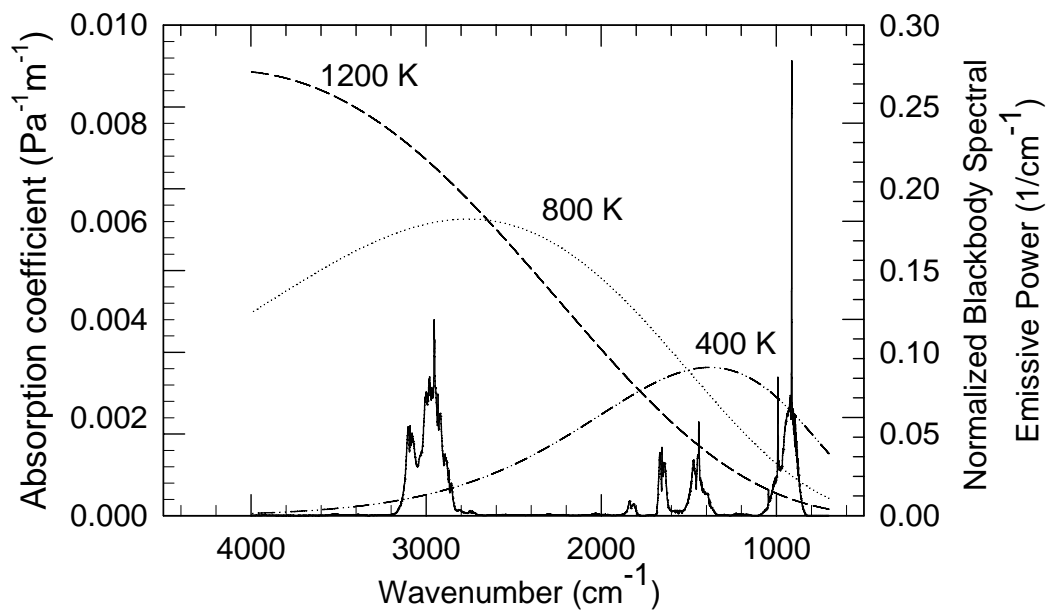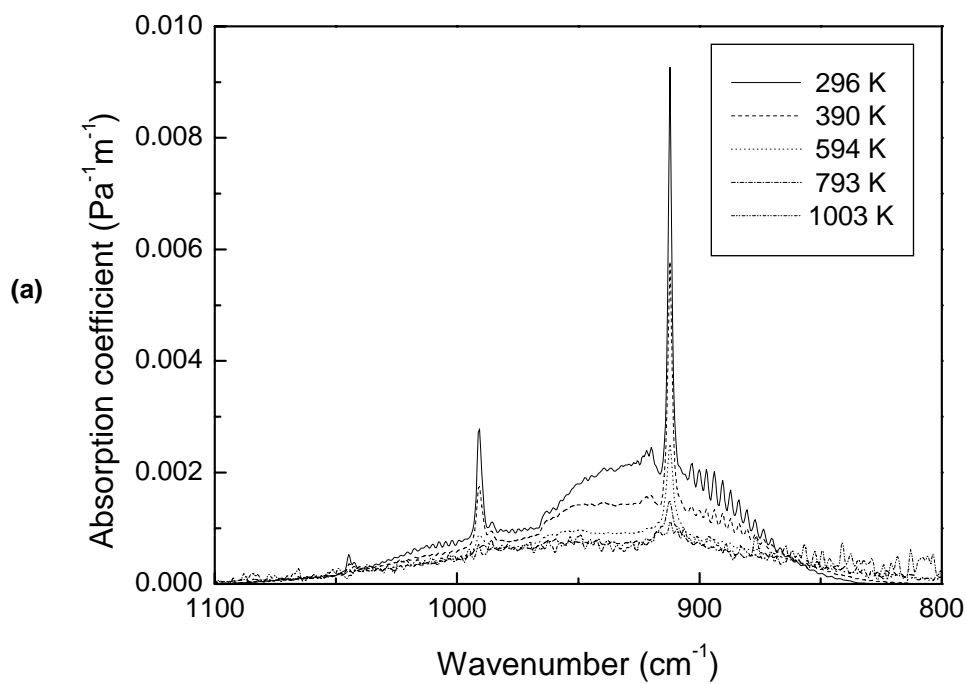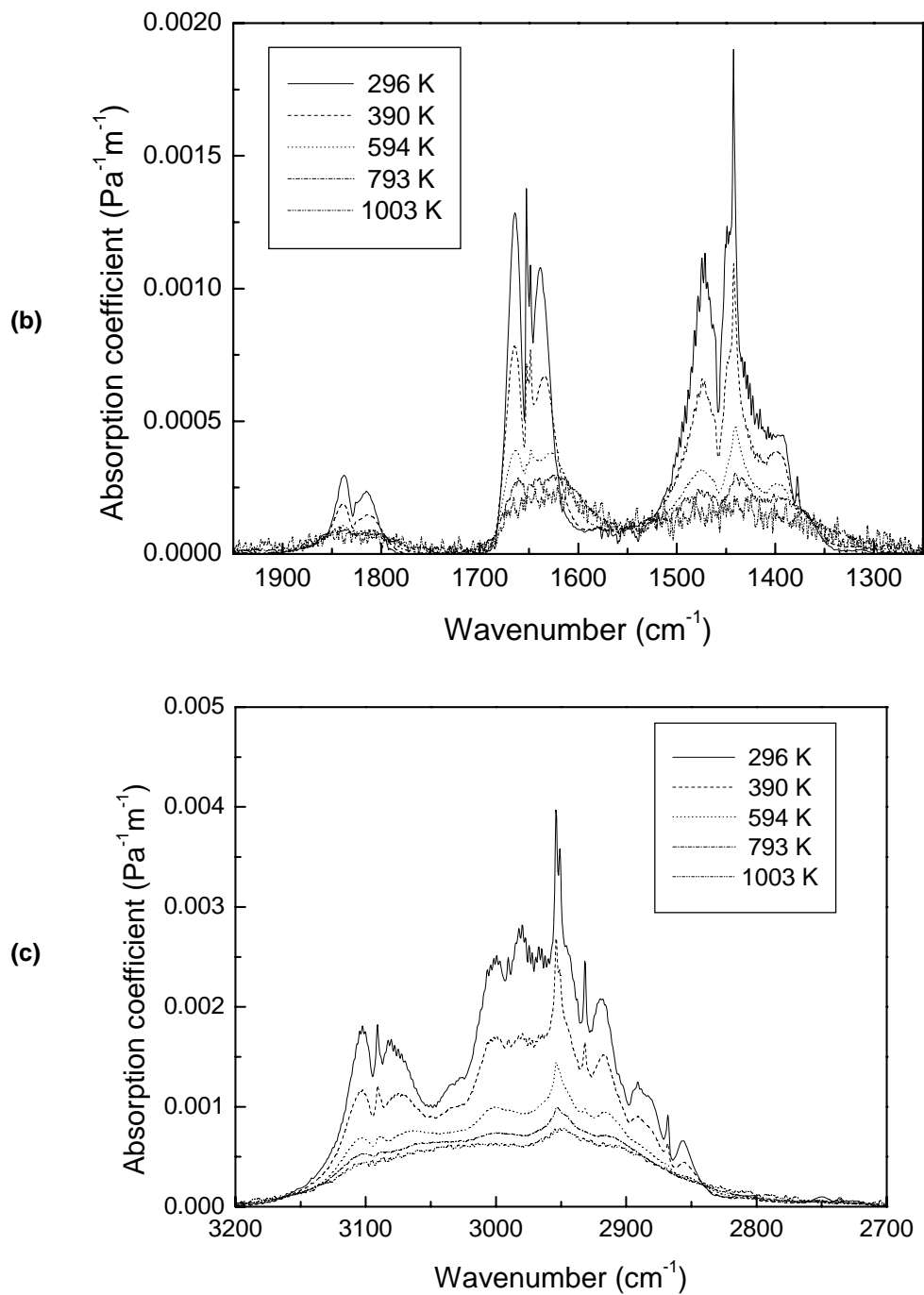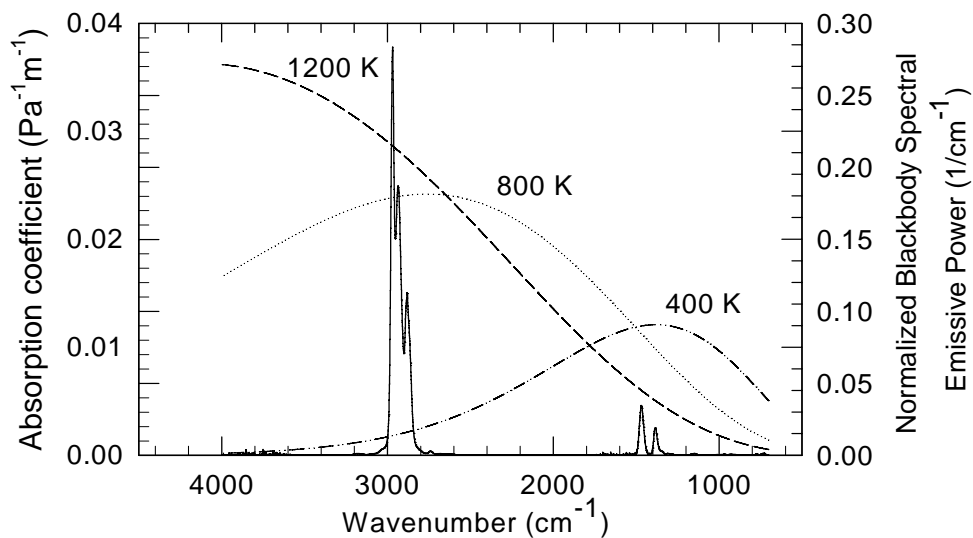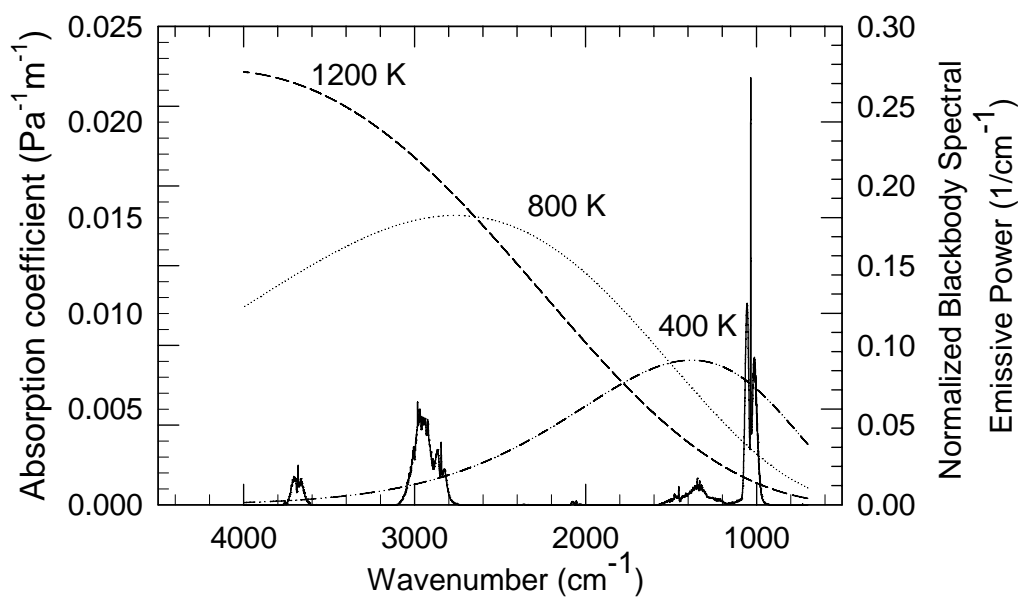
Figure 3-9: Measured spectral absorption coefficient of methanol (CH₃OH) at 293 K and the temperature dependent normalized blackbody spectral emissive power as a function of wavenumber.
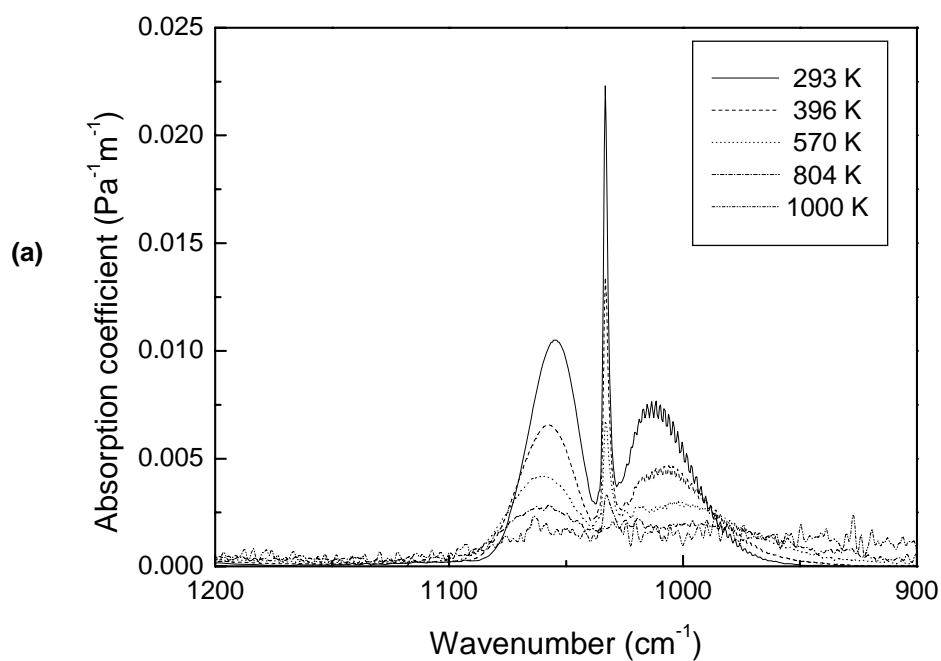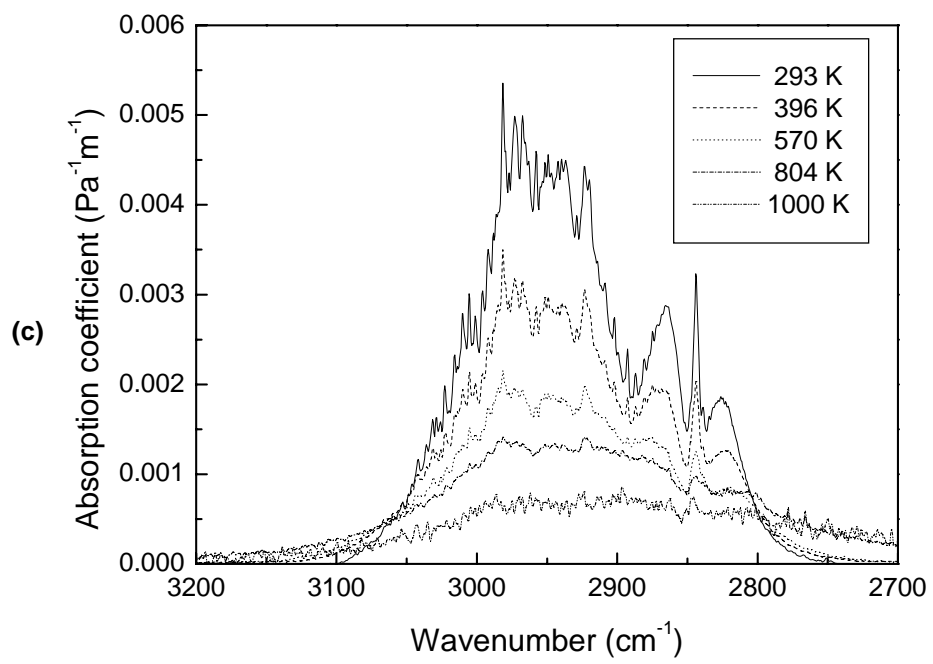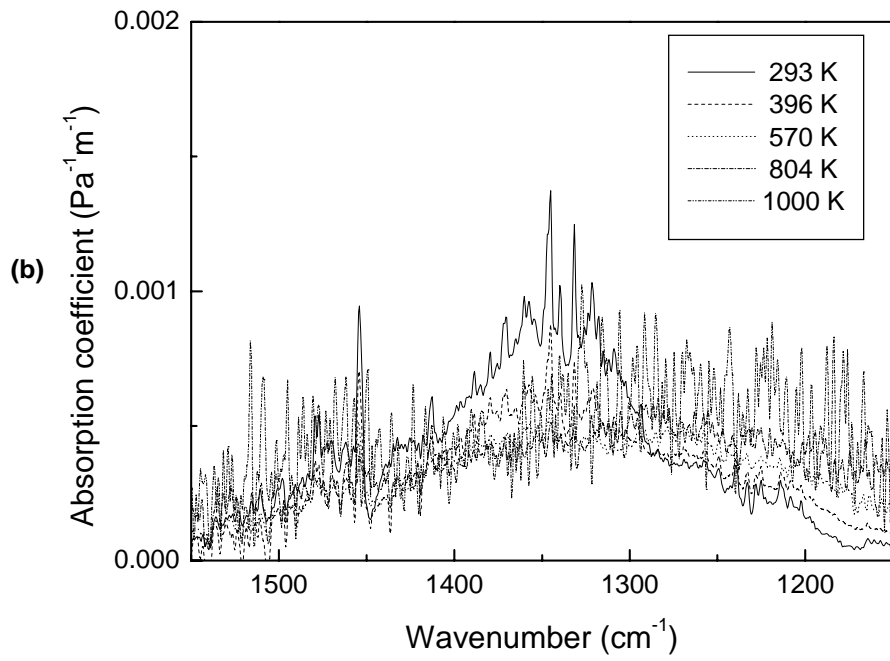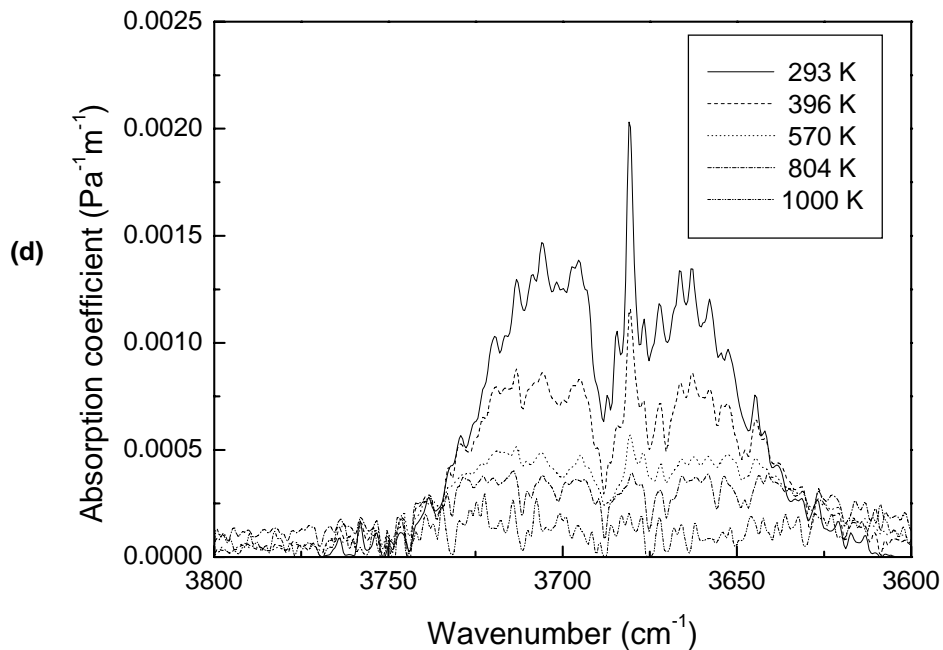
Figure 3-10: The temperature dependent spectral absorption coefficient of methanol (CH$_3$OH); (a) C-O stretching, (b) C-H bending, (c) C-H stretching, and (d) O-H stretching region.

3.3.4   Methyl Methacrylate (MMA, C$_5$H$_8$O$_2$)

Figure 3-11 shows the absorption coefficient of methyl methacrylate at 296 K and the temperature dependent normalized blackbody spectral emi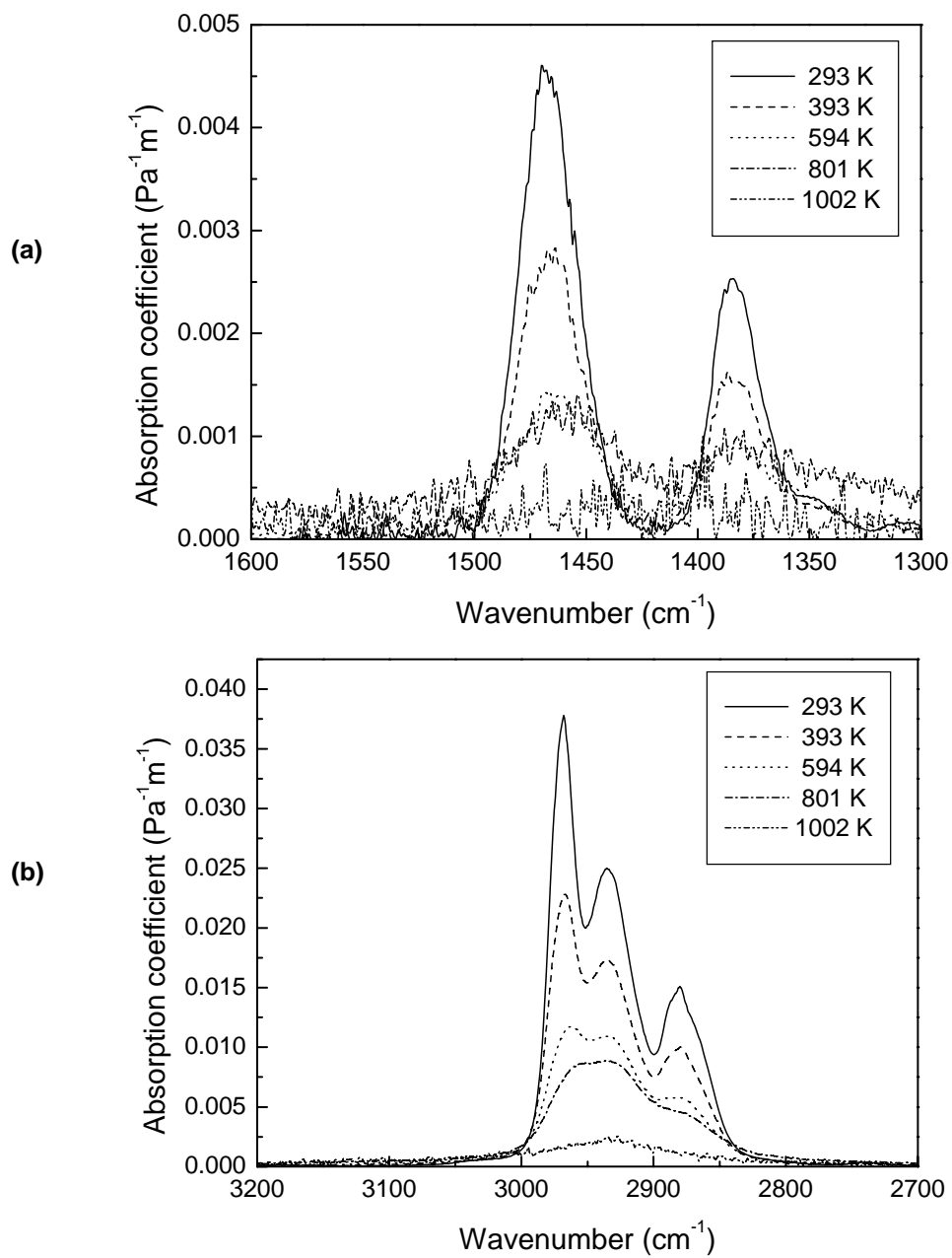ssive power as a function of wavenumber. This figure shows how characteristic bands of methyl methacrylate impact absorption of blackbody emission. Compared to methanol and toluene, methyl methacrylate has more bands. Methyl methacrylate contains CH$_3$- stretching peaks centered at 2970 and 2864 cm^{-1}, bending peaks at 1450 and 1332 cm^{-1}, =CH stretching peaks at 3114 and 3001 cm^{-1}, and out of plane bending peaks at 941 and 1030 cm^{-1}, a C=C stretching peak at 1651 cm^{-1}, a C=O stretching peak at 1748 cm^{-1}, and C-O stretching peaks at 1202 and 1170 cm^{-1}. Figure 3-12 (a)-(d) show the spectral absorption coefficient of the methyl methacrylate =CH$_2$ out of plane bending, C-O stretching and

CH$_3$- bending, C=C and C=O stretching, and CH$_3$- and =CH$_2$ stretching band region as a function of temperature, respectively. C-O and C=O stretching and CH$_3$- bending motions have the most significant impact on emission and absorption for blackbody radiation of methyl methacrylate from low to high temperature. Stretching motion of CH$_3$- for methyl methacrylate at low temperature does not contribute the blackbody radiation as much compared as other peaks, but the motion increases at temperature higher than 800 K. The C-O and C=O stretching motions play an even more important role for emission and absorption of blackbody radiation at 800 K. Since the fuel rich core temperature generally ranges from the boiling temperature to 900 K, C-O and C=O stretching and CH$_3$- bending motions of methyl methacrylate molecule occupy regions of high blackbody emission and absorption mainly within the fuel rich core, and C-O, C=O, CH$_3$- and =CH$_2$ stretching motions does near the flame.
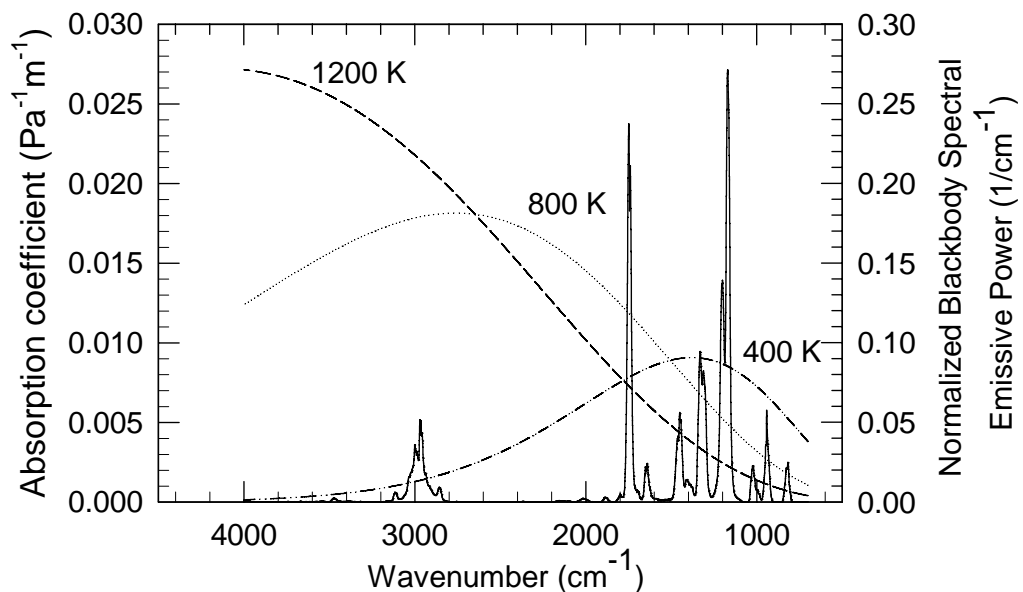
Figure 3-11: Measured spectral absorption coefficient of Methyl-methacrylate (MMA, C$_5$H$_8$O$_2$) at 297 K and the temperature dependent normalized blackbody spectral emissive power as a function of wavenumber.

66
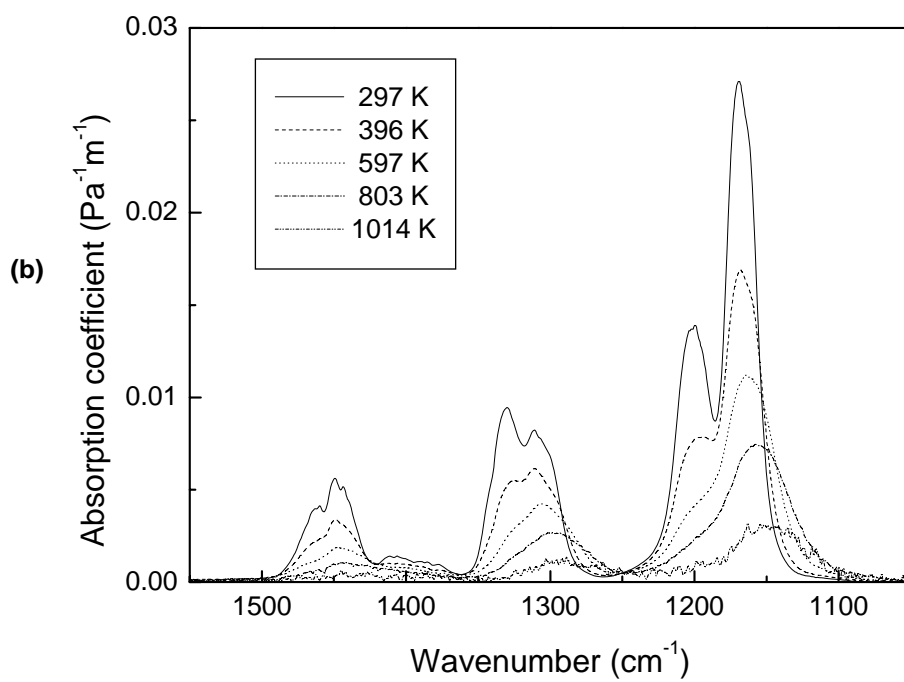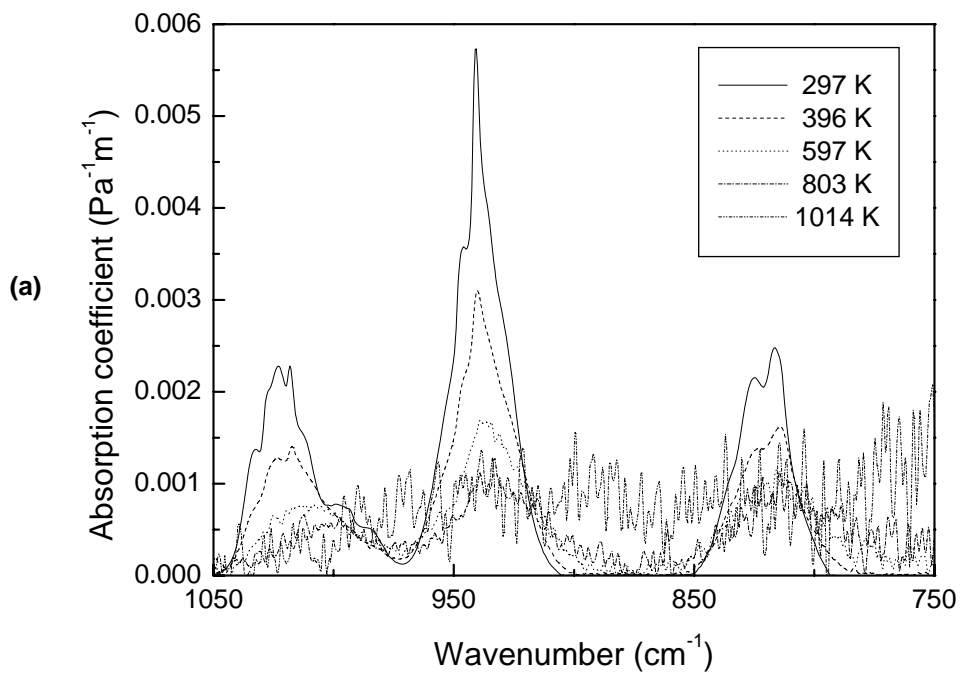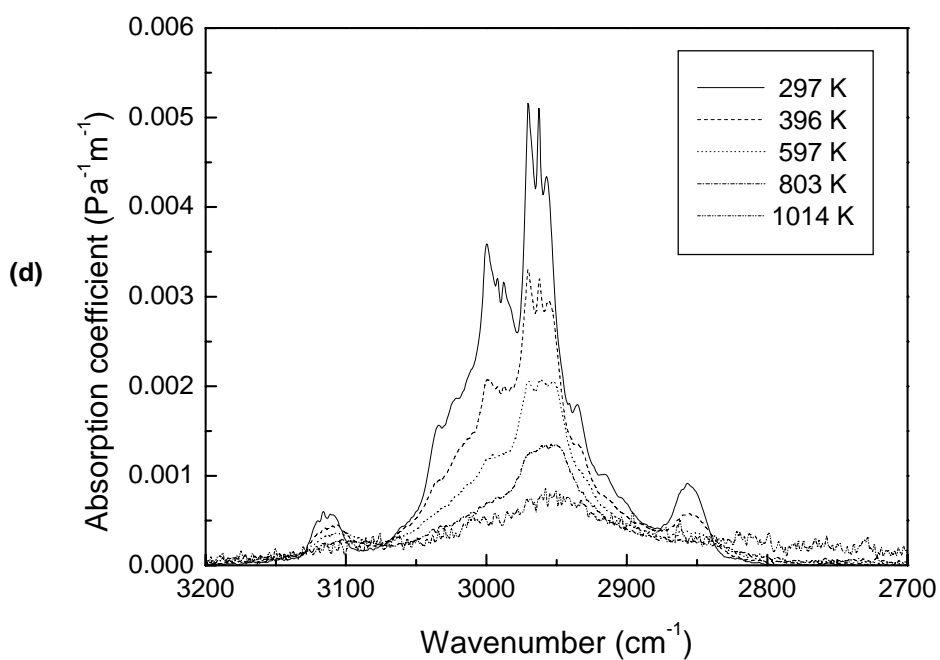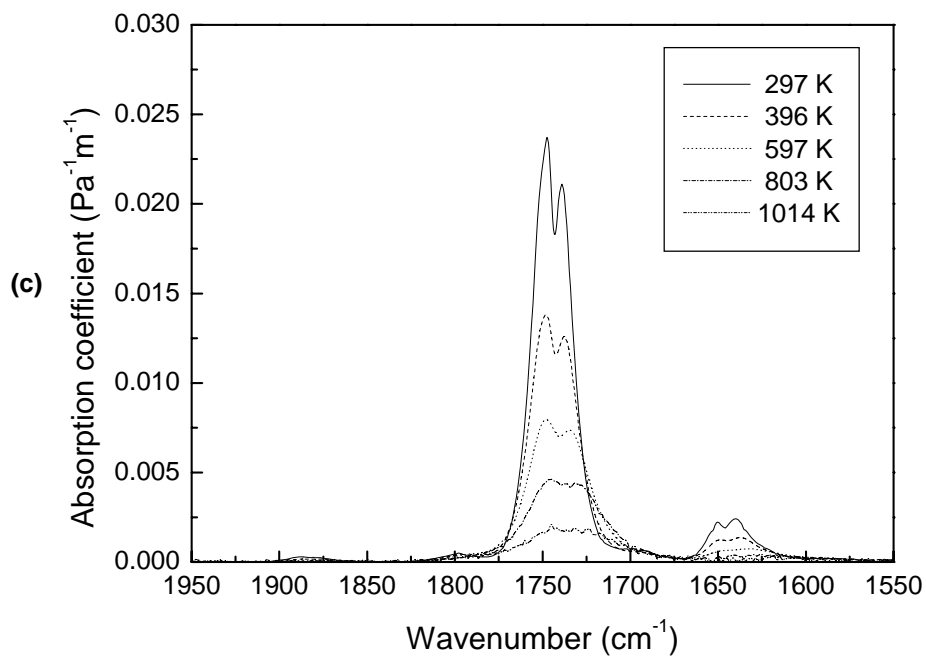
Figure 3-12: The temperature dependent spectral absorption coefficient of methyl methacrylate ($C_5H_8O_2$); (a) $=CH_2$ out of plane bending (b) C-O stretching and CH_3-bending (c) C=C and C=O stretching, and (d) CH_3- and $=CH_2$ stretching.

3.4   Extrapolation technique

3.4.1   Concept and background

Absorption measurements at temperatures above 700 K are difficult to make due to the thermal properties of infrared transmitting materials. Materials that transmit well in the infrared are generally not sufficiently robust to characteristic bands of methanol impact absorption of blackbody emission. One way to circumvent these limitations is to extrapolate the data collected at lower temperatures. This extrapolation technique was developed by Fuss and Nyden, and Wakatsuki [60]. The focus of this investigation, therefore, was to develop a semi-quantitative method to extrapolate absorption coefficient data, obtained for temperatures up to about 700 K, to the higher temperatures (approaching 1000 K) that are required to describe the transfer of radiation between the flame zone and fuel-rich core in fires.

The approach taken in this study was to simplify a quantum mechanical expression of general absorption coefficient described in eqn. 1.30 at chapter 1 to a form suitable for fitting the absorption coefficients measured over a range of temperatures. This was achieved by reducing eqn. 1.30 to an expression containing three fit parameters (S_0, E', and n) and two variables (ν and T). The values of the absorption coefficients at higher temperatures, which are difficult to measure, can then be estimated by extrapolation.

Recall, absorption coefficient is expressed as

$$k_\nu = \cfrac{\left\{\dfrac{8\cdot\pi^3}{3hc}\right\}\cdot\nu\cdot\left\{\dfrac{|R|^2}{g_l}\right\}\cdot g_i\cdot I_a\cdot\left[1-\exp\left(-\dfrac{hc\nu}{kT}\right)\right]\cdot g_l\cdot\exp\left(-\dfrac{E'}{kT}\right)\cdot\dfrac{g}{\pi}\cdot\left(\dfrac{296}{T}\right)^n\cdot P_t\cdot N_L\cdot\left(\dfrac{296}{T}\right)}{Q\cdot10^{36}\cdot\left[(\nu-\nu_0)^2+\left(g\cdot\left(\dfrac{296}{T}\right)^n\cdot P_t\right)^2\right]} \qquad (1.30)$$

The terms with negligible temperature or frequency dependence were consolidated into S_0 as indicated in eqn. (3.3).

$$S_0 = \cfrac{\left\{\dfrac{8\pi^2}{3hc}\right\}\cdot\left\{\dfrac{|R|^2}{g_l}\right\}\cdot g_i\cdot I_a\cdot g_l\cdot N_L}{296^{n-1}\cdot10^{36}\cdot g\cdot P_t\left(\dfrac{Q}{T^{\frac{m}{2}}}\right)} \qquad (3.3)$$

In the denominator, it includes all but T^m and the temperature dependence of the partition sum Q. The rotational partition function is presumed to be proportional to T (m = 2 rotational degrees of freedom) in a linear molecule and $T^{3/2}$ (m = 3) in a nonlinear molecule. With this in mind, all powers of T that were not contained in the exponential terms were included in the temperature exponent, n. Including the temperature dependency on the number of absorbing molecule and rotational partition function, the constraint of power n was set from 0 to 2. As a first approximation, the explicit contributions from overlapping rotational lines are ignored by setting $\nu = \nu_0$ so that the effects of the Lorentzian line shape functions are effectively subsumed into the S_0 and T^n terms. Since the temperature dependence of each rotational transition is unique, this approximation is likely to result in larger errors when the resolution of the measurements

is not sufficient to differentiate between the individual lines. After substituting $E' = hcv_r$ = 1.439 v_r for the energy of the lower state, eqn. (1.30) becomes:

$$k_v = \frac{S_0 \cdot v \cdot \left[1 - \exp\left(-\frac{1.439 \cdot v}{T}\right)\right] \cdot \exp\left(-\frac{1.439 \cdot v_r}{T}\right)}{T^n}$$

(3.4)

In this expression temperature, T (K), and wavenumber, v (cm^{-1}), are independent variables and the parameters S_0, v_r, and n were fit over a range of temperatures at each wavenumber.

Equation 3.4 ignores minor temperature dependencies of some terms in the full quantum expression by lumping them into a constant S_0, but provides a reasonable approximation to the full equation with respect to temperature. The three parameters S_0, v_r, and n are optimized using a least squares approach to fit measured spectral absorption data such that κ_v can be extrapolated and interpolated for any range of temperatures. The fits do very well at capturing the falloff with temperature of the various absorption bands, but have limited accuracy for the wings of strong bands where slight increases in κ_v with temperature can arise due to line broadening at high temperatures. However, the wings typically account for very small amounts of the total integrated κ_p and thus the fitted equations provide sufficiently accurate values for κ_v's to use, and for finding κ_p as a function of T.

3.4.2 Verification

3.4.2.1 HITEMP database

Absorption data for CO, CO_2, and H_2O were obtained for temperatures up to 1000 K from the HITEMP database [6]. HITEMP is the high temperature extension of the HITRAN database, which is compilation of molecular line absorption data for 39 species [18]. The accuracy of the spectra derived from the HITEMP database for applications to combusting systems at temperatures exceeding 1000 K has already been examined by others [61]. The parameters (S_o, v_r, n) were fit to eqn. 3.3 for absorption coefficients obtained from the database at 300 K, 400 K, 450 K, 500 K, and 600 K. Using these parameters, an extrapolation was performed to 1000 K and comparisons were made to absorption coefficients calculated from spectra generated directly from the HITEMP database at 1000 K. As a first attempt, the accuracy of the extrapolation procedure was examined without introducing complications due to experimental errors. This exercise provides an estimate of the magnitude of the errors resulting from the simplifications introduced in representing eqn. 1.30 by eqn. 3.4.

The accuracies of the extrapolations are assessed according to eqn. 3.6. The relative errors are determined by taking the ratio of the difference between the integrated absorption coefficients obtained from the extrapolations and the "actual" values obtained (either from HITEMP for CO, H_2O, and CO_2 or experimental spectra for C_3H_8) and dividing by the "actual" values.

$$Error(\%) = \frac{\int_{\Delta v} \kappa_{v_{(Fit)}} dv - \int_{\Delta v} \kappa_{v_{(HITEMP \ or \ Experiment)}} dv}{\int_{\Delta v} \kappa_{v_{(HITEMP \ or \ Experiment)}} dv} \times 100 \qquad (3.6)$$

3.4.2.2   Carbon Monoxide

Parameters were fit for the R branch of the 4.7 µm CO band, over the range from 2150 cm^{-1} to 2270 cm^{-1}. The data were generated at a resolution of 1 cm^{-1}, resulting in an average spacing of 0.482 cm^{-1}. This was sufficiently high that the individual lines in the band were resolved.   Figure 3-13 (a) is a comparison of the extrapolated absorption coefficient from eqn. 3.5 to the one from HITEMP at 300 K.   The difference in the integrated absorption between the original and fit data, obtained from eqn. 3.6, is less than –0.1 %. The small error is expected because the reference spectrum was included in the training set. In Figure 3-13 (b), however, the extrapolated absorption coefficients are compared to the HITEMP data at 1000 K, which is 400 K above the highest temperature spectrum used in the fitting procedure. The difference in the integrated absorbance at this temperature is still only 3.6 %. While this agreement may be a little misleading because there is clearly a cancellation of errors, the magnitudes of the residuals (Figure 3-14) are on average at least an order of magnitude smaller than the absorbance values.

The spectra of heavier molecules are not as well resolved at elevated temperatures as is the CO spectrum shown in Figure 3-15. Closely spaced broadened lines will, in effect, smear out distinguishable line structure. Since this is the case for many fuels, it is important to investigate the effect of reducing the resolution on the accuracy of the extrapolations. Figure 3-15 (a) and (b) compare the extrapolated absorption coefficients and HITEMP data at 1000 K and 4 cm^{-1} resolution.   At this resolution, the CO line structure is gone and the band appears as a continuous absorption. The fit procedure was carried out using these data with similar results as the higher resolution case.   The

integrated absorbance at 1000 K using the fit parameters differed from the HITEMP data by only –0.28 %. The errors in the temperature extrapolations for CO appear to remain small for de-resolving the spectrum even though the contributions from overlapping rotational lines were not explicitly accounted for in the derivation of Eqn. 3.4.

Figure 3-13: Comparison of CO spectral absorption coefficient between HITEMP and data calculated using eqn. 3.3 with fit parameters at 1cm^{-1} resolution: (a) 300K and (b) 1000K.

Figure 3-14: Residual ($\kappa_{Fit} - \kappa_{Hitemp}$) for CO at 1000 K. This represents the difference between the data sets shown in Figure 3-13.

Figure 3-15: Comparison of CO spectral absorption coefficient between HITEMP and data calculated using eqn. 3.3 with fit parameter at 4cm^{-1} resolution: (a) 300 K, (b) 1000 K.

3.4.2.3 Carbon Dioxide

The accuracy of the extrapolation method for the 4.3 μm band in CO_2 over the spectral range 2250 cm^{-1} to 2350 cm^{-1} (P branch) was also examined. The procedure was carried out using data at two resolutions: 0.5 cm^{-1} and 4 cm^{-1}, resulting in average data spacing of 0.241 cm^{-1} and 1.93 cm^{-1}, respectively. The HITEMP and fit data at 300 K and 0.5 cm^{-1} resolution are compared in Figure 3-16 (a). In this case the difference in the integrated absorption coefficient was –2.1 %, compared with –1.1 % at 4 cm^{-1} resolution. At 1000 K, the difference at 0.5 cm^{-1} resolution was only –0.7 %. The HITEMP and fitted spectra are compared in Figure 3-16 (b). While the error in the integrated absorbance is small, a frequency resolved comparison, as indicated by the residual spectrum in Figure 3-17, does reveal a small, but noticeable systematic error between 2270 cm^{-1} and 2300 cm^{-1}. At 4 cm^{-1} resolution (and 1000 K), the difference in the integrated absorption coefficient at 1000 K is 1.3 %. The discrepancies are apparent in the comparison shown in Figure 3-18.

A summary of the integrated and residual RMS errors for the extrapolations of the HITEMP data is presented in Table 3-1. Chu et al. [62] report uncertainties on the order of 2 % - 3 % for the measurement of absorption coefficients in the NIST Quantitative Infrared Database. Additionally, their study reports that line intensity variations on the order of ± 10 % can frequently be found in comparisons of quantitative reference spectra. Although the cancellation of positive and negative errors makes it difficult to discern a pattern in the discrepancies between the integrated absorption coefficients obtained from direct calculation and the extrapolation, it does appear that the RMS errors grow more

rapidly with temperature in the extrapolations from the lower resolution spectra. However, in either case, the errors in the extrapolations are comparable to the experimental uncertainties reported by Chu.

Table 3-1: Summary of errors in the HITEMP extrapolations.

Molecule (resolution)	Reference Data	Integration Range (cm^{-1})	Error in integrated values		RMS of the residual	
			300 K	1000 K	300 K	1000 K
CO (1 cm^{-1})	HITEMP	2150 – 2270	-0.1 %	3.6 %	1.33 E^{-3}	1.11 E^{-3}
CO (4 cm^{-1})	HITEMP	2150 – 2270	0.3 %	-0.3 %	2.04 E^{-4}	1.10 E^{-3}
H_2O (4 cm^{-1})	HITEMP	3500 – 4000	-0.02 %	3.6 %	2.09 E^{-3}	4.85 E^{-3}
CO_2 (0.5 cm^{-1})	HITEMP	2250 – 2350	-2.1 %	-0.7 %	3.06 E^{-2}	1.45 E^{-2}
CO_2 (4 cm^{-1})	HITEMP	2250 – 2350	-1.1 %	1.3 %	1.36 E^{-2}	1.18 E^{-1}
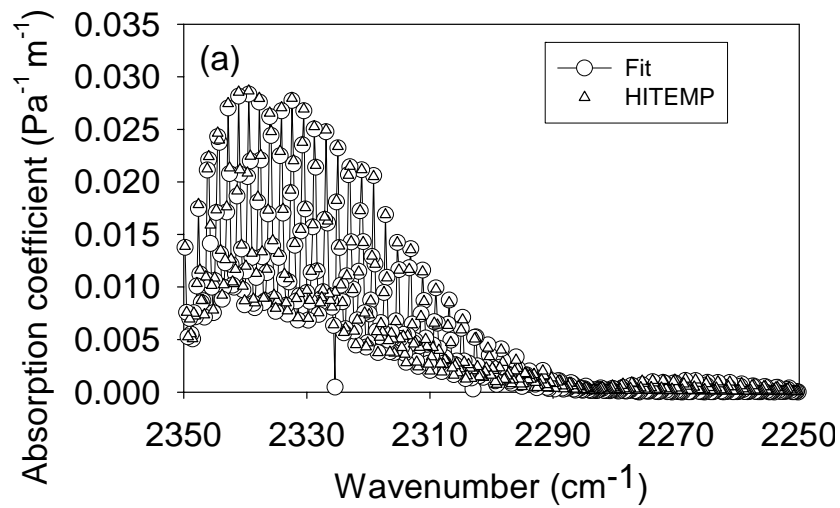
Figure 3-16: Comparison of CO_2 spectral absorption coefficient at 300 K between HITEMP and data calculated using eqn. 3.3 with fit parameters at 0.5 cm^{-1} resolution: (a) 300K, (b) 1000K.
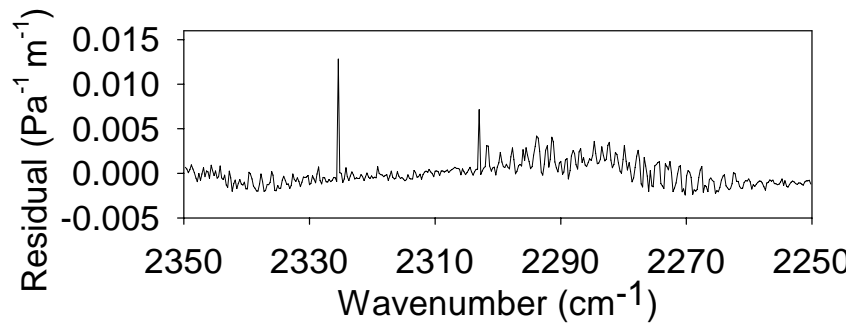
Figure 3-17: Residual ($\kappa_{Fit} - \kappa_{Hitemp}$) for CO_2 at 1000 K. This represents the difference between the data sets shown in Figure 3-16.
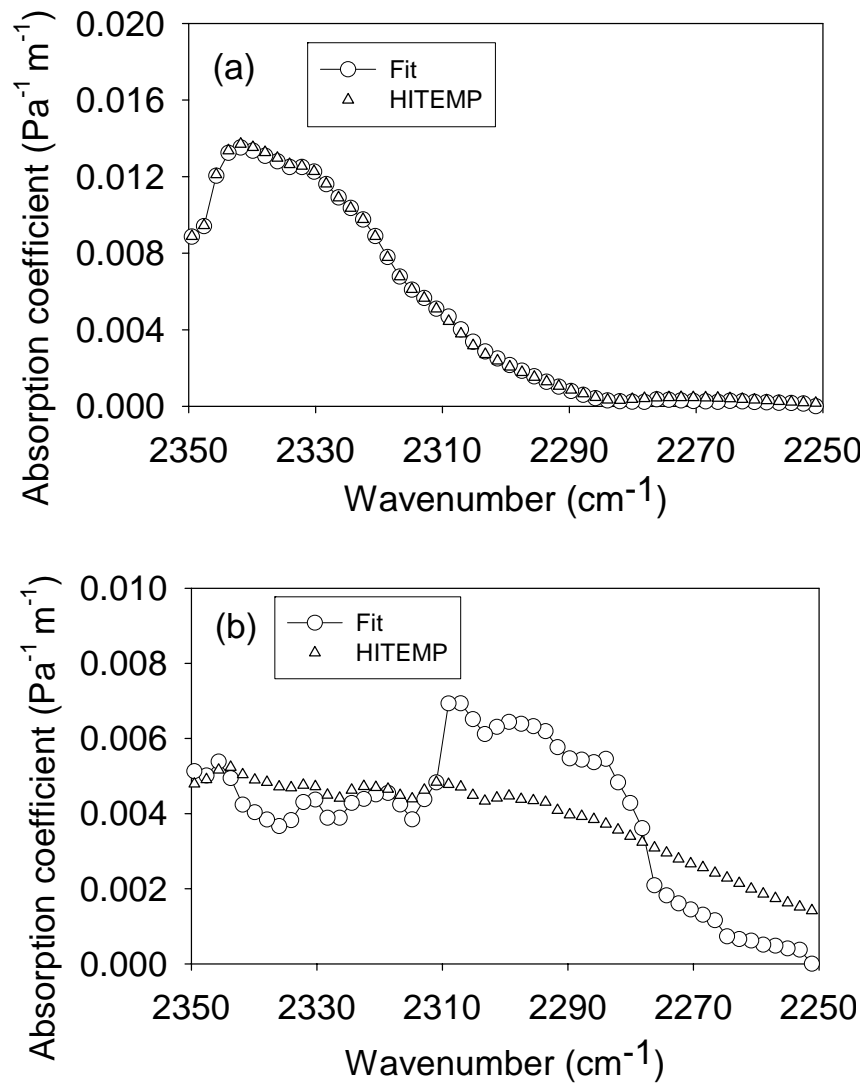
Figure 3-18: Comparison of CO_2 spectral absorption coefficient at 1000 K between HITEMP and data calculated using eqn. 3.3 with fit parameters at 4 cm-1 resolution: (a) 300K, (b) 1000K.

3.4.2.4   Water vapor

Parameters were fit to lines in the 2.7 μm water band, over the range between 3500 cm^{-1} – 4000 cm^{-1}. The temperatures used were the same as those in the CO case. The water absorption data was generated from the HITEMP database at a resolution of 4 cm^{-1}, resulting in an average data spacing of 1.93 cm^{-1}.   At this resolution, most of the line structure is still visible in this band. Figure 3-19 (a) is a comparison of extrapolated absorption coefficient from Eqn. 3.4 to the one from HITEMP at 300 K, using the parameters generated in the fit. The error from the fits at 300 K was comparable to the fits at 300 K for CO. The difference in the integrated absorbance was -0.02%. Again, a small error is anticipated because the parameters were fit to data at this temperature. However, the comparison is still favorable at 1000 K, where the difference in the integrated absorbance is only 3.6%. This result is shown in Figure 3-19 (b).   The residuals are shown as a function of wavenumber in Figure 3-20.

3.4.3   Experimental data

3.4.3.1   Propane

Figure 3-21 shows how the absorption coefficient for propane varies with temperature. The band broadens with increasing temperature as higher energy rotational states become populated. Furthermore, the peak absorption drops by more than an order of magnitude from 300 K to 1000 K. These changes in the shape and intensity of the absorption band are captured in the extrapolations.
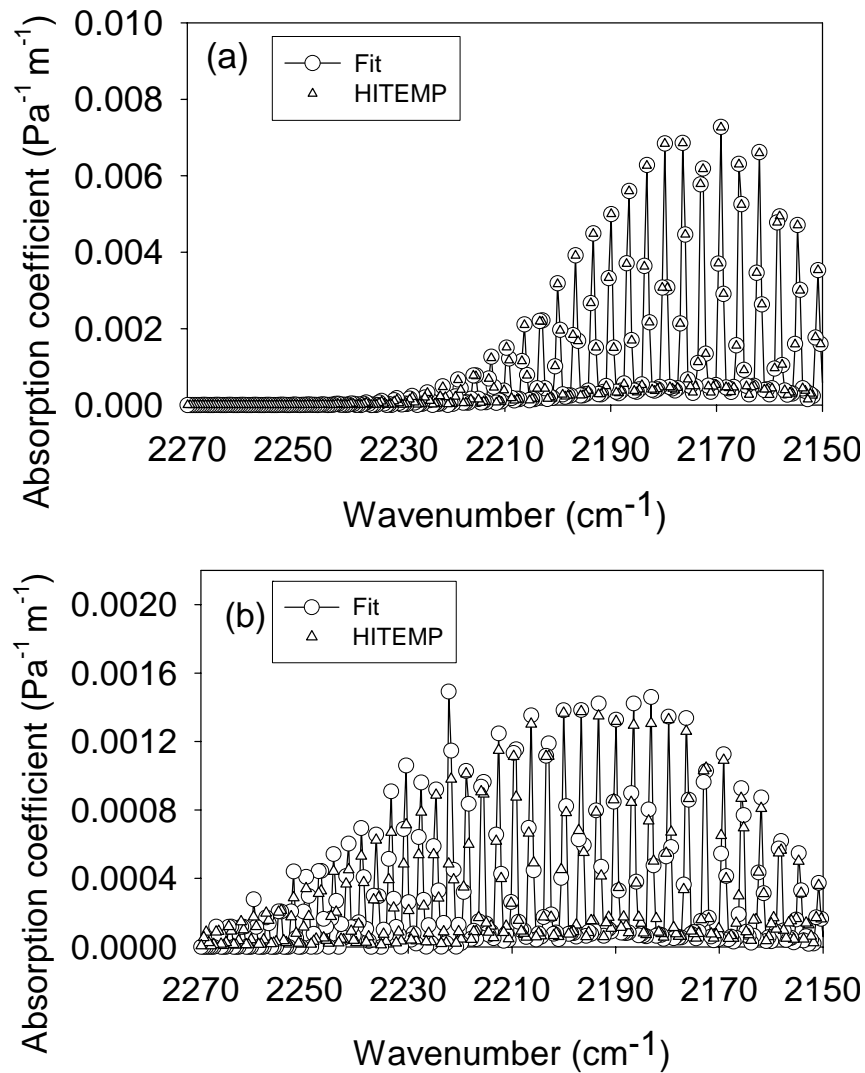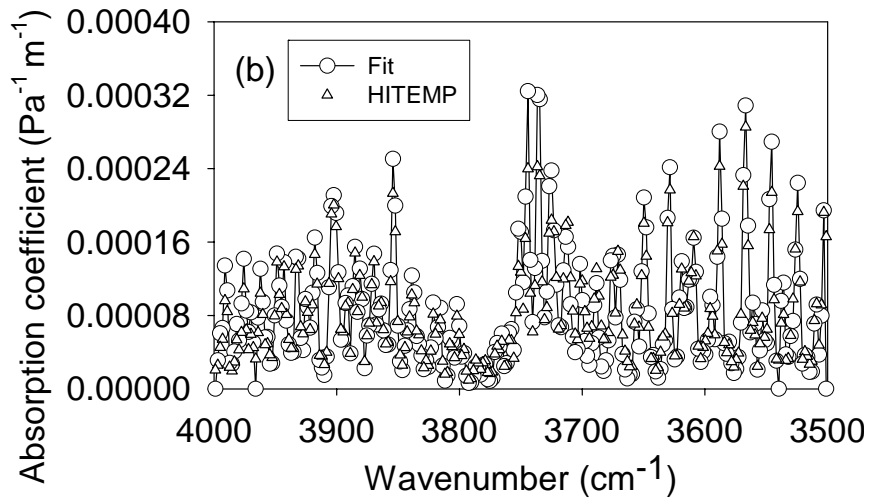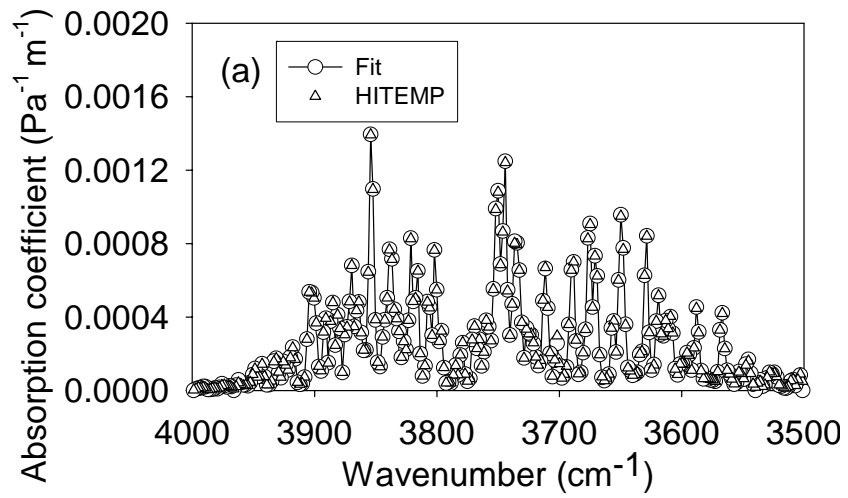
Figure 3-19: Comparison of water vapor spectral absorption coefficient between HITEMP and data calculated using eqn. 3.3 with fit parameters at 1cm^{-1} resolution: (a) 300K, (b) 1000K.
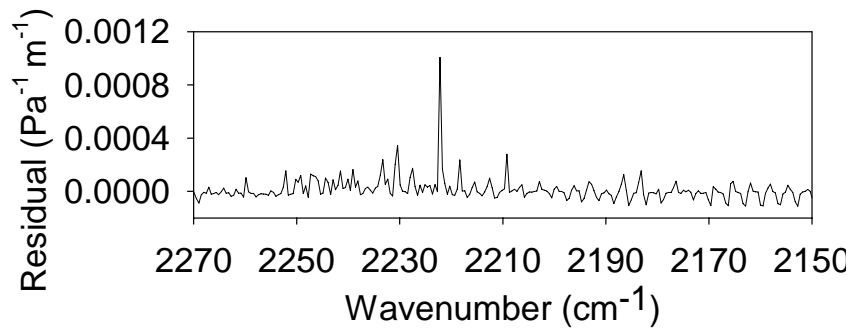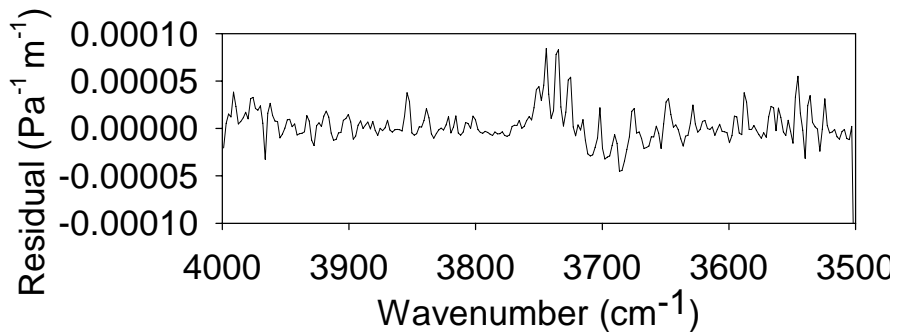

Figure 3-20: Residual ($\kappa_{Fit} - \kappa_{Hitemp}$) for H$_2$O at 1000 K. This represents the difference between the data sets shown in Figure 3-19.
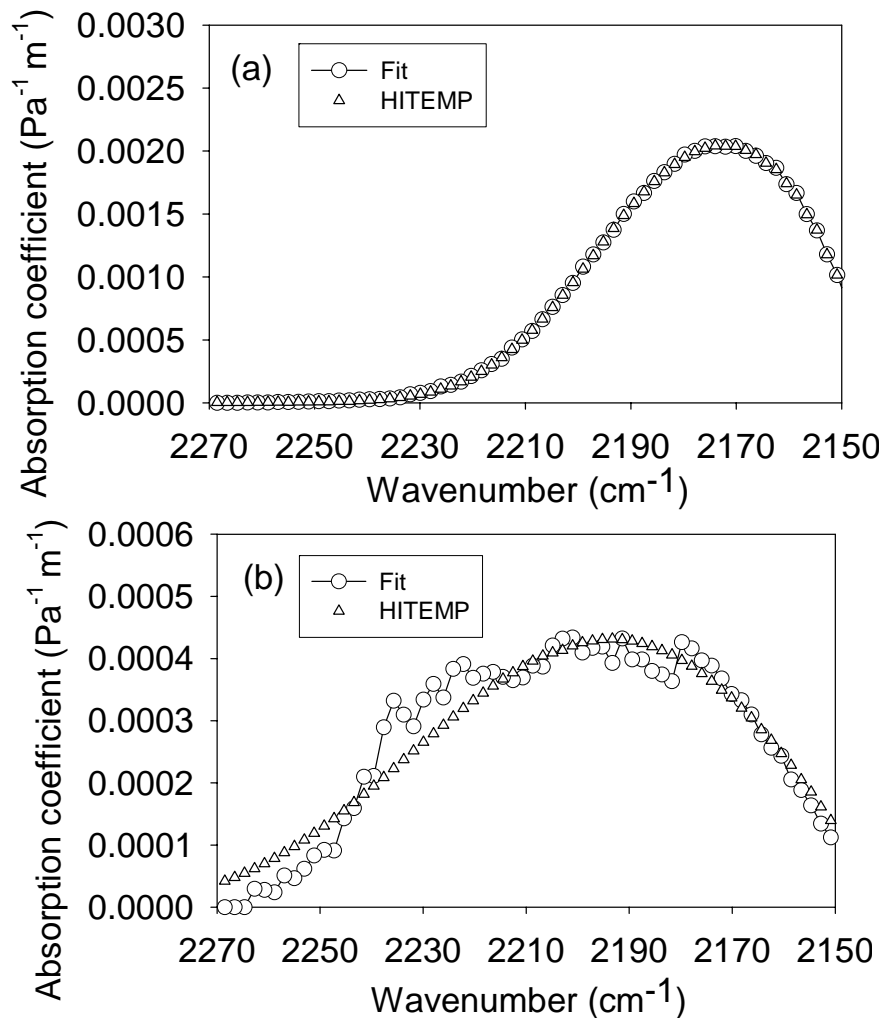
The extrapolated absorption coefficients at (a) 800 K and (b) 1000 K are compared to the corresponding experimental values in Figure 3-22. Although there is at least qualitative agreement, a more detailed comparison reveals that the extrapolations retain more structure at high temperature and underestimate the absorbance at the wings of the bands. The residuals at 1000 K are shown as a function of wavenumber in Figure 3-23. The fine structure apparent in the extrapolations is presumably an artifact resulting from the retention of structure in the fit parameters, which are based on measurements at lower temperatures. The discrepancy at the band wings is probably due to the inability of the extrapolations to capture the effects of "hot bands", corresponding to vibrational transitions that are not populated at the lower temperatures used in determining the fitting parameters. The accuracy of the extrapolations is better for frequencies in the vicinity of the band center (Table 3-2). These deficiencies in the extrapolation technique lead to errors in the integrated absorption coefficients at 800 K and 1000 K ranging from −20% to −12 % These deficiencies in the extrapolation technique lead to errors in the integrated absorption coefficients at 800 K and 1000 K ranging from −20% to −12 %, which accounts for the decomposition of propane at 1000K. Based on calculations using the CHEMKIN AURORA [63] with the University of California, San Diego, chemical-kinetics model [64], the decomposition of propane is negligible at 800 K and about 8.8 % at 1000 K.
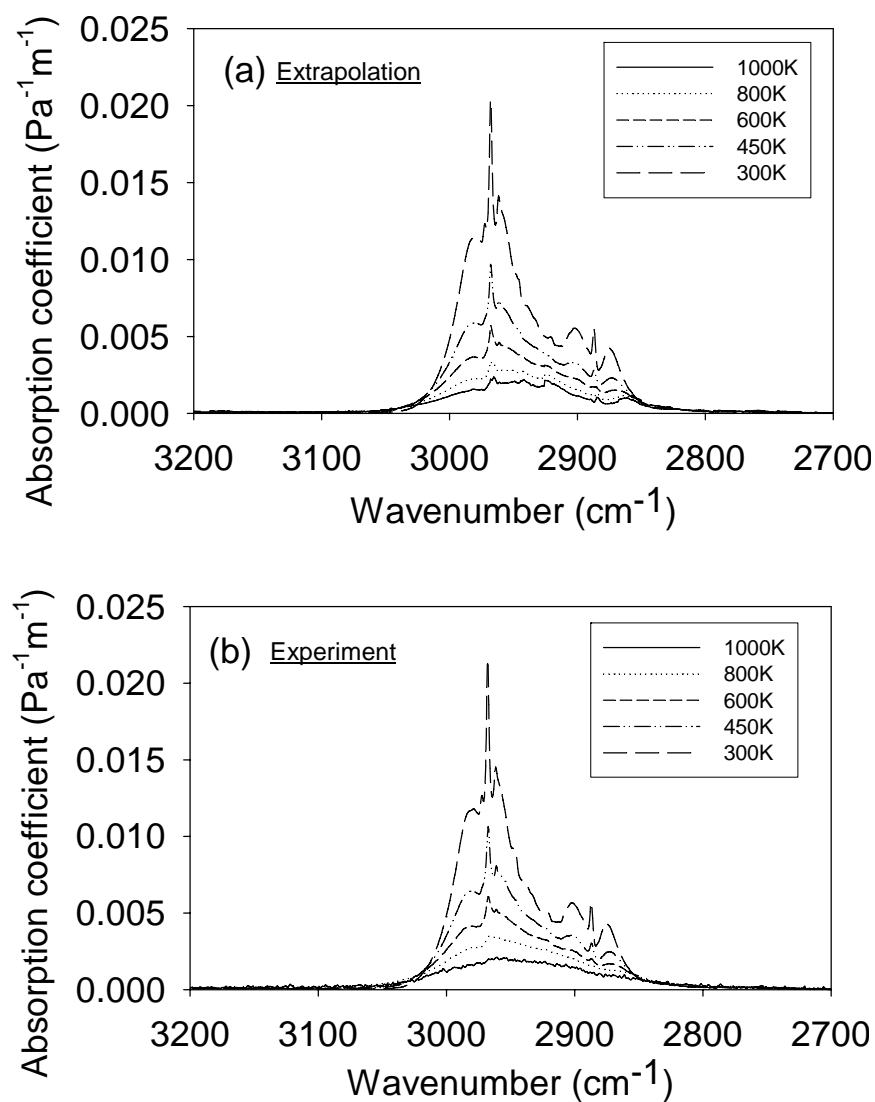
Figure 3-21: Comparison of C_3H_8 spectral absorption coefficient between experiment and data calculated using eqn. 3.3 with fit parameters at 1 cm^{-1} resolution: (a) Extrapolation, (b) Experiment.
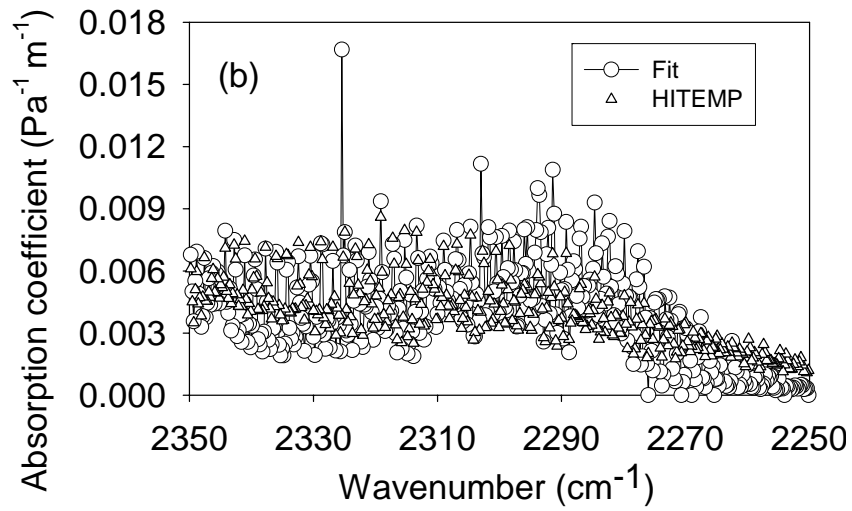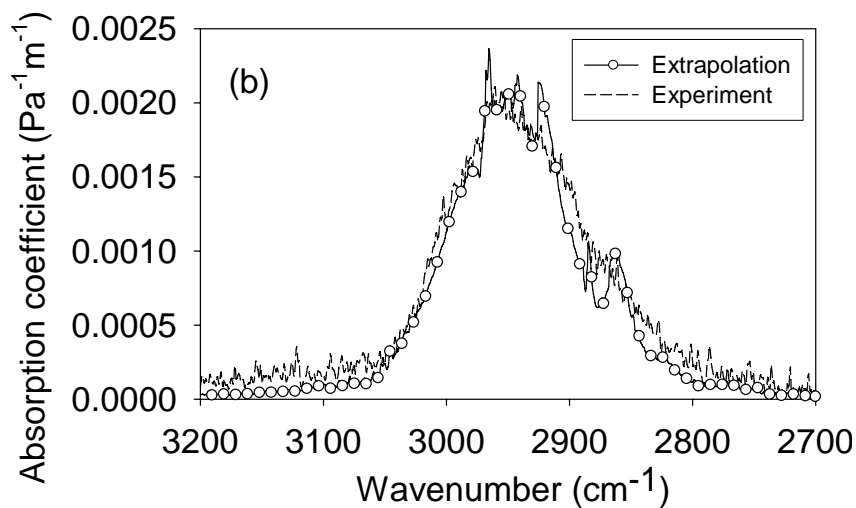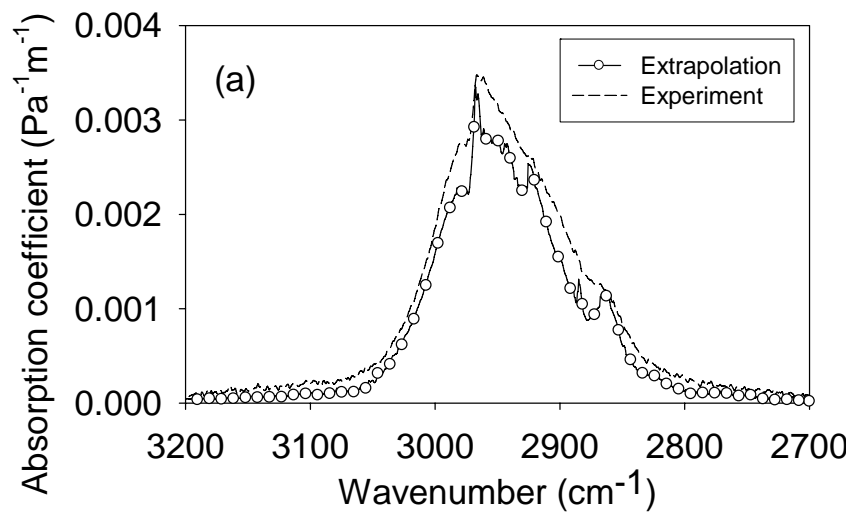
Figure 3-22: Comparison of C_3H_8 spectral absorption coefficient between experiment and data calculated using eqn. 3.3 with fit parameters at 1 cm^{-1} resolution: (a) 800K, (b) 1000K.
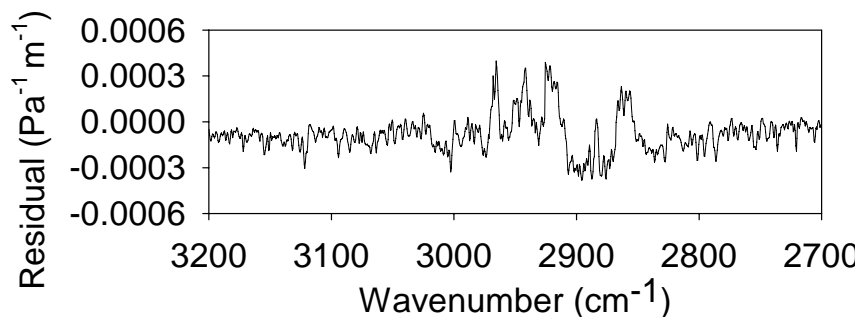

Figure 3-23: Residual ($\kappa_{Fit} - \kappa_{Experiment}$) for C_3H_8 at 1000 K. This represents the difference between the data sets shown in Figure 3-22.

Table 3-2: Errors in the integrated absorption coefficients for propane at 1 cm^{-1} resolution.

Integration Range (cm^{-1})	Integrated Absorption Coefficient (1/Pa/m) Upper: Extrapolation Lower: Experiment			Error in integrated values (%)		
	300 K	800K	1000 K	300 K	800K	1000 K
2700 –2850 (Right Wing)	0.027	0.022	0.020	6.5	-41.1	-40.8
	0.025	0.037	0.033			
2850 – 3050 (Band Center)	0.656	0.324	0.244	-6.7	-15.9	-4.3
	0.703	0.385	0.255			
3050 – 3200 (Left Wing)	0.015	0.013	0.011	18.5	-53.7	-59.0
	0.013	0.027	0.026			

3.4.4 Application of extrapolation technique

The simple extrapolation method has great advantage in that absorption coefficient data can be extrapolated to high temperature, which is difficult to measure. It can also be calculated at any arbitrary temperature.

Figure 3-24 shows the comparison between fitting and HITEMP data of carbon monoxide, water vapor and carbon dioxide at 550 K. From the figures and errors in the table, the simplified extrapolation equation is seen also to work well to calculate absorption coefficient at any arbitrary temperature.

(a)

(b)

85
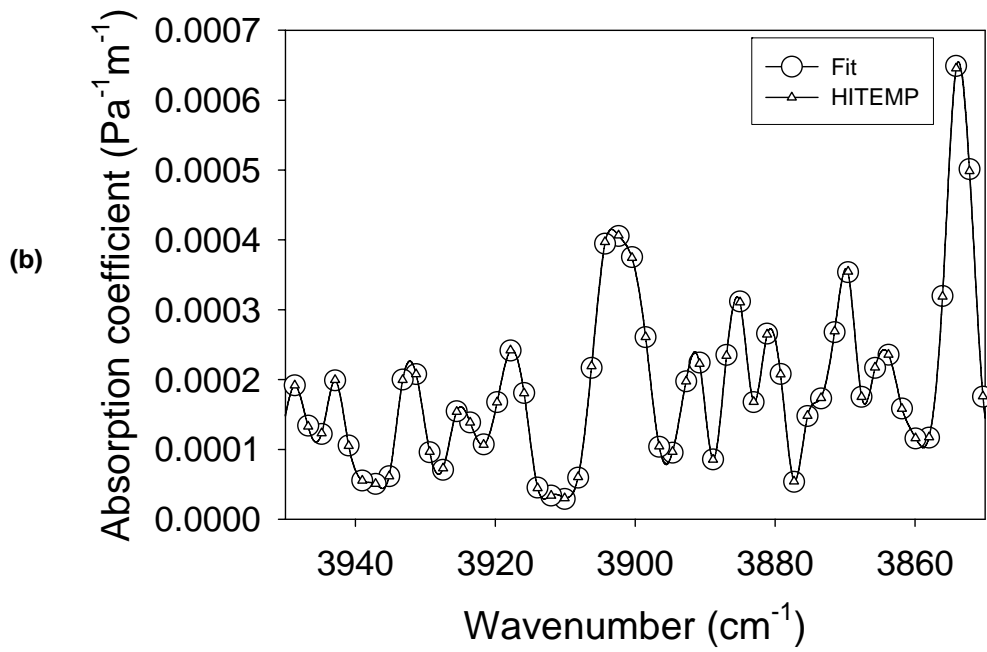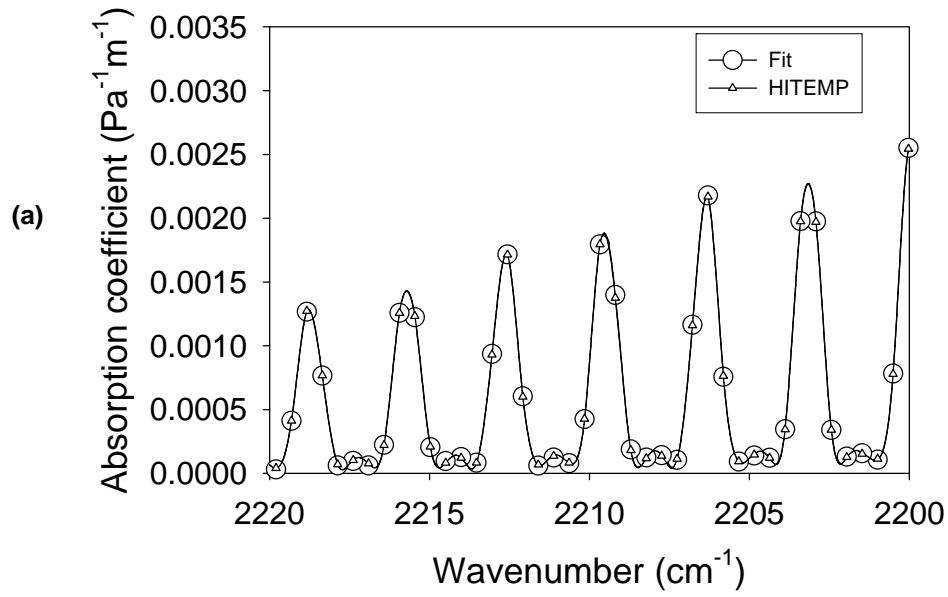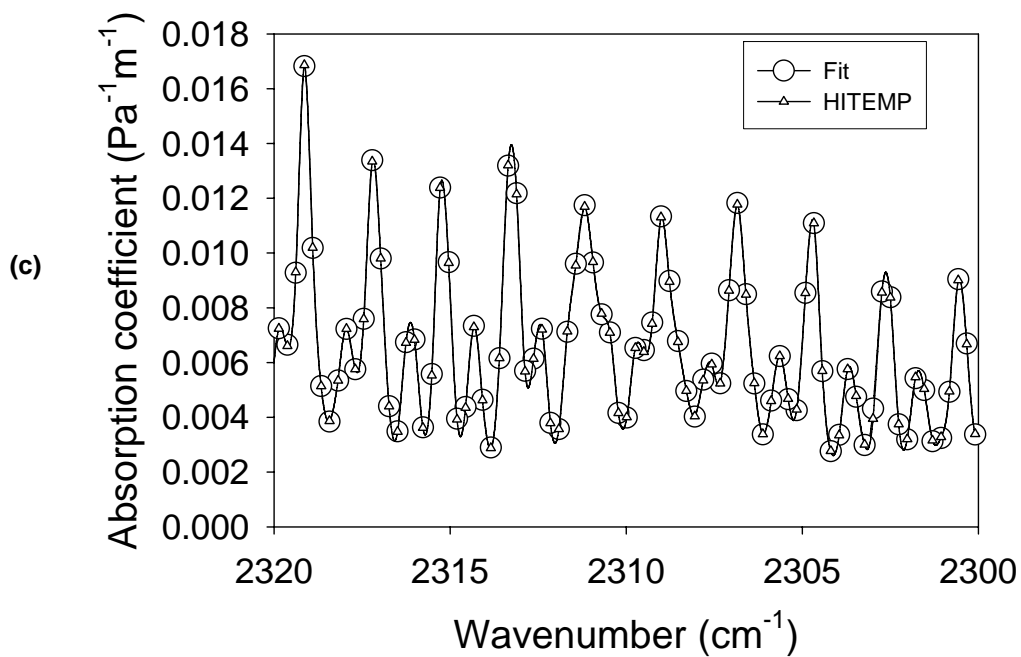
Figure 3-24: Comparison of (a) CO, (b) Water, and (c) CO_2 spectral absorption coefficient between HITEMP and fitted data at 550 K

Table 3-3: Errors of the integrated absorption coefficients in the HITEMP fitting at 550 K.

550 K	CO	H_2O	CO_2
Error (%)	0.3	0.3	0.8

3.4.4.1 Effect of fuel pyrolysis

Because the current study explored very high temperatures both experimentally and with fit extrapolations, it is important to consider how fuel pyrolysis influenced the measurements and subsequent calculations for Planck mean absorption coefficient. Pyrolysis of the fuels of interest were calculated using the Aurora program in CHEMKIN [63] for temperatures up to 1800 K.

Figure 3-25 shows results of the normalized volume fraction for the fuels. The chemical kinetics model was based on the UC San Diego, chemical-kinetics model for propane, heptane, methanol [64] and MIT model for toluene [65]. The experimental cell conditions with the calculated residence times (ranging from 15 s at 300 K down to around 3 s at 1000 K) were input into Aurora [63] and pyrolysis of each species within the cell was calculated. Figure 3-25 shows that heptane begins pyrolyzing at about 900 K, and is about 77% degraded at 1000 K. Figure 3-26 compares the heptane infrared spectrum obtained by experiment and the extrapolation at 1000 K. The extrapolated data was obtained by using the simplified extrapolation technique [60]. It was assumed that no fuel pyrolysis occurred at any temperature. This plot indicates that significant heptane pyrolysis has occurred at 1000 K, which is consistent with the results from Ref. [63]. For the other species, pyrolysis of methane, propane, and propylene begins at 1200 K, 900 K and 950 K, respectively. Radiation calculations using Planck mean absorption coefficients above a fuel's pyrolysis temperature should be modified to account for fuel pyrolysis.

In general, the measurements suggest that the significance of various fuel species absorption in a fire will in part depend on the temperature character of the radiation. Since 800 K is not atypical for internal temperatures of large fires, it is clear that detailed radiative transport calculations including temperature effects may be necessary to resolve heat feedback to fuel sources.

Another important question regarding radiation feedback involves the question of fuel pyrolysis products and how they impact overall absorption. In this regard, propylene and methane are interesting molecules as both can be prominent pyrolysis products during the

breakdown of larger hydrocarbons such as heptane. In fact two C_3H_6 molecules plus one CH_4 molecule has the same number of C's and H's as C_7H_{16}, and at least at high temperature ($T > 800$ K), the sum of Planck mean absorption coefficients for the smaller molecules is only slightly higher than that of the larger heptane molecule. At lower temperature ($T < 600$ K), the smaller molecules have much higher Planck mean absorption coefficients whereas the larger n-heptane does not. This suggests that if pyrolysis products find their way either through diffusion or convection into cool regions of the flame core, the impact of pyrolysis on hydrocarbon radiation absorption may be very significant. This is an area for further study, both with additional data collection and with detailed modeling of large-scale pool fires in which chemically resolved fuel rich cores and detailed radiation transport calculations are developed.
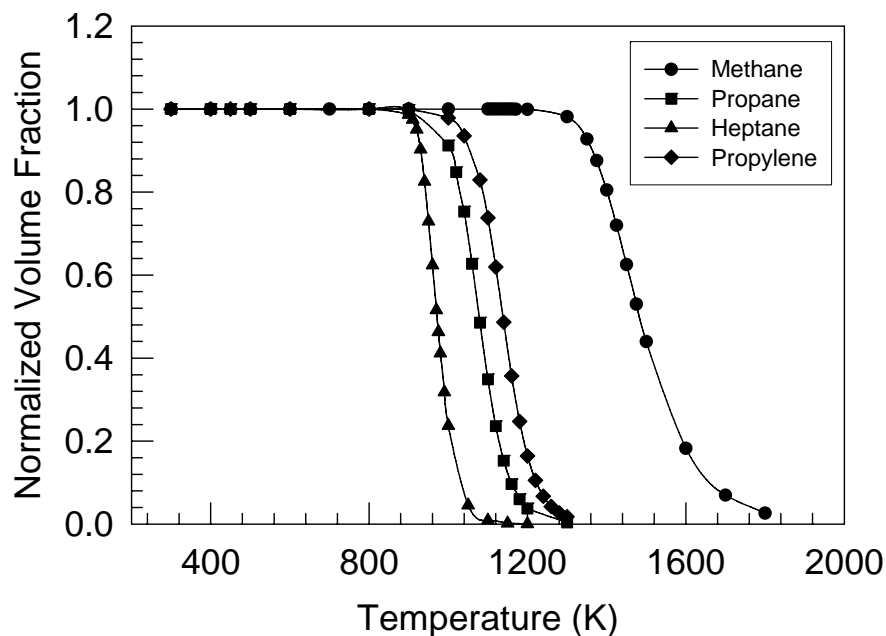
Figure 3-25: Calculated normalized fuel volume fraction of hydrocarbon fuels remaining after residence in gas cell as a function of temperature.
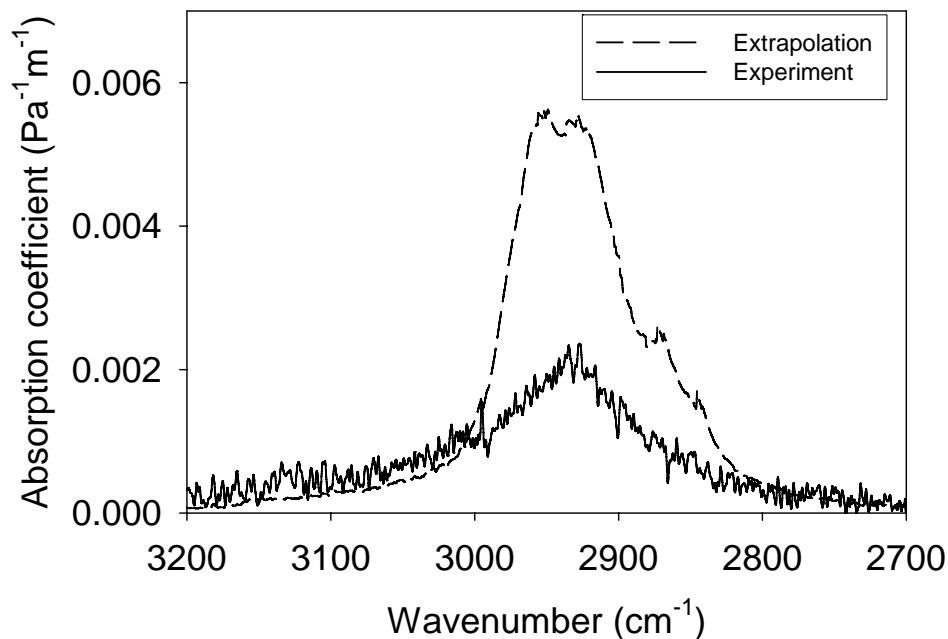
Figure 3-26: Comparison of the extrapolated and experimentally measured spectral absorption coefficient of heptane (C_7H_{16}) for the C-H stretching band at 1000 K. The difference between extrapolated (----) and measured (—) spectrum is due to pyrolysis.

3.5   Conclusion

Infrared spectra of gas and liquid fuel species measured using unique high temperature FTIR introduced in chapter 2 were presented. Propane, heptane, methanol, toluene, propylene and methyl methacrylate (MMA) infrared absorption coefficients were presented as a function of temperature from 300 K to 1000 K. As temperature increases, absorption coefficients for each fuel decrease around the band peaks, but the band wings are increased due to shifted and broadened rotational transition. The characteristic band peak for each fuel molecule decreased and became noisy because lower vibrational states become less probable with higher temperatures and the spectrum featured vibrational and rotational energy transition at higher energy levels. A simplified extrapolation technique for absorption coefficient was developed and evaluated by HITEMP database and

propane spectrum. Uncertainty of extrapolating the fit to high temperature was ≤ 20 % and interpolation within the temperature measurement window was ≤ 10 %. The fuel pyrolysis problem at high temperature was investigated by CHEMKIN AURORA, and evaluated the possibility of fuel pyrolysis during high temperature infrared measurement. All fuels studied are not expected to undergo significant (> 10%) pyrolysis with the exception of n-heptane at 1000 K. The extrapolation technique is expected to enable an infrared spectrum to be obtained up to 1000 K, but not for higher temperatures due to fuel pyrolysis changing the characteristics of the infrared absorption spectra.

CHAPTER 4   DEVELOPMENT OF A RADIATION ABSORPTION DATABASE

4.1   Introduction

The radiation absorption coefficient databases, currently used in combustion and fire modeling, have been used for 20 years. Highly resolved combustion products absorption coefficient database has been updated, but fuel information has not. To model and predict radiation feedback study within various fires, it is critical to develop and update the absorption coefficient database. In this chapter, current databases (HITRAN, HITEMP, and RADCAL), and the concept and the design of a new radiation absorption database (RADCAL2) are introduced. Finally, the new database is used to derive Planck mean absorption coefficients for fuels under fire conditions.

4.2   Current database

4.2.1   HITRAN and HITEMP

The HITRAN database was first developed in the 1960's at Air Force Cambridge Research Laboratory to investigate deeply the infrared spectra for the atmosphere. HITRAN started from seven species and has now expanded to 39 species in the 2004 edition [66]. This database is used for infrared sensing such as qualitative analysis for atmosphere and space and quantitative analysis for environmental gases. HITRAN offers the parameters obtained by experiment and calculation to obtain line-by-line intensity with high resolution.

HITRAN can calculate temperature dependent line intensity based on 296 K data up to 3000 K, but the high temperature data is verified experimentally only up to 600 K, since HITRAN misses the information regarding vibrational transition hot bands, which happen at high temperatures above 1000 K. HITEMP, which include this vibrational transition, was developed in 2000 to include these high temperature bands for H_2O, CO_2, and CO. Modest et al. [67] and Fleckl et al. [61] verified the high temperature line intensities experimentally up to 1550 K. The line intensity is generated to incorporate the database into other program, but user friendly commercial programs such as E-Trans can calculate spectral transmissivity and absorptivity by input of concentration, temperature, resolution, and pathlength.

4.2.2 RADCAL

The RADCAL [46] was developed in the 1970's and the 1980's. (Current version was in 1993) to calculate spectral transmissivity, radiation intensity, and several mean absorption coefficients, such as the Planck mean, wall-incident mean, and effective mean, of non-isothermal gas mixtures at line of sight with the current version completed in 1993 [46]. This database uses both experimental and modeled data of H_2O, CO_2, CO, and soot with a 25 cm^{-1} resolution. RADCAL utilizes narrow band models to calculate detailed absorption coefficients from 25 cm^{-1} resolution data. Accuracy is less than HITRAN and HITEMP, but the input files and user-friendly programming makes combustion modeling easily adapted for engineering radiation calculation. FDS uses RADCAL to calculate the Planck mean and effective mean absorption coefficient as a function of temperature and mixture fraction.

4.3   New database

4.3.1   Concept and database structure

A new RADCAL database was programmed with additional new fuel species absorption coefficients for methane (updated), propane, heptane, methanol, toluene, propylene, and methyl methacrylate, and the updated absorption coefficient data for CO_2, H_2O, CO, and soot. The database was incorporated into a one dimensional radiation transportation analysis in order to verify how updated radiation information affects incident heat flux on the fuel surface.   The database had been made ready for complete integration into NIST's FDS simulation package, which is expected to be completed in 2005.

The current input file style of RADCAL (temperature, species concentration and path length), was not changed since the problem of the current version is the number of fuel specie, and resolution. High resolution (1 cm^{-1} with 0.48 cm^{-1} line spacing) and low resolution (16 cm^{-1} with 7.9 cm^{-1} line spacing) tabulated databases as a function of wavenumber from 50 cm^{-1} (200 μm) to 25000 cm^{-1} (0.4 μm) and temperature from 300 K to 2400 K with 50 K increments were created for well-resolved spectral 1-D radiation transportation analysis and for radiation calculation in FDS.

4.3.2   Fuel absorption database

A fuel database was created using an interpolation and extrapolation absorption coefficient program written in Matlab. The program uses three fitting parameters and two

variables described in the extrapolation technique section in 3.4.1, and generates tables

for spectral information of absorption coefficient, transmissivity, absorptivity, and

integrated value of absorption coefficient and Planck mean absorption coefficient for

seven fuels obtained by experiment and HITRAN.   Input parameters are series of

temperatures, concentrations, and pathlengths, as well as the current and new RADCAL.

Table 4-1: Spectral ranges used in the absorption coefficient database for fuels.

Specie	Methane[*] Propane Heptane	Methanol	Toluene	MMA	Propylene
Spectral range Wavenumber (cm^{-1})	1300 – 1600 1150 – 1600[*] 2700 - 3200	900 - 1600 2700 - 3200 3600 - 3800	700 - 800 1000 - 1150 1300 - 1900 2700 - 3200	750 - 1950 2700 - 3200	750 - 1150 1250 - 1950 2700 - 3200

4.3.3   Combustion product database (CO_2, H_2O, and CO)

E-trans with HITEMP database by Spectrasoft Inc., was used to make a spectral

absorption coefficient database for CO_2, H_2O, and CO. Temperature (from 300 K to

2400 K), total pressure (760 mmHg), species concentration (1000 ppm), pathlength

(0.3175 m), and resolution (1 cm^{-1} or 16 cm^{-1}) were input parameters.   Spectral

transmittance for each species was calculated by E-trans, and converted to spectral

absorption coefficient. Wavenumber range to make the absorption coefficient table is

described in Table 4-2.

Table 4-2: Spectral ranges used in the absorption coefficient database for water vapor, carbon dioxide and carbon monoxide by HITEMP.

Specie	Water vapor	Carbon dioxide	Carbon monoxide
Spectral range (cm^{-1})	0 – 2600 2800 - 4500 4700 – 6000 6500 - 7700	550 – 900 2100 – 2450 3300 - 3800	1750 - 2400

4.3.4 Combustion product database (Soot)

Although an infrared active material has discrete characteristic wavelengths which represents the motion of the molecule structure, soot emits and absorbs continuous thermal radiation in the infrared region. Therefore, the amount of soot volume fraction strongly affects the entire infrared radiation emission and absorption both inside and outside a fire.

Spectral soot absorption coefficient was generally modeled by the Rayleigh limit expression since the largest soot particle size is smaller than infrared wavelengths and negligible against scattering [47]. The Rayleigh limit expression is written as

$$\kappa_\lambda = \frac{36\pi nk}{\left(n^2 - k^2 + 2\right)^2 + 4n^2k^2} \cdot \frac{1}{\lambda} \qquad [m^{-1}] \quad (4.1)$$

where n is refractive index, k for absorptive index and λ for wavelength (m), respectively.

Many researchers have investigated optical properties of soot. Notable work about soot properties are Dalzell and Salofim (propane soot) [68], Lee and Tien (polystylene and PMMA) [5], Chang and Charalampopoulos (propane soot) [69], and Felske and coworkers (propane soot) [70]. Comparison of soot optical properties on these authors was summarized by Modest [47], and absorption coefficient based on each authors' value were compared at 3 μm. Modest reported that the optical properties of these authors

except Felske were given in close agreement, and that Felske's value is the lowest due to a low value of k.

Spectral refractive index n and absorptive index k are functions of wavelength. Chang and Charalampopoulos [69] for propane soot has polynomial expression for both n and k, as functions of wavelength (μm) and convenient to make various resolution soot spectral absorption coefficient. Therefore, soot absorption coefficient database were made based on equation 4.1 to 4.3. Expressions for refractive and absorptive indexes are:

For refractive index,

$$n = 1.8110 + 0.1263 \ln \lambda + 0.0270 \ln^2 \lambda + 0.0417 \ln^3 \lambda \qquad (4.2)$$

For absorptive index,

$$k = 0.5821 + 0.1213 \ln \lambda + 0.2309 \ln^2 \lambda - 0.0100 \ln^3 \lambda \qquad (4.3)$$

where, λ is wavelength (μm).

Figure 4-1 shows the spectral absorption coefficient of propane soot modeled by equations 4.1 to 4.2.

Although soot may have a temperature dependency on the absorption coefficient at low temperature according to Lee and Tien [5], a temperature independent absorption coefficient was adopted for the new absorption coefficient database because optical properties taken by Chang was temperature independent.
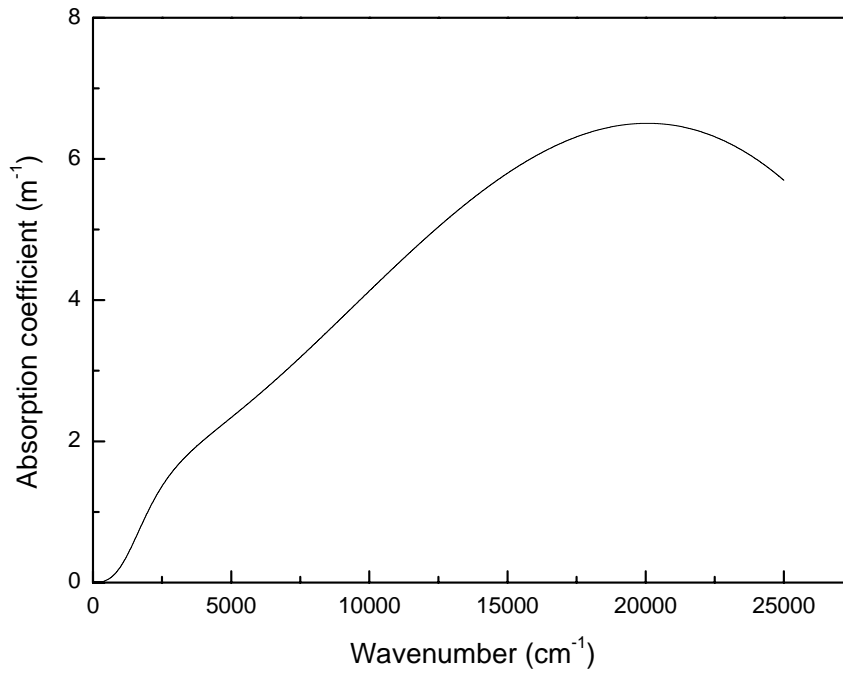
Figure 4-1: The modeled spectral absorption coefficient of soot.

4.3.5   Planck mean absorption coefficient

The intensity of thermal radiation from flames is diminished by absorption and augmented by emission as it travels through the atmosphere of a fire. The emissivity of the participating medium (at temperature T) is given by Planck mean absorption coefficient, which is expressed as an integral of the product of the spectral absorption coefficient κ_ν and the blackbody Planck function $E_{b\nu}$ over all wavenumber ν [71]:

$$\kappa_p = \frac{\int_0^\infty \kappa_\nu E_{b\nu} d\nu}{\sigma T^4} \qquad (4.4)$$

Here σ denotes the Stephan-Boltzmann constant. Since Planck mean absorption coefficient is a function only of temperature, it can be easily presented in tabular form [72].

Approximate values for κ_p are obtained by numerical integration and the accuracy increases with the resolution of the spectral measurements. Accurate κ_p are important in combustion and fire modeling for solution of the radiative transport equation without employing computationally expensive calculations. Use of κ_p approach is limited by the scarcity of temperature dependent data κ_ν. The κ_p is calculated for a range of fire conditions and the impact of hydrocarbon absorption on radiation from large-scale fires is discussed.

4.3.5.1 Hydrocarbon fuels

Figure 4-2 shows κ_p for methane (obtained from HITRAN), propane, heptane, and propylene (interpolated and extrapolated from the experimental data), as a function of temperature up to 1400 K in 50 K increments. Table 4-3 summarizes the fourth order polynomial fits to the data (Eqn. 4.5) shown in Figure 4-2.

$$\kappa_p = a_0 + a_1 T + a_2 T^2 + a_3 T^3 + a_4 T^4 \qquad (4.5)$$

Figure 4-2 show that both propane and heptane have similar characteristics. The number of -CH_2- groups impacts the magnitude of the absorption coefficient, but it does not influence the general trend of κ_p. Methane exhibits a peak in κ_p at much lower

temperatures than the two larger alkanes due to an increased proportion of its absorption occuring in the low-frequency bands. Figure 4-3 shows the absorption coefficient of C-H bending peaks for methane, propane, and heptane at 296 K. Since the absorption coefficient of the bending motion within a methane molecule is larger than that of propane and heptane at 1300 cm^{-1}, the methane κ_p is larger compared to propane up to about 400 K and similar to heptane at 300 K.

Propylene has the largest κ_p from 300 K to 500 K of hydrocarbon fuels due to contributions of $=CH_2$ and CH_3- bending, but the effect of the bending band on the mean absorption coefficient is diminished above 800 K where blackbody emissions peak well above the frequency of those bands. In contrast, the CH_3-, CH_2- and $=CH_2$ stretch bands contribute to emission and absorption of blackbody radiation. For temperatures above 800 K, propane with the two extra C-H bonds, has a slightly higher absorption coefficient than propylene because for the extra low frequency bands for propylene contribute very little to the blackbody radiation. The results for propylene from the experiments in this paper compare very favorably with previous studies by Brosmer et al. [13]. Since transmittance of the ZnSe window used in the gas cell experiments in this study rapidly falls off below 700 cm^{-1} (above 14.3 μm) as temperature increases [73], the absorption spectrum of the low frequency 578 cm^{-1} band was not measurable in the current study. Brosmer et al. [13] calculated Planck mean absorption coefficient of propylene with and without the 578 cm^{-1} band by approximation from the result of Load et al. [74] and Silvia et al. [75]. They estimated the inclusion of the band gave 15 %, 10 %, and 5 % of the total absorption for blackbody emissions at 300 K, 400 K and 550 K respectively and rapidly dropped below 1 % for higher temperatures. The κ_p of propylene was corrected

to include the 578 cm^{-1} band and results showed that the current Planck means absorption coefficient was typically 15 % higher than those of the previous study for the range of temperatures measured.

Table 4-3: Values for 4th order polynomial fits with equation 4 to Planck mean absorption coefficient data of hydrocarbon.

	Methane	Propane	Heptane	Propylene
	300 K - 1400 K	300 K - 1400 K	300 K - 1400 K	300 K - 1400 K
a0	-1.8267E-05	-9.2136E-05	-1.5179E-04	3.3532E-04
a1	3.9617E-07	4.6676E-07	6.6905E-07	-3.4358E-07
a2	-7.7619E-10	-1.7967E-10	3.4879E-10	-1.5077E-10
a3	5.7857E-13	-2.4935E-13	-1.1117E-12	3.5885E-13
a4	-1.5283E-16	1.3570E-16	4.4372E-16	-1.3216E-16
R^2	9.9196E-01	9.9527E-01	9.9507E-01	9.9823E-01
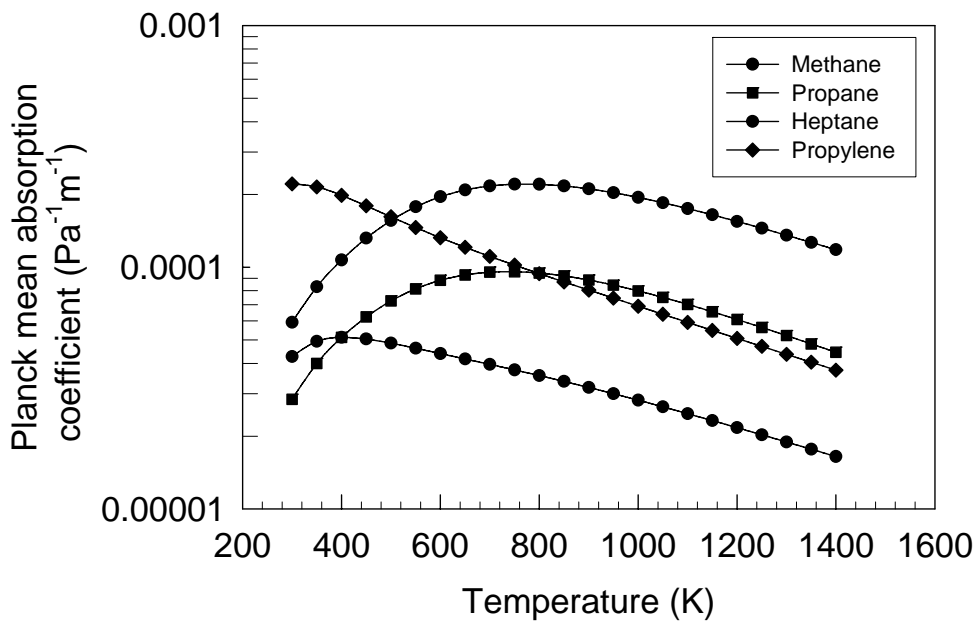
Figure 4-2: Planck mean absorption coefficient of CH_4 (from HITRAN), C_3H_8, n-C_7H_{16}, and C_3H_6 (from fitting and extrapolation of measurements).
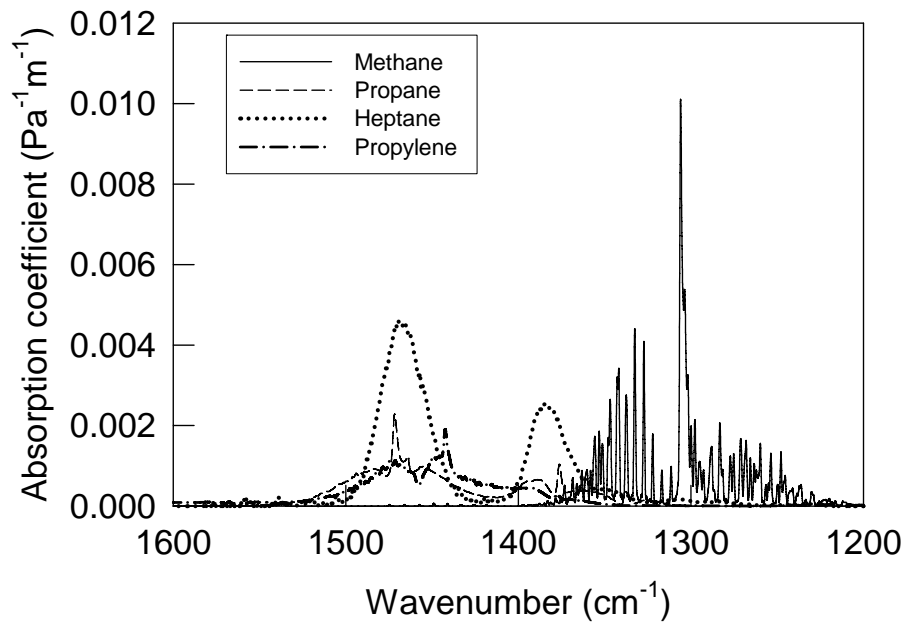
Figure 4-3: Spectral absorption coefficients for C-H bending peaks for methane (HITRAN), and propane and heptane (experimental) at 296 K.

4.3.5.2   Other fuels

Planck mean absorption coefficient for methanol, toluene and methyl methacrylate (interpolated and extrapolated from the experimental data), as a function of temperature up to 1400 K in 50 K increments are shown on Figure 4-4.   Table 4-4 summarizes the fourth order polynomial fits to the data (Eqn. 4.5). Figure 4-4 shows that methanol, toluene and methyl methacrylate have similar characteristics, due to many bands at low wavenumber range. This is in contrast to the alkanes, which have primarily C-H related bands.

Figure 4-5 shows the absorption coefficient of methanol, toluene and methyl methacrylate at room temperature. Since methyl methacrylate has the largest number of characteristic bands with large absorption coefficient at low wavenumber up to 1800 cm^{-1}

of all fuels, methyl methacrylate has the largest Planck mean absorption coefficient over the entire temperature range.

It is also interesting to compare methanol and toluene, since both have the same CH_3-, but each has different bonding (C-O and -OH or phenyl carbon double C=C, respectively) in their chemical structure. From 300 K to 1100 K, methanol has a larger Planck mean absorption coefficient than toluene. This is mainly due to the contribution of a C-O stretching peak. In contrast, the effect of CH_3-, and =CH stretch bands of toluene increases higher than 1100 K. Planck mean absorption coefficient of heptane increases up to 800 K, but is smaller than toluene up to 550 K and methanol up to 700 K.

Since the transmittance of the ZnSe window starts falling below approximately 700 cm^{-1} (14.3 μm) and drops dramatically below 625 cm^{-1} (16 μm) as temperature increases [73], the absorption spectrum of phenyl out-of and in-plane bending peak around 460 cm^{-1} band were not measurable. Figure 4-6 shows the comparison of our results and previous work done by Park et al. [13, 14]. There is an error of 19.3 % min. at 400 K and 31.1 % max. at 800 K between the two results. They used the total absorbance to generate Planck mean absorption coefficient because of their low-resolution spectrum, compared to our high-resolution analysis. Therefore, the difference between our result and previous work on methyl methacrylate is attributed to the experimental resolution and calculation method for Planck mean absorption coefficient.
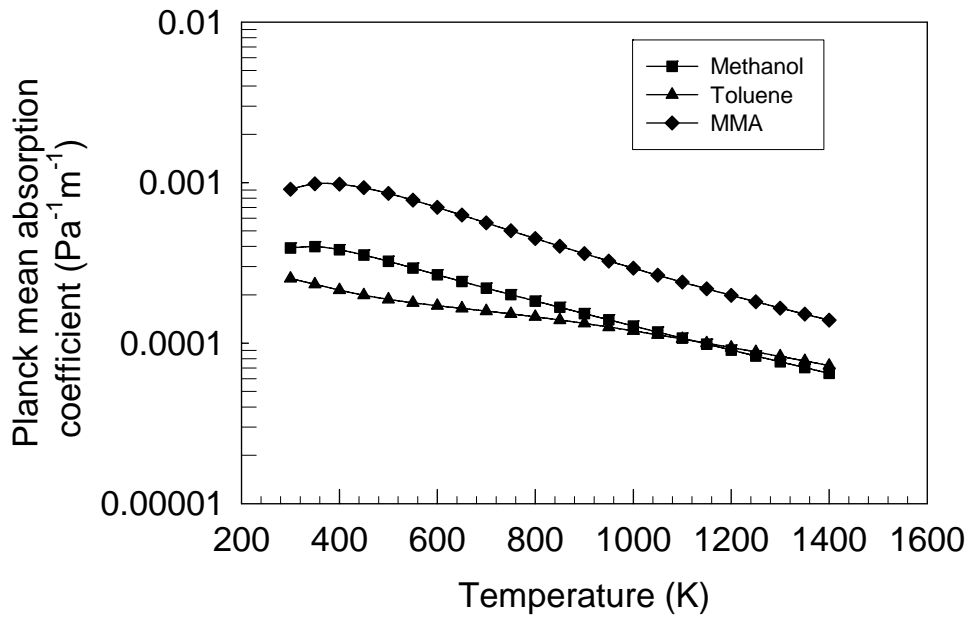
Figure 4-4: Planck mean absorption coefficient of methanol, and toluene, methyl methacrylate (MMA) (from fitting and extrapolation).
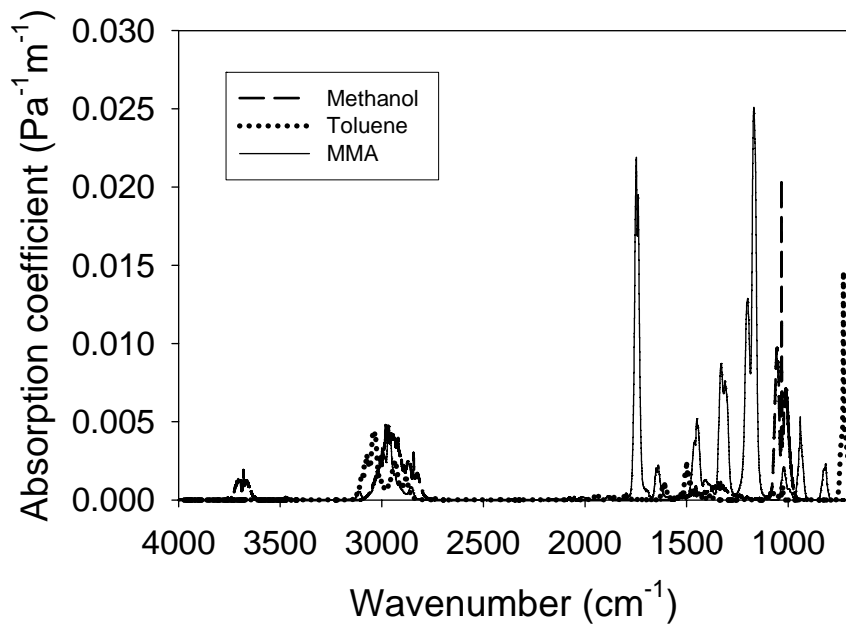
Figure 4-5: Spectral absorption coefficient of methanol, toluene and methyl methacrylate at room temperature.
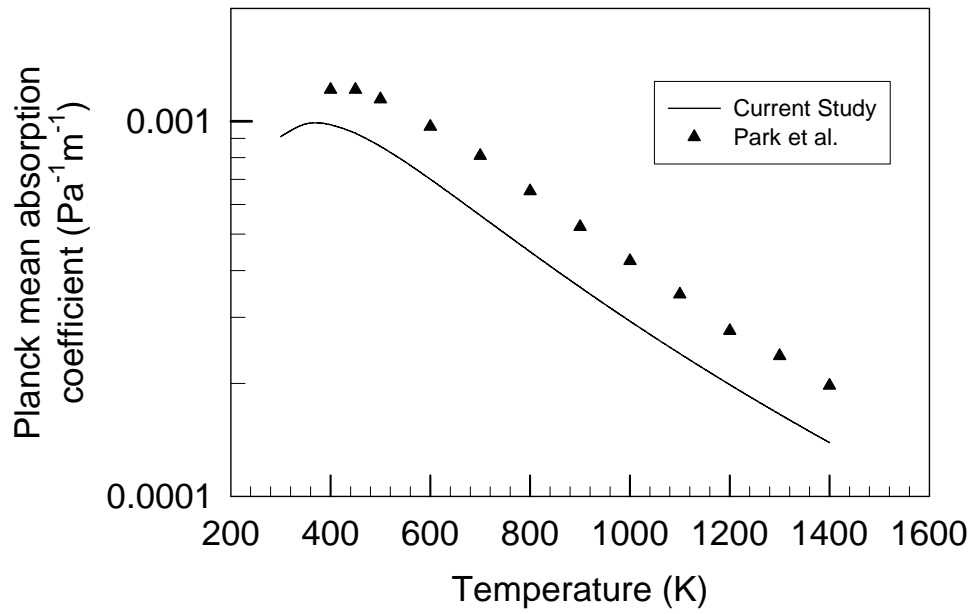
Figure 4-6: Comparison of Planck mean absorption coefficient for methyl methacrylate (MMA) with results from Park et al [14].

Table 4-4: Values for 4th order polynomial fits with equation 4 to Planck mean absorption coefficient data of other fuels.

	Methanol	Toluene	MMA
	300 K - 1400 K	300 K - 1400 K	300 K - 1400 K
a0	3.3374E-04	4.9459E-04	-5.7555E-05
a1	9.3528E-07	-1.2630E-06	7.2282E-06
a2	-3.0573E-09	1.8963E-09	-1.6559E-08
a3	2.6760E-12	-1.3674E-12	1.3318E-11
a4	-7.6382E-16	3.5996E-16	-3.6529E-15
R^2	9.9735E-01	9.9964E-01	9.9601E-01

4.4   Conclusion

Highly resolved infrared absorption coefficient database of fuels and combustion products (H_2O, CO_2, and CO from HITEMP database, and soot from modeling) were created. Planck mean absorption coefficients of measured fuels and methane absorption coefficients calculated from the HITRAN database were fitted to 4th order polynomial equations as a function of temperature and compared with each other. Large differences in the absolute values of the coefficients were obtained for the different hydrocarbon molecules. Based on this observation, it is clear that an accurate description of radiative transfer in fires will require temperature dependent absorption coefficients for all fuels. As the carbon number increases, similar trends in Planck mean absorption coefficients as a function of frequency were observed. However, at lower temperatures, propylene shows a large contribution for absorption and emission due to bending motion of the C=C bond and the associated =C-H bond. Other fuels such as toluene, methanol and methyl methacrylate, which contain characteristic band groups that absorb at low wavenumber as

well as propylene, had a large Planck mean absorption coefficient compared to hydrocarbons such as methane, propane, and heptane.

CHAPTER 5   THERMAL RADIATION FEEDBACK ANALYSIS AND CALCULATION

5.1   Introduction

Understanding of thermal radiation feedback using the new radiation absorption coefficient database described in the previous chapter is the final objective. Line of sight radiation transport analysis for methanol, heptane and toluene 0.3 m pool fires is conducted to understand the radiation contribution of combustion and fuel species within a fire. Radiation is dominant for energy feedback on fuel surface at fuel center. The one dimensional radiative transport equation along the flame centerline from the flame to fuel surface is introduced and the solution of the equation for pool fires for 0.3 m pool fires is presented.

5.2   Solution of 1D radiative transport equation (line of sight)

5.2.1   Transport equation

Radiation intensity change by attenuation per unit length is expressed as

$$\left(\frac{dI_v}{dz} \right)_a = -\kappa_v I_v \qquad (5.1)$$

where, I_v is spectral radiation intensity, κ_v is spectral absorption coefficient, and z is distance traveling the photons, subscript a is absorption, respectively.

Spectral radiation intensity change by emission per unit length is also expressed as

$$\left(\frac{dI_v}{dz}\right)_e = \kappa_v I_{b,v} \qquad (5.2)$$

where $I_{b,v}$ is radiation intensity by blackbody, and subscript e is emission. Combining eqn. (5.1) and (5.2) results in the general radiation transport equation,

$$\frac{dI_v}{dz} = -\kappa_v \left(I_v - I_{b,v}\right) \qquad (5.3)$$

where attenuation term is the first and emission term is the second of the right hand side.

For spectroscopy, the emission term originates from the self-emission of molecules, but is negligible unless the absorbing medium is of high concentration and at high temperature. Spectroscopy uses eqn. 5.1 to measure an absorption coefficient. This equation is referred to as "Beer's law". Beer's law assumes that the medium is at local thermodynamic equilibrium (LTE) and that there is no interaction between molecules.

When the photons travel from a position 0 to L within the medium having absorption coefficient κ, equation 5.1 becomes

$$I_v(L) = I_v(0)\exp(-\kappa_v L) \qquad (5.4)$$

$$\frac{I_v(L)}{I_v(0)} = \exp(-\kappa_v L) = T_v (\%) \qquad (5.5)$$

where $I_v(0)$ is spectral initial intensity, $I_v(L)$ is spectral intensity at L, and T_v is spectral transmittance, respectively. Physically, equations 5.4 and 5.5 indicate that spectral radiation intensity decays exponentially with length.

The radiative transport equation is integrated along the line of sight from 0 to s. The derivative of the radiative transport equation is given as

$$\frac{dI_v}{dz} = -\kappa_v \left(I_v - I_{b,v} \right) \qquad (5.5)$$

Optical depth τ is introduced as

$$d\tau_v = \kappa_v(z)dz \qquad (5.6)$$

$$\tau_v = \int_0^z \kappa_v dz \qquad (5.7)$$

Multiplying exp (τ) to both side of eqn. 5.5 yields

$$\exp(\tau_v)\frac{dIv}{d\tau v} + \exp(\tau_v)I_v(\tau) = I_{bv}(\tau_v)\exp(\tau_v) \qquad (5.8)$$

$$\frac{d}{d\tau}\left(\exp(\tau_v)I(\tau_v)\right) = I_{bv}(\tau_v)\exp(\tau_v) \qquad (5.9)$$

Integration of eqn. 5.9 from 0 to τ can be written as

$$\int_0^\tau d(\exp(\tau_v)I(\tau_v)) = \int_0^\tau I_{bv}(\tau_v *)\exp(\tau_v *)d\tau_v * \qquad (5.10)$$

$$I_v(\tau_v)\exp(\tau_v) - I_v(0) = \int_0^\tau I_{bv}(\tau_v *)\exp(\tau_v *)d\tau_v * \qquad (5.11)$$

$$I_v(\tau_v) = I_v(0)\exp(-\tau_v) + \exp(-\tau_v)\int_0^\tau I_{bv}(\tau_v *)\exp(\tau_v *)d\tau_v * \quad (5.12)$$

Since eqn. 5.12, a source function, cannot be solved directly, the trapezoidal rule is used to solve the transportation equation numerically.

$$I_v(\tau_v) = I_v(0)\exp(-\tau_v) + 0.5\tau_v \left[I_{bv}(\tau_v) + I_{bv}(0)\exp(-\tau_v) \right] \qquad (5.13)$$

Equation 5.13 was used to solve the radiation transport equation along the centerline of the fire from flame to fuel surface in the following section.

5.3   Radiation intensity at fuel surface by line of sight analysis

5.3.1   Data set and processing procedure

Species and temperature distribution data is necessary to analyze the radiation intensity along the flame centerline from flame to fuel surface. FDS (ver. 4.02) was used as a tool to model species and temperature information within pool fires for methanol, heptane, and toluene with 0.3 m diameter, which were then used to solve radiation

intensity at fuel surface. The grid sizes for each pool fire were 2 cm x 2 cm x 2 cm. Slice output files and the FDS utility (FDS2ASCII.EXE) were used to generate species and temperature distribution in the x and z directions, then the species and temperature data along the centerline of the fire were tabulated. The species and temperature table from the FDS and high-resolution absorption coefficients of species table were loaded into spectral radiation transport equation solver written in Matlab script, and radiation intensity at the pool surface was calculated. Radiation intensity normal onto the pool surface and contribution of species absorption were analyzed by gas-phase species absorption.

Two boundary conditions were set to solve the one dimensional transport equation. At first emission from species concentrations calculated by FDS at selected flame temperature was assumed for all fires and calculated the radiation intensity at the fuel surface defined as $I_{species}$. Second, blackbody emission at 1400 K for fuels with high degrees of sooting (heptane and toluene) was assumed and calculated the radiation intensity at the heptane and toluene pool surface defined as I_{BB}.

5.3.2   Methanol pool fire analysis

Figure 5-1 shows the solution of the spectral radiative transport equation along the fire centerline from the flame to fuel surface for a 0.3 m methanol pool fire. It should be mentioned that the grid is far too big to capture flame structure and thus it underpredicts the temperature rise in the flame zone. Therefore, flame temperature $T_f = 1400$ K, height 0.74 m of zero fuel mole fraction position from FDS calculation, and emission of H_2O, CO_2, and CO at flame were boundary condition. Since methanol produces little soot in its combustion, zero soot volume fraction was assumed in radiation calculation. Radiation intensity $I_{species}$, which is area under the curve in Figure 5-1, is 12,400 W/m^2-sr

at fuel surface, and this value is quite similar to Klassen's measurement (12,200 W/m^2-sr) [8]. Figure 5-2 shows the integrated radiation intensity by all species, the intensity by methanol, and the ratio of methanol to all species intensity as a function of height. As the height decreases, the contribution of methanol for radiation transport increases up to about 40% at the pool surface. Figure 5-3 shows radiation intensity, mole fraction of each species, and temperature as a function of height. From Figure 5-3, H_2O and CO_2 are seen to be major contributors to radiation transport near the flame, but the fuel mole fraction X_f increased above 0.3 (Z < 5 cm from the fuel surface). Thus, in this region fuel became the major contributor to radiative absorption. The mole fraction of CO is very low (ppm level) compared to Hamins' experiment (3 %) [76], but the contribution of CO on total radiation intensity is very small since the total number of carbon doesn't change at all and the carbon is shared by CO and CO_2. Radiation intensity gains from the flame to 10 cm above the fuel surface (emission > absorption), then slightly decreases toward the fuel surface (absorption > emission). The temperature along the flame centerline is very high ranging from 900 K to 1400 K. Since radiation absorption at high temperature becomes small and emission becomes larger, the temperature profile also supports the radiation intensity profile. Figure 5-4 shows the spectral radiation intensity of C-H stretching of methanol about 3.4 μm (3000 cm^{-1}) as a function of height. From the spectral intensity, methanol emission is stronger than absorption from flame to 6 cm above fuel surface, then absorption is more significant than emission toward to fuel surface. Since the radiation transport equation calculates both absorption and emission, this result shows that emission by methanol is higher than absorption almost within the methanol fire, and absorption is only higher than emission near the fuel surface. Figure

5-5 shows comparison of radiation intensity of 0.3 m methanol pool fire calculated by temperature dependent and independent (ambient temperature) methanol and temperature dependent methane absorption coefficients. Since calculation only changes fuel absorption coefficient, difference in radiation intensity is due to fuel absorption. Ambient absorption coefficient as an alternative absorption coefficient for all temperatures was set to see if temperature dependent absorption coefficient has significant impact on the radiation calculation. As the comparison of effect on the fuel species, radiation intensity at methanol fuel surface calculated the transport equation using methanol absorption coefficient is higher than the intensity by methane (error +17%). This is because emission by methanol is higher than methane at high temperature. Intensity decay (dI/dz < 0) near the fuel surface also shows methanol absorbs more radiation than methane. Since methanol has higher absorption coefficient relative to methane. As a comparison of temperature dependency of methanol absorption coefficient on radiation intensity, the radiation intensity during emission has maximum +17% error, but the error decreased toward to fuel surface and finally – 3% at fuel surface. The position, where the sign of dI/dz changed from + to -, shifted higher if the temperature independent (ambient) methanol absorption coefficient was set. Although there was an effect temperature dependency of absorption coefficient while a molecule was emitting and absorbing, there was small impact on radiation intensity at fuel surface.
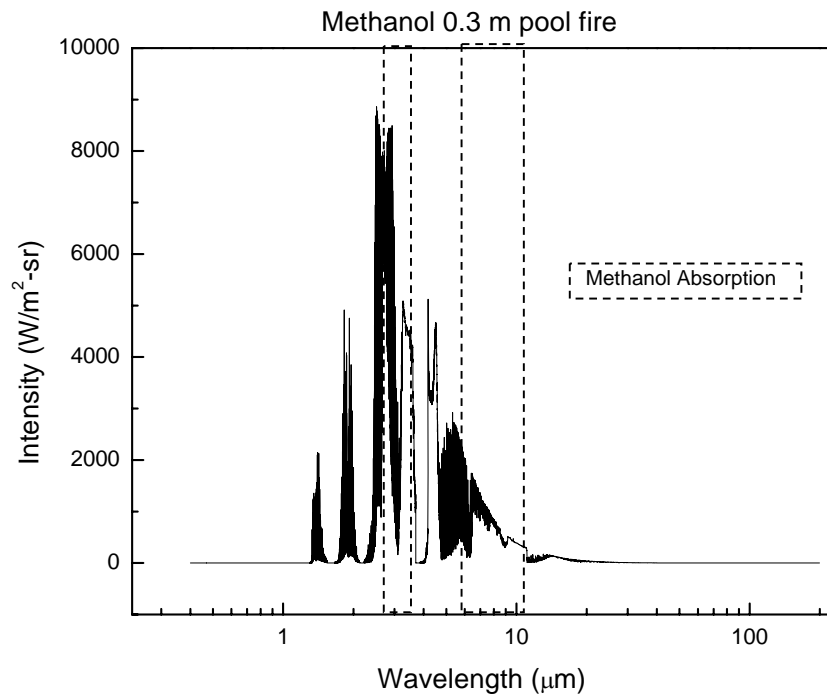
Figure 5-1: Spectral directional radiation intensity along the flame centerline from flame to fuel surface for 0.3 m methanol pool fire.
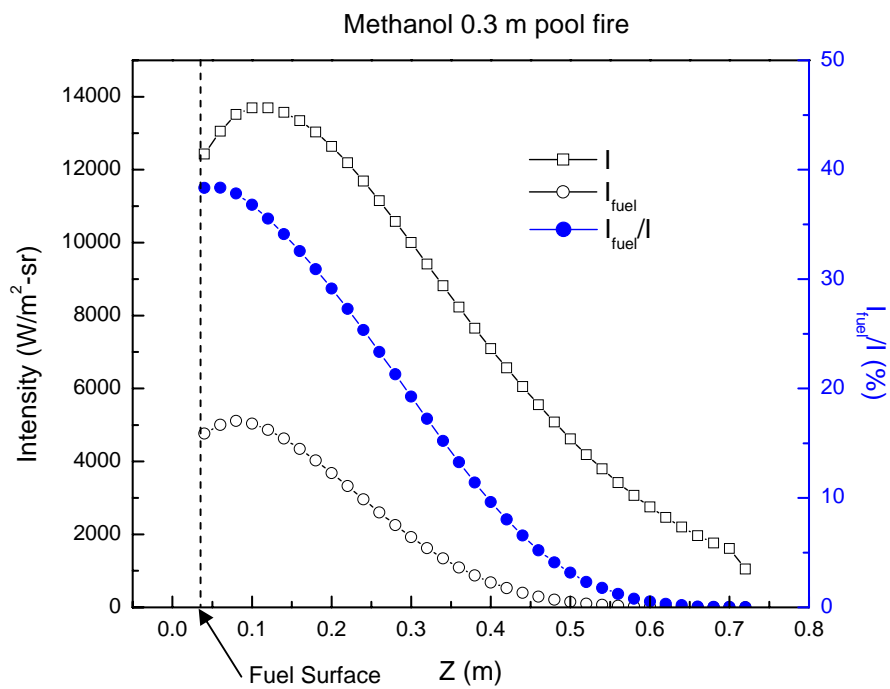
Figure 5-2: Integrated directional radiation intensity by all species and methanol, and the ratio of methanol to all species intensity as a function of height for 0.3 m methanol pool fire.
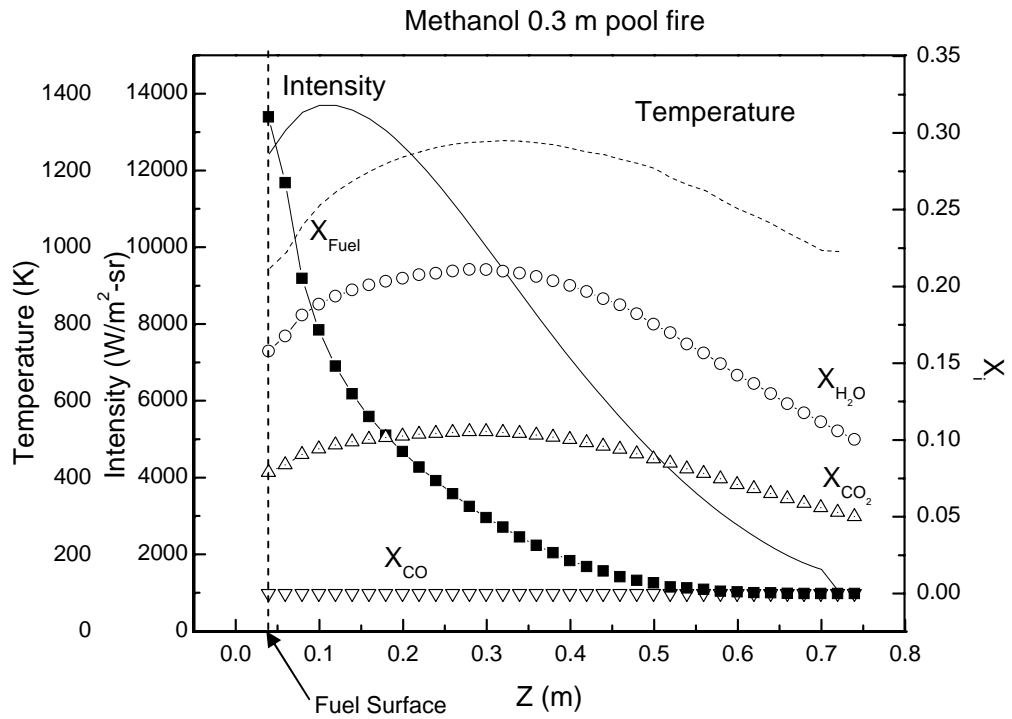
Figure 5-3: Integrated directional radiation intensity, mole fraction of each species (X_i), and temperature as a function of height for 0.3 m methanol pool fire.
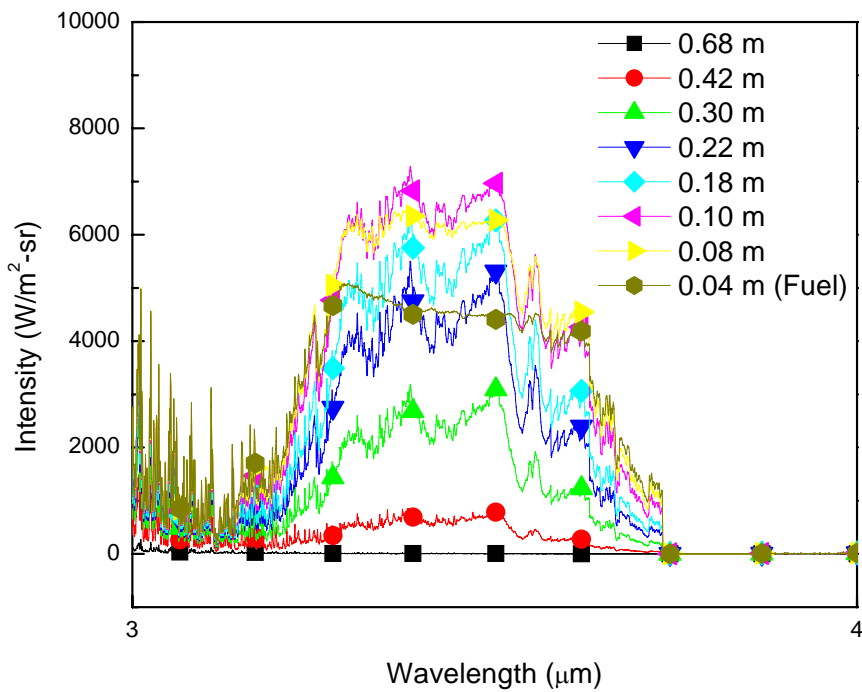
Figure 5-4: Spectral radiation intensity of C-H stretching of methanol about 3.4 mm (3000 cm^{-1}) as a function of height
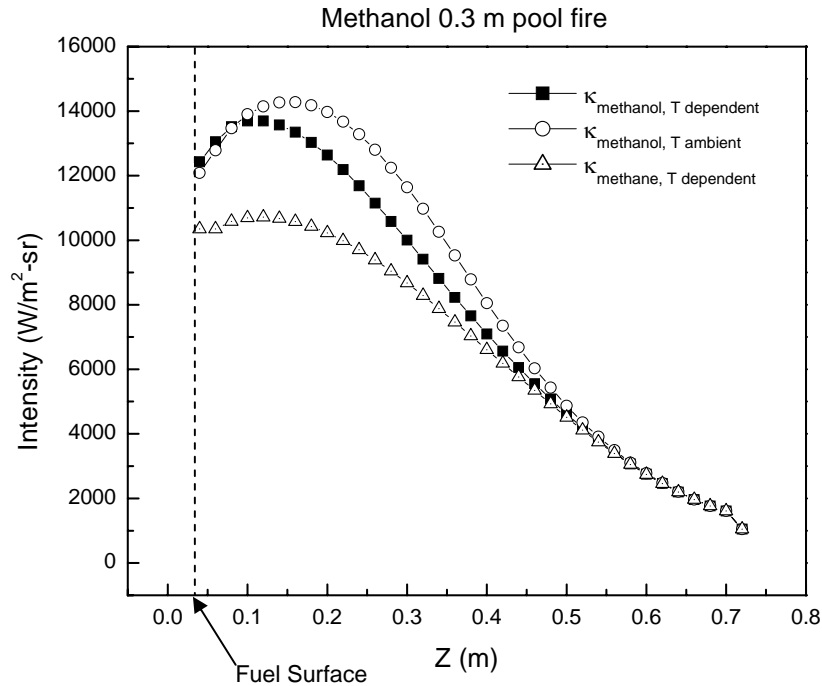
Figure 5-5: Comparison of radiation intensity of 0.3 m methanol pool fire calculated by temperature dependent and independent methanol absorption coefficient and temperature dependent methane absorption coefficient.

5.3.3 Heptane pool fire analysis

Figure 5-6 shows the solution of the spectral radiative transport equation along the fire centerline from the flame to fuel surface for a 0.3 m heptane pool fire. The grid is far too big to capture flame structure and thus it underpredicts the temperature rise in the flame zone. Emission of soot, H_2O, CO_2, and CO from a flame temperature $T_f = 1400$ K at a height 0.86 m, the highest temperature position in a flame region from FDS calculation, was the boundary condition. Radiation intensity $I_{species}$, the area under the curve at the fuel surface, was 3,500 W/m^2-sr. The spectrum result was qualitatively good, but the integrated intensity was very low relative to Klassen's measurement (23,500 W/m^2-sr) [8]. Figure 5-7 shows comparison of the integrated directional radiation intensities by all species and heptane, and the ratio of heptane to all species intensity as a

116

function of height for 0.3 m heptane pool fire. Average radiation contribution of heptane is about 20% entire heptane fire, but slightly decreased about 13 % at fuel surface.

In reality, the moderate sooty heptane flame is optically thick and emission is assumed as the blackbody emission. In order to compare previous results of weak species emission to blackbody radiation, the boundary condition to solve transport equation was changed to blackbody emission at 1400 K, and the transport equation was recalculated. Figure 5-8 shows the result of 1400 K blackbody emission as an alternative boundary condition. Total directional radiation intensity I_{BB}, the area under the curve for each flame sheet and fuel surface, at a flame position was 69,300 W/m^2-sr and 25,700 W/m^2-sr at fuel surface. This result was very close to Klassen's measurement (23,500 W/m^2-sr). This result implies that species emissions from the flame were likely issuing from much higher temperatures than predicted by the FDS simulation and that the temperature was not far from 1400 K. As stated earlier, the underprediction of flame temperatures by FDS is expected because it fails to resolve flame structure properly. From Figure 5-8, combustion products (H_2O, CO_2, CO, and soot) and heptane attenuated about 60 % of flame radiation, 43,600 W/m^2-sr, during radiation attenuation from flame to fuel surface. Heptane absorption was approximately 5,800 W/m^2-sr, and occupied about 13 % of total energy absorption. Soot was the most absorbed specie with 27,000 W/m^2-sr, and occupied about 62 % of total absorption. Other specie (H_2O, CO_2, and CO) were 10,800 W/m^2-sr and 25 % of total absorption.

Temperatures within the heptane fire decreased toward the fuel surface, and the temperature within the entire flame was lower than with methanol shown in Figure 5-9. Also the temperature near the heptane fuel surface was much lower (about 450 K) than

methanol fire (about 900 K), and the slope of radiation intensity (dI/dz) was negative. Therefore, the contribution of radiation absorption was larger than that of emission for radiation transfer process in a heptane fire. The difference of radiation intensity by heptane and methane absorption is also compared in Figure 5-10. As for methanol, the difference of radiation intensity was due to these two fuels absorption coefficient. For species emission boundary condition, radiation intensity by heptane was higher than methane due to more emission by heptane molecules, but the difference decreased toward the fuel surface and finally the intensity became lower than for methane (error – 8%). For 1400 K blackbody boundary condition, radiation intensity by heptane was always lower than methane (error -9 %). This difference of radiation characteristic is due to the boundary radiation source intensity. For comparison of radiation intensity calculated by temperature dependent and ambient absorption coefficient as an alternative of all temperature absorption coefficients, the radiation intensity by temperature dependent absorption coefficient was 6 % lower value than the ambient absorption coefficient. Figure 5-11 shows the comparison spectral radiation intensity of C-H stretching peak about 3.4 μm (3000 cm^{-1}) at the pool surface between heptane and methane absorption coefficient. Since heptane has a higher absorption coefficient than methane due to the increased number of C-H bonds, the radiation intensity with the heptane coefficient was lower than that of methane.

Heptane 0.3 m pool fire
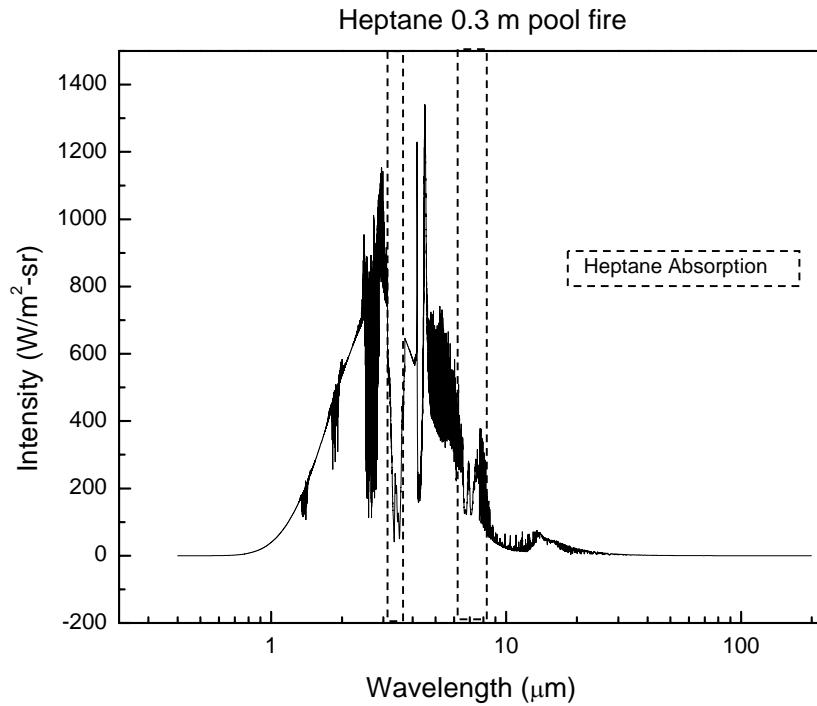
Figure 5-6: Spectral directional radiation intensity along the flame centerline from flame to fuel surface for 0.3 m heptane pool fire.

Heptane 0.3 m pool fire

Figure 5-7: Integrated directional radiation intensity by all species and heptane, and the ratio of heptane to all species intensity as a function of height for 0.3 m heptane pool fire.

Heptane 0.3 m T_f = 1400 K
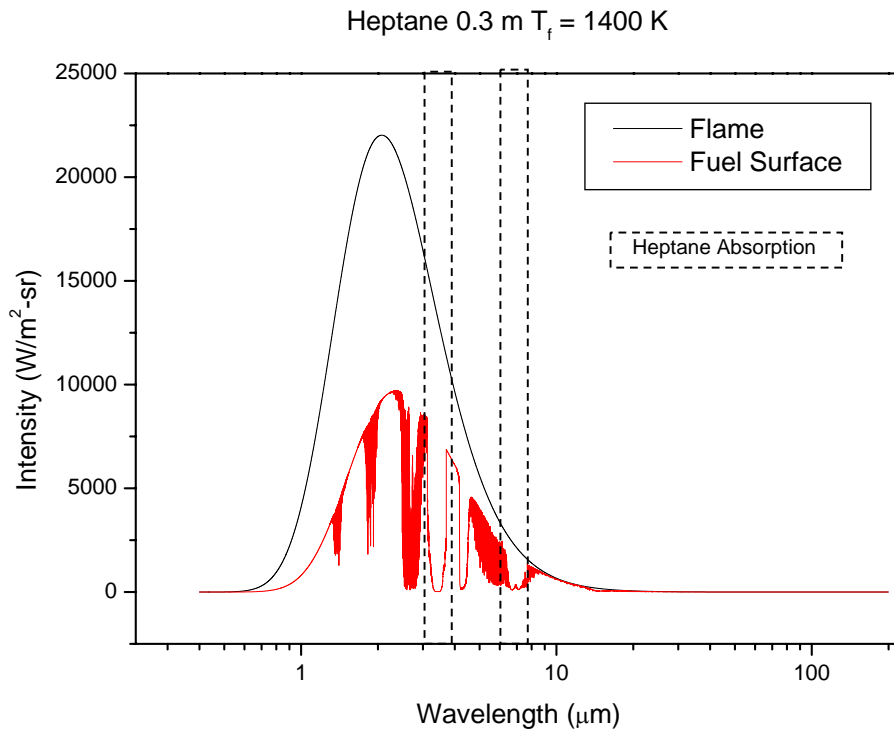
Figure 5-8: Spectral directional radiation intensity along the flame centerline from flame to fuel surface for 0.3 m heptane pool fire with blackbody intensity as an initial condition.
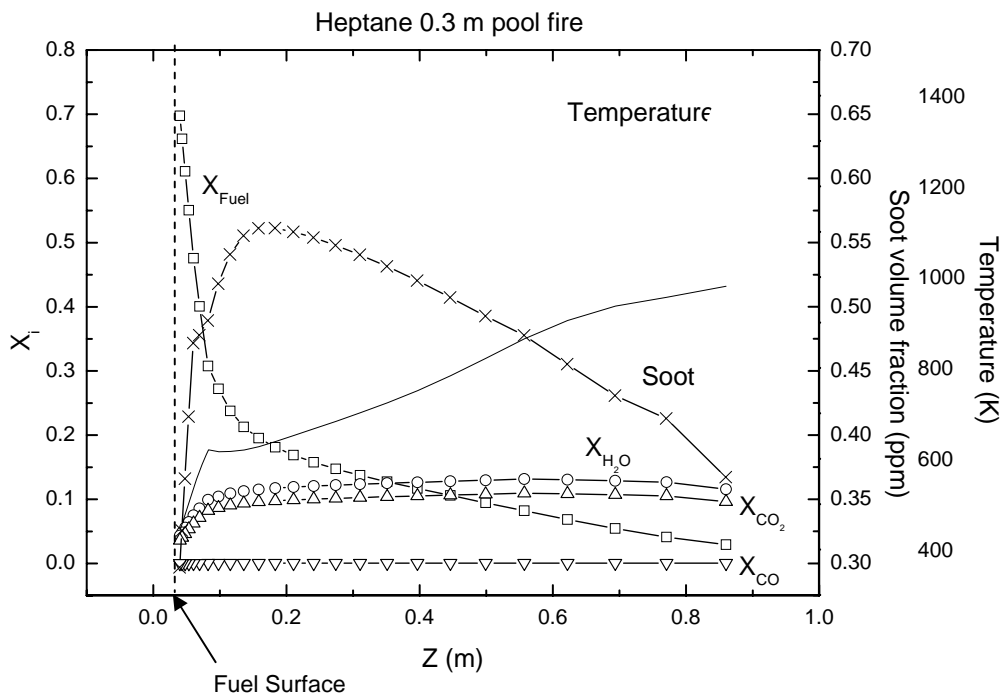
Figure 5-9: Mole fraction of species (X_i) and soot volume fraction (ppm), and temperature as a function of flame height for 0.3 m heptane pool fire.
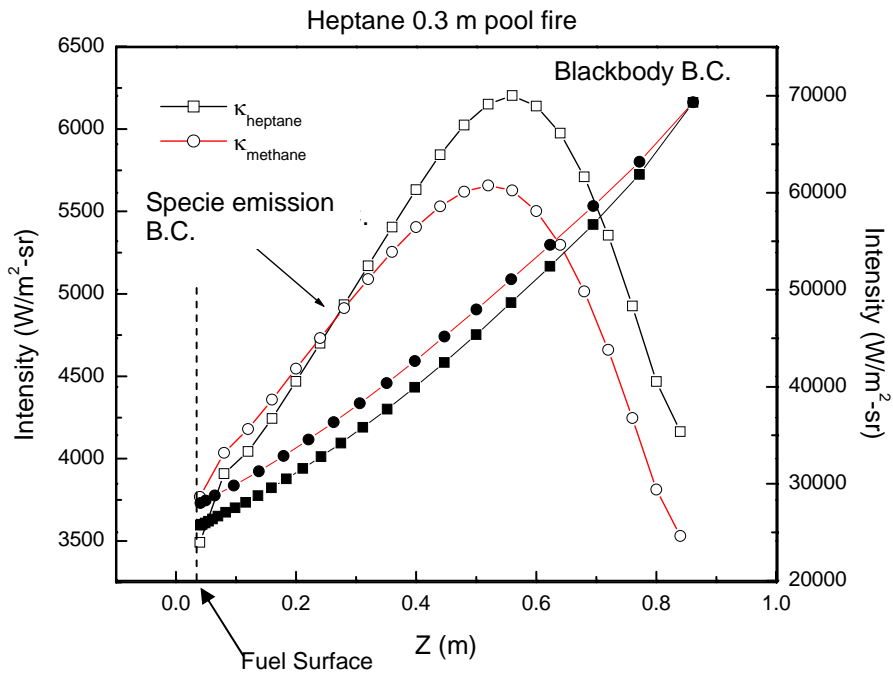
Figure 5-10: Comparison of radiation intensity of 0.3 m heptane pool fire calculated by heptane and methane absorption coefficients, and by species and blackbody emission at 1400 K as boundary conditions.
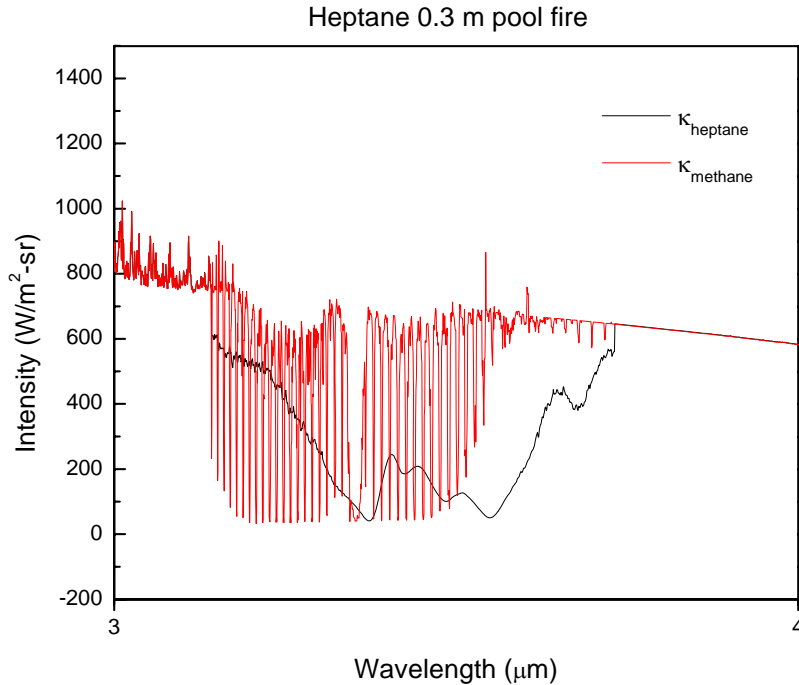
Figure 5-11: Comparison of spectral radiation intensity of C-H stretching peak about 3.4 μm (3000 cm^{-1}) at heptane pool surface between heptane and methane absorption coefficient (Specie emission boundary condition).

5.3.4   Toluene pool fire analysis

Since toluene pool fires are sootier than heptane fires, the radiation intensity calculation of toluene was more difficult than previous heptane analysis. Figure 5-12 shows the solution of the spectral radiative transport equation along the fire centerline from the flame to fuel surface for a 0.3 m toluene pool fire. As for methanol and heptane fire analysis, emission of soot, H_2O, CO_2, and CO of flame temperature T_f = 1400 K at height 0.86 m of the highest temperature position in a flame region from FDS calculation, was the first boundary condition.   Radiation intensity at the fuel surface $I_{species}$, which is area under the curve in Figure 5-12, was 4,100 W/m^2-sr.   Figure 5-13 shows a comparison o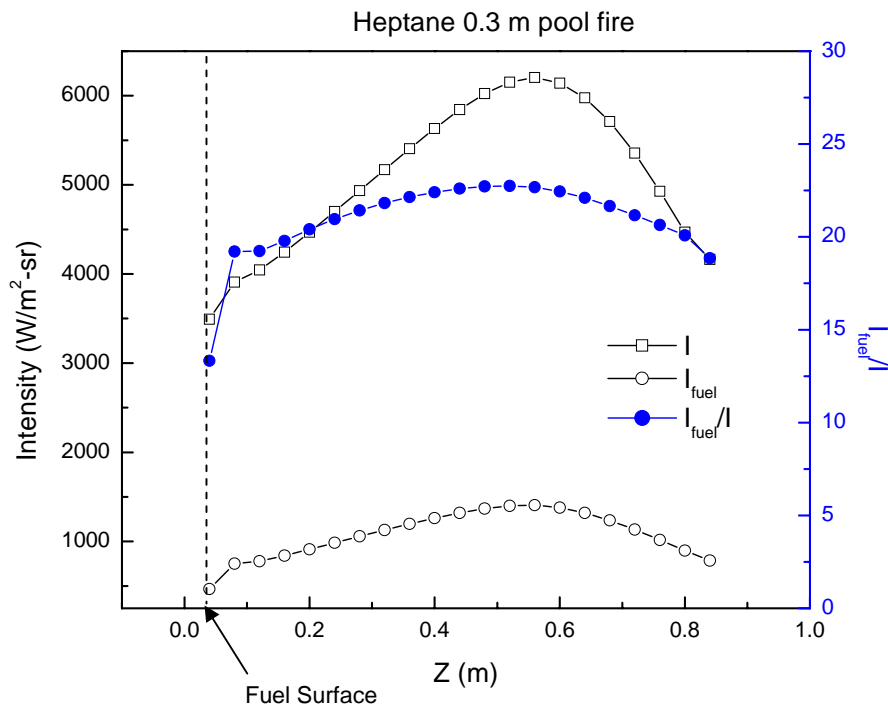f integrated directional radiation intensities by all species and toluene, and the ratio of toluene to all species intensity as a function of height for 0.3 m toluene pool fire, when species emission at 1400 K was set as a second boundary condition. The radiation contribution of toluene increased toward the fuel surface up to 40 %. Combustion products (mainly soot) absorbed the radiation. Figure 5-14 shows the mole fraction of each species and soot volume fraction (ppm), and temperature as a function of height. Compared to heptane analysis, toluene had 5.6 times higher soot volume fraction. Since soot strongly absorbed radiation in the toluene fire, water vapor and carbon dioxide were minor contribution relative to soot on radiation transport. Although fuel absorption dramatically increased from 0.05 m above the fuel surface and reached a maximum near the fuel surface, contribution of fuel on radiation transport was small relative to soot. Figure 5-15 shows the difference of radiation intensity calculated by temperature

dependent and independent (ambient temperature) toluene and temperature dependent methane absorption. As for methanol and heptane, the difference of radiation intensity was also due to these two fuels absorption coefficient. The difference decreased toward the fuel surface, and finally the intensity became lower than for methane. Figure 5-16 shows the comparison spectral radiation intensity from 3 to 11 μm at the pool surface by heptane and methane absorption coefficient. Since toluene has more bands coefficient than methane, the radiation intensity at pool surface by toluene absorption coefficient was lower than that of methane. Radiation intensity by toluene was slightly higher than methane, but total radiation intensity at fuel surface was not so different. The little effect of temperature dependency absorption coefficient on radiation intensity could be seen in the same figure. Temperature within the toluene fire dropped near the fuel surface, and the temperature within the entire flame was lower than methanol as well as heptane. This could be due to mainly soot absorption. The temperature near fuel surface was much lower (about 490 K) than methanol fire (about 900 K) as well as heptane.

Blackbody radiation at 1400 K as an alternative boundary condition was set and recalculated as well as heptane fire, in order to compare the result of previous boundary condition. Radiation intensity I_{BB}, which is the area under the curve for each flame and fuel surface shown in Figure 5-17, was 69,300 W/m^2-sr at the flame position and 6,400 W/m^2-sr at the fuel surface. This value was still lower than Klassen's measurement (20,200 W/m^2-sr). Combustion products (H_2O, CO_2, CO, and soot) and toluene absorbed about 91% of flame radiation, 63,000 W/m^2-sr, as a result of radiation attenuation from the flame to fuel surface. Soot was the most absorbed specie with 58,400 W/m^2-sr, and

occupied about 93% of total absorption. Combustion products (H_2O, CO_2, and CO) and toluene were 2% and 5% of total absorption, respectively.

Although the highest temperature position in the flame along the flame centerline, and accurate absorption coefficients for all species were set, solution of the radiation transport equation of line of sight was underestimated at the toluene pool surface. Although the radiation intensity of methanol pool fire was predicted well relative to experimental result, the result of heptane and toluene were not. Most of the radiation for moderate sooty and heavy soot fires (heptane and toluene fires) was attenuated before the intensity reached to the fuel surface. In order to obtain more radiation at fuel surface, the emission intensity must be stronger (a higher flame temperature), or the position of the emission source within the pool fire could be lower.

Since radiation transport of sooty fires depends on soot concentration, the location of emission origin of heptane might be higher than toluene. If the radiation transport equation is solved reversibly from fuel surface with fuel radiation intensity as an initial condition until the intensity goes to maximum, the emission source (say virtual emission source) can be determined. More details of the radiation transport mechanism within the fire can be obtained if accurate species and temperature distribution are used.

Figure 5-12: Spectral directional radiation intensity along the flame centerline from flame to fuel surface for 0.3 m toluene pool fire.

Figure 5-13: Integrated directional radiation intensity by all species and toluene, and the ratio of toluene to all species intensity as a function of height for 0.3 m toluene pool fire.
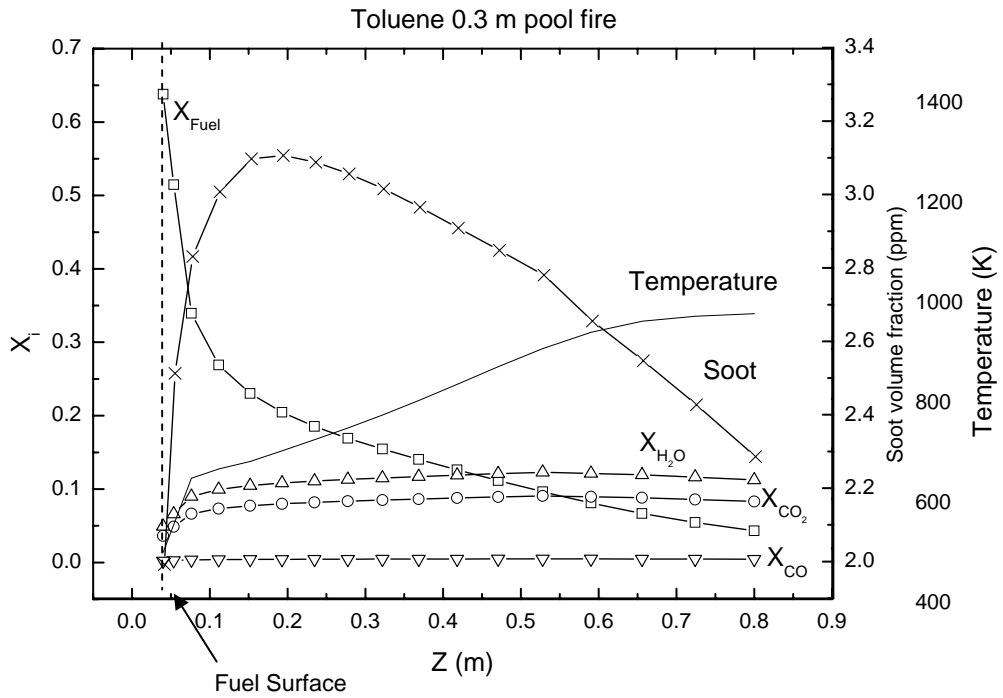
Figure 5-14: Mole fraction of species (X_i) and soot volume fraction (ppm), and temperature as a function of flame height for 0.3 m toluene pool fire.
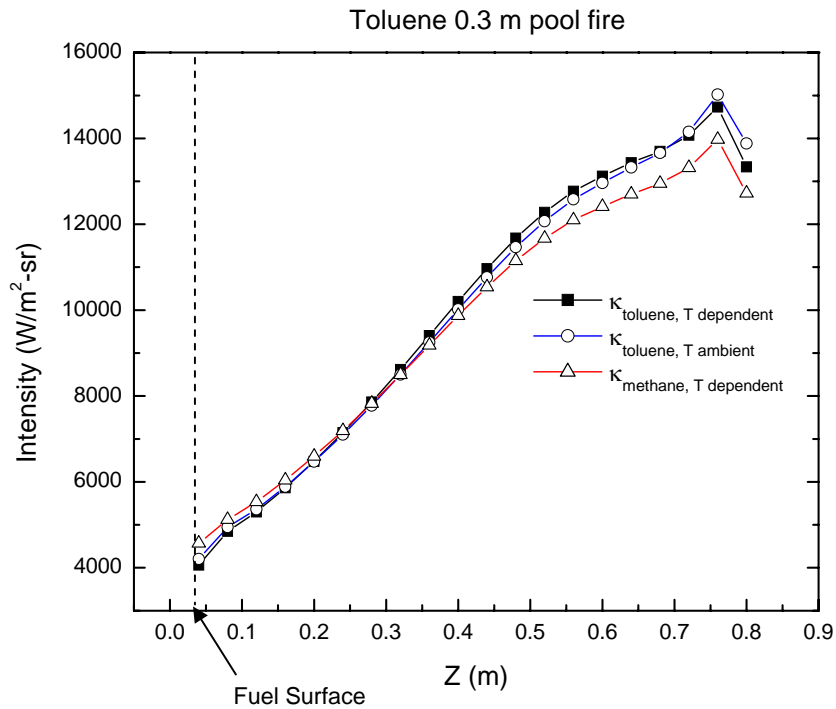
Figure 5-15: Comparison of radiation intensity of 0.3 m toluene pool fire calculated by toluene and methane absorption coefficients, and by specie emission as a boundary condition.
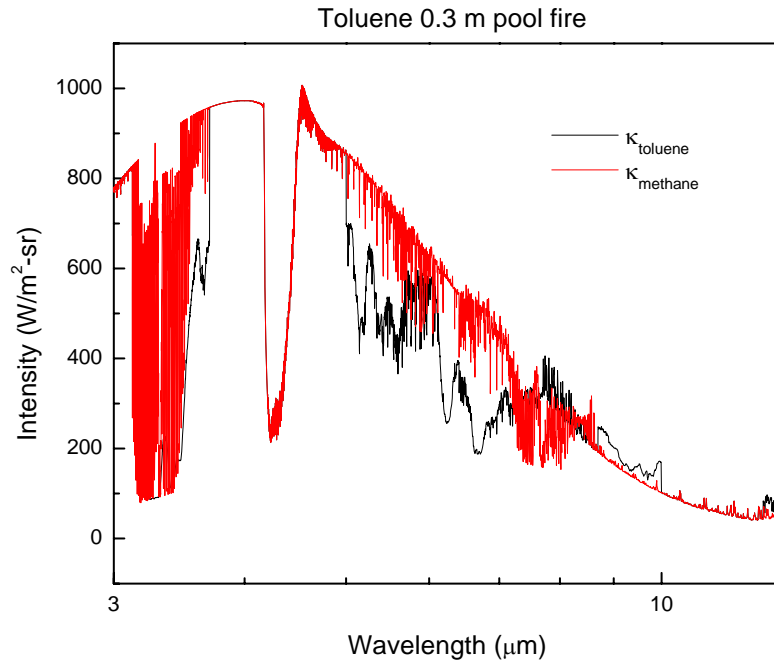
Figure 5-16: Comparison of spectral radiation intensity from 3 to 11 µm at toluene pool surface by toluene and methane absorption coefficient.
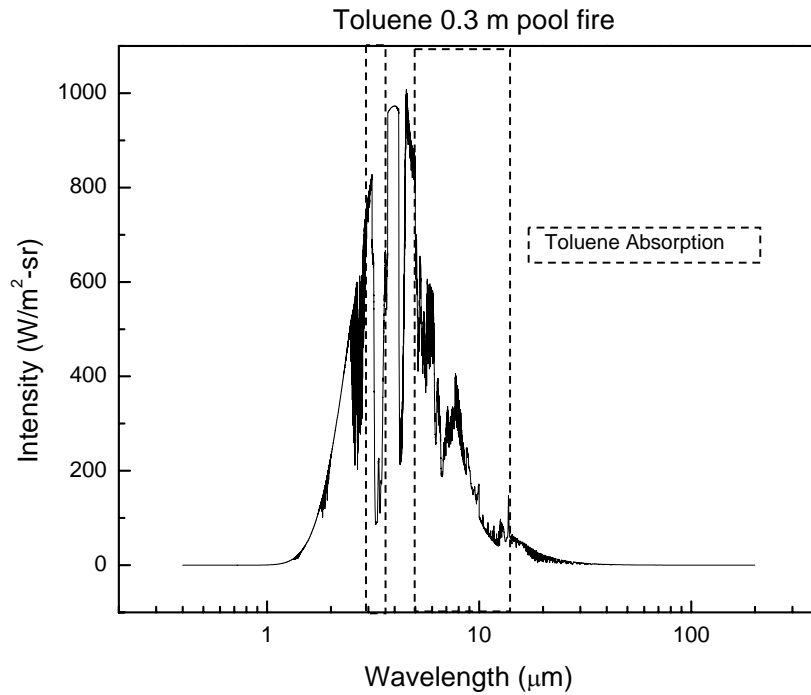

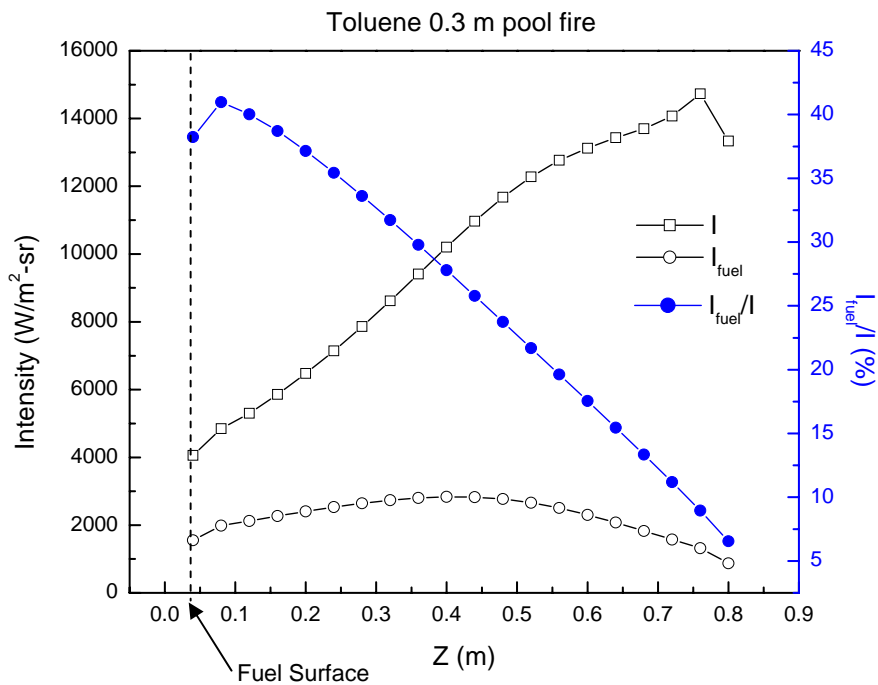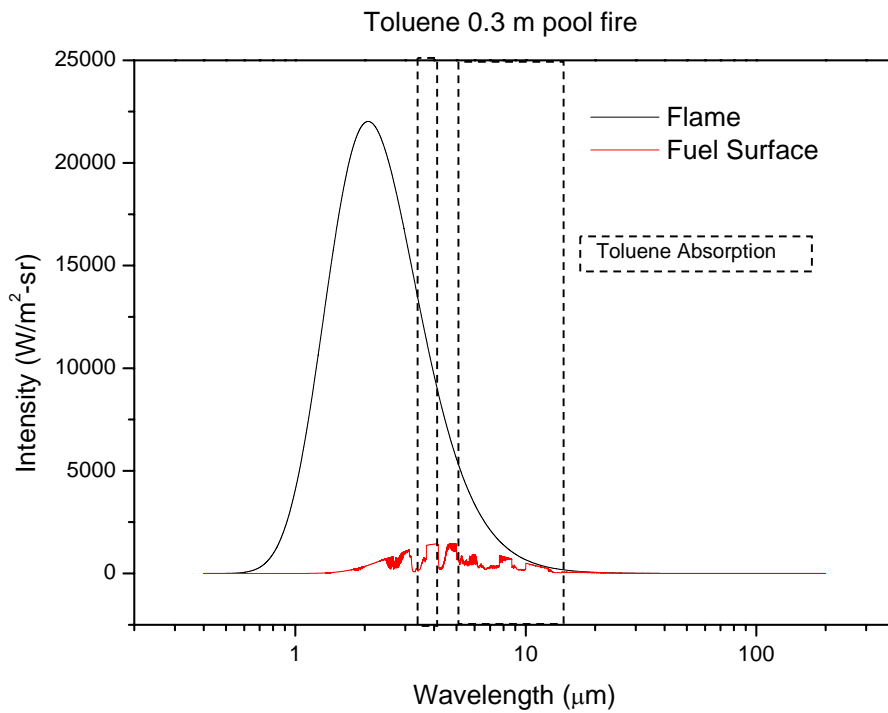Figure 5-17: Spectral directional radiation intensity along the flame centerline from flame to fuel surface for 0.3 m toluene pool fire with blackbody boundary condition.

5.3.5   Radiation transport between gas phase and condensed phase

Spectral directional radiative intensity at the fuel surface for each fuel pool fire shows that the characteristic band region for each fuel is very small relative to the entire infrared region.   Since the fuel molecule can only absorb the radiation at the characteristic wavelength, the radiation at other bands is transmitted. Figure 5-18 through Figure 5-20 show the condensed and gas phase infrared spectrum for methanol, heptane, and toluene, respectively. From these figures, condensed phase spectra are broad and many additional peaks due to association and dense population of the molecules are seen. Once the radiation by gas phase strikes the fuel surface, the absorption characteristic of fuel molecule changes to a condensed phase one. Therefore, a wider range of radiation can be absorbed by condensed fuel. Also, combustion products effect should be considered at the phase interface. For methanol, water vapor can be associated with methanol molecule. Since temperature on the interface of methanol can be assumed as methanol boiling point, water condensation is considered. Therefore, liquid water and liquid methanol absorption should be considered for radiation transport within the condensed phase. For heptane and toluene, it can be assumed that large concentrations of soot floating on the fuel surface absorbs radiation in addition to condensed fuel absorption, as a result of soot distribution within heptane and toluene pool fires. Hamins [77] observed much soot on the pool surface and a black liquid color after the heptane and toluene experiments. Condensed water is minor effect relative to soot absorption.
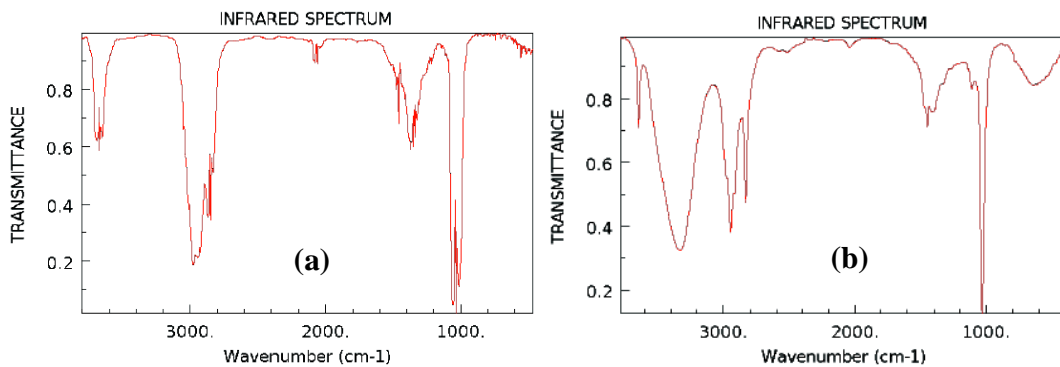
Figure 5-18: Transmissivity of methanol infrared spectrum; (a) gas phase and (b) condensed phase from NIST Webbook [58].
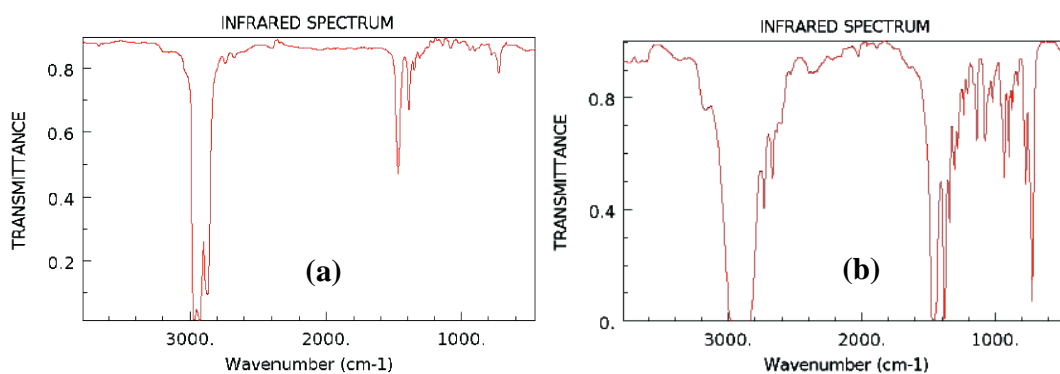
Figure 5-19: Transmissivity of heptane infrared spectrum; (a) gas phase and (b) condensed phase from NIST Webbook [58].
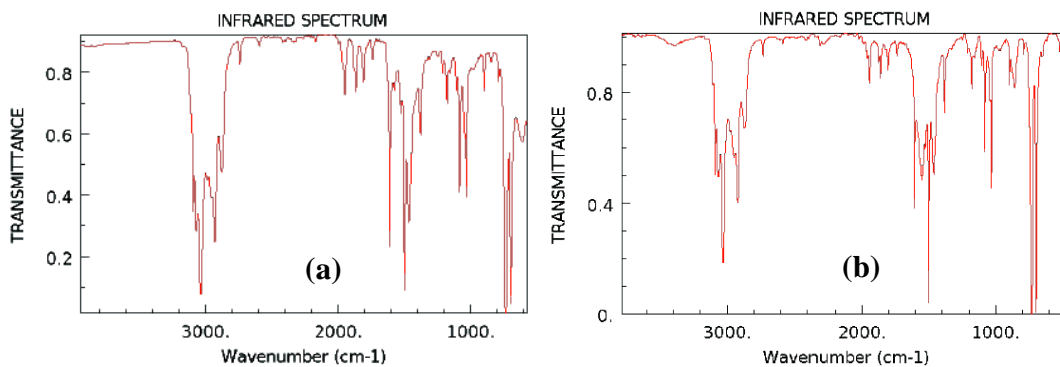
Figure 5-20: Transmissivity of toluene infrared spectrum; (a) gas phase and (b) condensed phase from NIST Webbook [58].

5.4   Conclusion

The radiation intensity at the pool surface of 0.3 m methanol, heptane, and toluene pool fire was calculated using one dimensional radiative transport equation with species concentration and temperature profile calculated by FDS.   Emission of combustion species was set as a boundary condition to solve the transport equation for all pool fires. Solution of methanol pool fire had small error (2%) relative to previous experimental data, but heptane and toluene errors were large (> 100%). When the blackbody emission at 1400 K was set as an alternative initial condition of heptane and toluene fire because of the optically thick flame, heptane agreed well with previous experimental data, but toluene did not. From this analysis, the radiation intensity of methanol fire can be solved by optically thin condition, and heptane can be solved using an optically thick blackbody boundary condition. If the radiation intensity at the toluene fuel surface is assumed from previous experiment by Klassen, emission sources within the fire could be closer to fuel surface or the boundary intensity could be stronger since soot absorbed much of the radiation energy. Toluene fire needs more careful investigation since soot absorption and emission completely controls radiation heat transfer within the toluene fire relative to methanol and heptane. Since the grid is far too big for FDS to capture flame structure, underprediction of temperature rise in the flame zone led low radiation intensity at fuel surface for heptane and toluene.

The effect of change of fuel absorption coefficient from each fuel to methane on the radiation intensity at fuel surface was analyzed and average 20 % for all fuels was observed.   Use of the correct fuel absorption coefficient significantly impacted the radiation intensity. The effect of temperature dependency absorption coefficient on the

radiation intensity at the fuel surface was also investigated by comparison between temperature dependent absorption coefficient and ambient absorption coefficient as an alternative for all temperature coefficients. The average impact for all pool fires was 4 %. Although differences between radiation intensity due to temperature dependency on absorption coefficient within the characteristic bands of each fuel were large, the difference was small impact on the total intensity at entire infrared region. The pool fires with cool fuel rich core don't receive the impact of temperature dependency, since radiation absorption of fuel is conducted within the fuel core. This analysis is only for small-scale (0.3 m diameter) fire, but medium scale (~1m) and large scale (~20 m) cases should be investigated since the flame structure changes.

CHAPTER 6   CONCLUSION

6.1   Summary of Results

An experimental apparatus was developed to obtain infrared measurements at high temperature. This unique instrument with a nitrogen jet window cooling unit protected the ZnSe window from oxidation and thermal degradation and allowed good spectral transmissivity for long running times at high temperature. Cooling effects on the infrared window were evaluated by temperature measurement inside and outside of the windows by thermocouples, and cooling velocity on the window was determined. Gas fuels and vaporized liquid fuels, and nitrogen mixture were supplied by two mass flow controllers, one for fuel delivery and the other for fuel dilution, and supplied continuously to optical cell.

Propane, heptane, methanol, toluene, propylene and methyl methacrylate (MMA) infrared absorption coefficients were obtained at five temperatures from 300 K to 1000 K. As temperature increased, absorption coefficients for each fuel decreased around the band peaks and became noisy since lower vibrational states become less probable with higher temperatures and the spectrum featured vibrational and rotational energy transition at higher energy levels. At the band wings, absorption coefficient increased due to shifted and broadened rotational transition. Simplified extrapolation techniques for absorption coefficients were developed and its capability was evaluated by HITEMP database and experimental data (propane). Fuel pyrolysis at high temperature was investigated by CHEMKIN AURORA, and the possibility of fuel pyrolysis during high temperature infrared measurement was evaluated. All fuels except heptane were not expected to have

fuel pyrolysis at 1000 K. The extrapolation technique was verified to give great contribution to obtain an infrared spectrum at high temperature, up to 1000 K.

A high-resolution infrared absorption coefficient database of fuels and combustion products (H_2O, CO_2, and CO from HITEMP database, and soot from modeling) was created. Planck mean absorption coefficients of measured fuels and methane absorption coefficients calculated from the HITRAN database were fitted to 4th order polynomial equations as a function of temperature and compared with each other. Based on the characteristics of Planck mean absorption coefficient, it was clear that an accurate description of radiative transfer in fires requires temperature dependent absorption coefficients for all fuels. Hydrocarbon (alkanes) had similar trends in Planck mean absorption coefficients, but propylene (alkenes) showed a large contribution for absorption and emission at lower temperatures due to the bending motion of the C=C bond and the associated =C-H bond. Other fuels such as toluene, methanol, and methyl methacrylate, which contain characteristic band groups that absorb at low wavenumber as well as propylene, had a large Planck mean absorption coefficient compared to hydrocarbons (alkanes).

Radiation intensity at the fuel surface of 0.3 m methanol, heptane, and toluene pool fires was investigated using one dimensional radiative transport equation with species concentration and temperature profile obtained by FDS. The grid for FDS was far too big to capture flame structure and thus it underpredicts the temperature rise in the flame zone for all pool fires. Emission of combustion species of flame temperature at 1400 K was set as a boundary condition, and the transport equation for all pool fires was solved. Methanol pool fires had good agreement with previous experimental data, but heptane

and toluene didn't when emission by species was set as the boundary condition. When blackbody emission at 1400 K was set as an alternative boundary condition of heptane and toluene fire because of their optically thick flame, heptane yielded good agreement with previous experimental data, but toluene did not. As a result, radiation intensity of methanol fire can be solved by optically thin condition with species emission and heptane can be by optically thick blackbody condition. From the analysis of heptane and toluene, emission source within the fire could be stronger or source position could be closer to fuel surface since soot absorbed much radiation. Toluene fires need to be further investigated since soot absorption and emission completely dominates radiation heat transfer within the toluene fire relative to methanol and heptane. Underprediction of the temperature rise in the flame zone resulted in low radiation intensity. Using the exact fuel absorption coefficient has a significant impact on radiation intensity at the fuel surface, but temperature dependency on the absorption coefficient is small since the discrete characteristic band range for fuel is much smaller than the entire infrared region absorption by soot.

6.2   Recommendation for Further Research

This dissertation only focused on the radiation heat transfer in the gas phase. However, radiation heat transfer of the condensed phase cannot be ignored since a fuel can only absorb radiation at fuel's several characteristic band groups. An infrared spectrum in the condensed phase is also broadened and more absorption can be considered relative to gas phase spectrum due to the huge population and association of molecules. Moreover, condensed combustion products such as water and soot near or floating on the fuel surface can also affect the infrared absorption. These additional

134

conditions should be included to understand more deeply the radiation absorption at fuel surface. Radiation absorption coefficient measurement of condensed phase fuel should be the first step to understand radiation transport at interface between gas and condensed phase. The absorption coefficient database in this thesis will be incorporated into current FDS and will make significant improvement of fuel burning rate calculation including accurate prediction of radiation feedback on fuel surface. Additional fuel information such as acetylene, ethylene, gasoline and LNG will be conducted by the unique FTIR and expand fuel database in the FDS. This future work is necessary to expand energy feedback study to control practical large scale fire such as an oil tank fire.

Reference

1. Burgess, D., and Hertzberg, M., *Radiation From Pool Flames*, in *Heat Transfer in Flames*, N.H. Afgan, and Bear, J. M., Editor. 1974, John Wiley: New York. p. 413-430.

2. Hamins, A., Fischer, S. J., Kashiwagi, T., Klassen, M. E., Gore, J. P., *Heat Feedback to the Fuel Surface in Pool Fires.* Combust Sci Technol, 1994. **97**(1-3): p. 37-62.

3. Buckius, R.O., Tien, C. L., *Infrared Flame Radiation.* Int J Heat Mass Tran, 1977. **20**(2): p. 93-106.

4. Ludwig, C.B., Malkmus, W., Reardon, J. E., and Thomson J. A. L., *Handbook Of Inrared Radiatioin From Combustion Gases*. 1973, National Aeronautics and Space Administration (NASA): Washingon, D.C.

5. Lee, S.C., and Tien, C. L., *Optical Constants of Soot in Hydrocarbon Flames.* Eighteenth Symposium (International) on Combustion/The Combustion Institute, 1980: p. 1159-1166.

6. Rothman, L.S., Camy-Peyret, C., Flaud, J-M., Gamache, R., Goldman, A., Goorvitch, D., Hawkins, R., Schroeder, J., Selby, J., Wattson, R., *HITEMP, the High-Temperature Molecular Spectroscopic Database.* Journal of Quantitative Spectroscopy and Radiative Transfer, being prepared.

7. Brosmer, M.A., Tien, C. L., *Radiative Energy Blockage in Large Pool Fires.* Combust Sci Technol, 1987. **51**(1-3): p. 21-37.

8. Klassen, M., and Gore, J. P., *Structure and Radiation Properties of Pool Fires*. 1994, National Institute of Standards and Technology.

9. Markstein, G.H., *Radiative Properties of Plastics Fires*. Seventeenth Symposium (International) on Combustion/The Combustion Institute, 1979: p. 1053-1062.

10. De Ris, J., *Fire Radiation-A Review*. Seventeenth Symposium (International) on Combustion/The Combustion Institute, 1979: p. 1003-1015.

11. Brosmer, M.A., and Tien, C. L., *Intrared Radiation Properties of Methane at Elevated Temperatures*. Joutnal of Quantitative Spectroscopy and Radiative Transfer, 1985. **33**: p. 521-532.

12. Brosmer, M.A., and Tien, C. L., *Thermal Radiation Properties of Acetylene*. ASME Journal of Heat Transfer, 1985. **107**: p. 943-948.

13. Brosmer, M.A., and Tien, C. L., *Thermal Radiation Properties of Propylene*. Combust Sci Technol, 1986. **48**: p. 163-175.

14. Park, S., H., Stretton, A. J., and Tien, C. L., *Infrared Radiation Properties of Methyl Methacrylate Vapor*. Combust Sci Technol, 1988. **62**: p. 257-271.

15. Fuss, S.P., Ezekoye, O.A., Hall, M.J., *The Absorptance of Infrared Radiation by Methane at Elevated Temperatures*. ASME Journal of Heat Transfer, 1996. **118**: p. 918-923.

16. Fuss, S.P., Hall, M. J., Ezekoye, O. A., *Band Integrated Infrared Absorptance of Low Molecular Weight Paraffin Hydrocarbons at High Temperatures*. Applied Optics, 1999. **38**: p. 2895-2904.

17. Fuss, S.P., Hamins, A., *Determination of Planck mean absorption coefficients for HBr, HCl, and HF*. J Heat Trans-T Asme, 2002. **124**(1): p. 26-29.

18. Rothman, L.S., Rinsland, C.P., Goldman, A., Massie, S.T., Edwards, D.P., Flaud, J.M., Perrin, A., Camy-Peyret, C., Dana, V., Mandin, J.Y., Schroeder, J., McCann, A., Gamache, R.R., Wattson, R.B., Yoshino, K., Chance, K.V., Jucks, K.W., Brown, L.R., Nemtchinov, V., and Varanasi, P., *The HITRAN Molecular Spectroscopic Database and HAWKS (HITRAN Atmospheric Workstation): 1996 Edition.* Journal of Quantitative Spectroscopy and Radiative Transfer, 1998. **60**: p. 665-710.

19. Quintiere, J.G., *Fire behavior in building compartments.* P Combust Inst, 2003. **29**: p. 181-193.

20. Fletcher, D.F., et al., *Numerical Simulations of Smoke Movement from a Pool Fire in a Ventilated Tunnel.* Fire Safety J, 1994. **23**(3): p. 305-325.

21. Apte, V.B., *Effect of scale and fuel type on the characteristics of pool fires for fire fighting training.* Fire Safety J, 1998. **31**(4): p. 283-298.

22. Chow, W.K., et al., *Natural smoke filling in atrium with liquid pool fires up to 1.6 MW.* Build Environ, 2001. **36**(1): p. 121-127.

23. Jeong, J.Y. and H.S. Ryon, *A study on smoke movement in room fires with various pool fire location.* Ksme Int J, 2002. **16**(11): p. 1485-1496.

24. Heskestad, G., *Extinction of gas and liquid pool fires with water sprays.* Fire Safety J, 2003. **38**(4): p. 301-317.

25. Kim, M.B., Y.J. Jang, and M.O. Yoon, *Extinction limit of a pool fire with a water mist.* Fire Safety J, 1997. **28**(4): p. 295-306.

26. Jones, A. and G.O. Thomas, *The Action of Water Sprays on Fires and Explosions - a Review of Experimental Work.* Process Saf Environ, 1993. **71**(B1): p. 41-49.

27. Prasad, K., C.P. Li, and K. Kailasanath, *Simulation of water mist suppression of small scale methanol liquid pool fires.* Fire Safety J, 1999. **33**(3): p. 185-212.

28. Prasad, K., G. Patnaik, and K. Kailasanath, *A numerical study of water-mist suppression of large scale compartment fires.* Fire Safety J, 2002. **37**(6): p. 569-589.

29. Wang, X.S., et al., *Experimental study on the effectiveness of the extinction of a pool fire with water mist.* J Fire Sci, 2002. **20**(4): p. 279-295.

30. Richard, J., et al., *On the flame structure at the base of a pool fire interacting with a water mist.* Exp Therm Fluid Sci, 2003. **27**(4): p. 439-448.

31. Richard, J., et al., *Chemical and physical effects of water vapor addition on diffusion flames.* Fire Safety J, 2003. **38**(6): p. 569-587.

32. Liu, J.H., et al., *Study of liquid pool fire suppression with water mists by cone calorimeter.* J Fire Sci, 2002. **20**(6): p. 465-477.

33. Liu, J.H., et al., *Progress in research and application of water mist fire suppression technology.* Chinese Sci Bull, 2003. **48**(8): p. 718-725.

34. Iwata, Y., et al., *Combustion characteristics of crude oils.* Fire Mater, 2001. **25**(1): p. 1-7.

35. Koseki, H., et al., *Tomakomai large scale crude oil fire experiments.* Fire Technol, 2000. **36**(1): p. 24-38.

36. Persson, B., A. Lonnermark, and H. Persson, *FOAMSPEX: Large scale foam application - Modelling of foam spread and extinguishment.* Fire Technol, 2003. **39**(4): p. 347-362.

37. Klassen, M., Sivathanu, Y. R., and Gore, J. P., *Simultaneous Emission Absorption Measurements in Toluene-Fueled Pool Flames: Mean and RMS Properties.* Combust Flame, 1992. **90**: p. 34-44.

38. Hamins, A., Fischer, S.J., and Kashiwagi, T., *Heat Feedback to the Surface in Pool Fires.* Combust Sci Technol, 1994. **97**: p. 37-62.

39. Gritzo, L.A., S.R. Tieszen, and D. Murray, *Flame structure of large, hydrocarbon-fueled pool fires.* J Heat Trans-T Asme, 1997. **119**(2): p. 209-209.

40. McGrattan, K.B., *Fire Dynamics Simulator (Version 4)-Technical Reference Guide.* 2004, National Institute of Standards and Technology: Gaithersburg, MD.

41. Hostikka, S., McGrattan, K. B., and Hamins A.,. *Numerical Modeling of Pool Fires Using LES an Finite Volume Method for Radiation.* in *Fire Safety Science - Proceedings of the Seventh International Symposium. International Association for Fire Safety Science (IAFSS).* 2003. Worcester, MA: Intl. Assoc. for Fire Safety Science.

42. Novozhilov, V. and H. Koseki, *CFD prediction of pool fire burning rates and flame feedback.* Combust Sci Technol, 2004. **176**(8): p. 1283-1307.

43. Prasad, K., et al., *Numerical modelling of methanol liquid pool fires.* Combust Theor Model, 1999. **3**(4): p. 743-768.

44. DeRis, J., *Fire Radiation-A Review.* Seventeenth Symposium (International) on Combustion/The Combustion Institute, 1979: p. 1003-1015.

45. McGrattan, K.B., Baum, H.R., Rehm, R.G., Hamins, A., Forney, G.P., Prasad, K., Floyd, J.E., and Hostikka, S.,, *Fire Dynamics Simulator (Version 3)- Technical*

Reference Guide. 2002, National Institute of Standards and Technology: Gaithersburg, MD.

46.   Grosshandler, W.L., *"RADCAL: A Narrow-Band Model for Radiation Calculations in a Combustion Environmnet,"*. 1993, National Institute of Standards and Technology.

47.   Modest, M.F., *Radiative Heat Transfer*. 2nd ed. 2003: Academic Press. 398-405.

48.   Modak, A.T., *The burning of large pool fres*. 1979, Factory Mutual Research.

49.   Brosmer, M.A. and C.L. Tien, *Radiative Energy Blockage in Large Pool Fires.* Combustion Science and Technology, 1987. **51**(1-3): p. 21-37.

50.   Gritzo, L.A., Nicolette. V.F., Tieszen, S. R., Moya, J. L., and Holen, J. *Heat transfer to the fuel surface in large pool fires*. in *Transport phenomena in combustion, Proceedings of the eighth International symposium on transport phenomena in combustion (ISTP-VIII)*. 1995. San Francisco, CA: Taylor and Francis.

51.   Hietaniemi, J., Hostikka, S., and Vaari J., *FDS simulatioin of fire spread - comparison of model results with experimental data.*, in *VTT Working papers 4, VTT Building and Transport*. 2004, VTT Building and Transport.

52.   Janssens, M.L., *Burning Characteristics of Heptane and Methanol Pool Fires.* Seventh International Conference on Fire and Materials, 2001: p. 517-526.

53.   Koseki, H., *Research on Oil Tank Fire.* Dissertation submitted for the degree of Doctor of Engineering, University of Tokyo, 1996.

54.   Banwell, C.N., and McCash E. M., *Fundamentals of molecular spectroscopy*. 4th ed. 1994: McGraw-Hill Book Company Europe.

55.   Gross, L.A., Griffiths, P.R., and Sun, J.N.-P., *Temperature Measurement by Infrared Spectroscopy*, in *Infrared Measurements for Gaseous Measurements*, J. Wormhoudt, Editor. 1985, Marcel Decker: New York. p. 81-132.

56.   Vidrine, W., *Thermal properties of transmissive optical materials - Optical Materials*. 2002, Vidrine Consulting.

57.   Tripp, C.P., and McFarlane, R. A., *Discussion of the Stray Light Rejection Efficiency FT-IR Spectrometers: The Effects of Sample Emission on FT-IR Spectra.* Applied Spectroscopy, 1994. **48**: p. 1138-1142.

58.   *NIST Chemistry Webbook http://webbook.nist.gov*, National Institute of Standards and Technology (NIST).

59.   Taine, J.a.S., N., *Gas IR radiative properties; From spectroscopic data to approximate models.* Advances in heat transfer, 1999. **33**: p. 295-414.

60.   Wakatsuki, K., Fuss, S. P., Hamins, A., and Nyden, M. R., *A Technique for Extrapolating Absorption Coefficient Measurements to High Temperatures.* P Combust Inst, 2004. **to appear**.

61.   Fleckl, T., Jager, H., and Obernberger, I., *Experimental verification of gas spectra calculated for high temperatures using the HITRAN and HITEMP database.* Journal of Physics. D: Applied Physics, 2002. **35**: p. 3138-3144.

62.   Chu, P.M., Guenther, F. M., Rhoderick, G., C., and Lafferty, W. J., *The NIST Quantitative Infrared Database.* Journal of Research of the National Institute of Standards and Technology, 1999. **104**: p. 59-81.

63.   Kee, R.J., Rupley, F. M., Miller, J. A., Coltrin, M. E., Grcar, J. F., Meeks, E., Moffat, H. K., Lutz, A. E., Dixon-Lewis, G., Smooke, M. D., Warnatz, J., Evans,

G. H., Larson, R. S., Mitchell, R. E., Petzold, L. R., Reynolds, W. C., Caracotsios, M. W., Stewart, E., Glarborg, P., Wang, C., Adigun, O., Houf, W. G., Chou, C. P., and Miller, S. F.,, *AURORA Application User Manual - CHEMKIN Collection*. 2003, Reaction Design, Inc., San Diego, CA.

64. *Chemical-Kinetic Mechanisms for Combustion Applications*. 2002, University of California, San Diego, Center for Energy Research.

65. *Kinetics Models and Data Used in Calculations*. 2002, Massachusetts Institute of Technology, Department of Chemical Engineering.

66. Rothman, L.S., Jacquemarta,D., Barbeb, A., Chris Bennerc, D., Birkd, M., Browne, L.R., Carleerf, M.R., Chackerian,C. Jr, Chancea, K., Couderth, L.H., Danai, V., Devic, V.M., Flaudh, J.M., Gamachej, R.R., Goldmank, A., Hartmannh, J.M., Jucksl, K.W., Makil, A.G., Mandini, J.Y., Massien, S.T., Orphalh, J., Perrinh, A., Rinslando, C.P., Smitho,M.A.H., Tennysonp, J., Tolchenovp, R.N., Tothe, R.A., Vander Auweraf, J., Varanasiq, P., Wagnerd, G., *The HITRAN 2004 Molecular Spectroscopic Database.* Journal of Quantitative Spectroscopy and Radiative Transfer, 2005. **to appear**.

67. Modest, M.F., Bharadwaj, S. P., *Medium resolution transmission measurements of CO2 at high temperature.* Journal of Quantitative Spectroscopy and Radiative Transfer, 2002. **73**: p. 329-338.

68. Dalzell, W.H., and Sarofim, A. F., *Optical constants of soot and their application to heat-flux calculations.* ASME Journal of Heat Transfer, 1969. **91**(1): p. 100-104.

69. Chang, H., Charalampopoulos, T., T., *Determination of the wavelength dependence of refractive indices of flame soot.* Proceedings of the Royal Society, Series A, 1990. **430**(1880): p. 577-591.

70. Felsk, J.D., Charalampopoulos, T.T., and Hura, H.S., *Determination of refractive indices of soot particles from the reflectivities of compressed soot particles.* Combustion Science and Technology, 1984. **37**: p. 263-284.

71. Siegel, R., and Howell, J. R.,, *Thermal Radiation Heat Transfer.* 3rd. ed. 1992, Washington, DC: Hemisphere Publishing.

72. Zhang, H.M., Modest, M. F., *Evaluation of the Planck-mean absorption coefficients from HITRAN and HITEMP databases.* J Quant Spectrosc Ra, 2002. **73**(6): p. 649-653.

73. Rohm and Haas Company, A.M., *Infrared Materials - Temperature Dependency Data.* May, 2000: Woburn, MA.

74. Lord, R.C., and Venkateswarlu, P., *The infrared spectra of propylene and propylene-d6.* Journal of Optical Society of America, 1953. **43**: p. 1079.

75. Silvia, B., Labarbe, P., and Perchard, J. P., *Spectres de vibrations et coordonees normales de quatre especes isotopiques de propene.* Spectrocim. Acta, 1973. **A29**: p. 263.

76. Hamins, A., *PhD Thesis.* University of California, San Diego, 1985.

77. Hamins, A., *Personal communication.* 2004.